



## รายงานวิจัยฉบับสมบูรณ์

โครงการ ตัวเร่งปฏิกิริยาที่เร่งด้วยแสงขนาดนาโนในรูปแบบเส้นใยที่มีความยืดหยุ่น

โดย รศ.ดร. วรงค์ ปวรจารย์ และคณะ

30 เมษายน 2562

## รายงานวิจัยฉบับสมบูรณ์

โครงการ ตัวเร่งปฏิกิริยาที่เร่งด้วยแสงขนาดนาโนในรูปแบบเส้นใยที่มีความยืดหยุ่น

### คณะผู้วิจัย

1. รศ.ดร. วรงค์ ปวรจารย์
2. น.ส. ฝากฝัน ดุริยศาสตร์
3. นาย กัญชัช ชัชกุล

### สังกัด

ภาควิชาวิศวกรรมเคมี จุฬาลงกรณ์มหาวิทยาลัย  
ภาควิชาวิศวกรรมเคมี จุฬาลงกรณ์มหาวิทยาลัย  
ภาควิชาวิศวกรรมเคมี จุฬาลงกรณ์มหาวิทยาลัย

สนับสนุนโดยสำนักงานกองทุนสนับสนุนการวิจัย

(ความเห็นในรายงานนี้เป็นของผู้วิจัย สกว. ไม่จำเป็นต้องเห็นด้วยเสมอไป)

## บทคัดย่อ

ปฏิกิริยาที่เร่งด้วยแสงในรูปแบบวิวิธพันธ์เป็นปฏิกิริยาที่มีความสำคัญในหลากหลายรูปแบบ เช่น การย่อยสลายสารปนเปื้อนตกค้าง การฆ่าเชื้อ หรือการสังเคราะห์สารต่างๆ โดยตัวเร่งปฏิกิริยาที่เป็นที่นิยมได้แก่ ไทเทเนียมออกไซด์ หรือสังกะสีออกไซด์ ทั้งนี้ ตัวเร่งปฏิกิริยาในรูปแบบอนุภาคนาโนมีข้อได้เปรียบหลายประการ เช่น มีความว่องไวสูงและมีพื้นที่ผิวมาก ทำให้มีการประยุกต์ใช้อนุภาคนาโนของไทเทเนียมออกไซด์และสังกะสีออกไซด์ มาเป็นตัวเร่งปฏิกิริยาด้วยแสงสำหรับการย่อยสลายสารมลพิษต่างๆ ในระดับห้องปฏิบัติการอย่างแพร่หลาย อย่างไรก็ตาม การนำอนุภาคนาโนไปประยุกต์ใช้จริงในอุตสาหกรรมนั้นยังมีข้อจำกัดในการดักจับอนุภาคออกจากของไหล ภายหลังจากที่การย่อยสลายได้เสร็จสิ้นลง ด้วยขนาดของอนุภาคที่เล็กจนไม่สามารถดักจับได้อย่างมีประสิทธิภาพ ทำให้มีการหลุดลอดของตัวเร่งปฏิกิริยา ติดไปกับกระแสของไหลออกสู่สิ่งแวดล้อมได้ ส่งผลทำให้เกิดผลเสียทั้งในด้านการสูญเสียตัวเร่งปฏิกิริยาและในด้านความเป็นพิษของอนุภาคนาโนหากมีการปนเปื้อนในสิ่งแวดล้อม การเปลี่ยนรูปสัณฐานของตัวเร่งปฏิกิริยาให้เป็นเส้นใยนาโนเป็นวิธีแก้ปัญหาดังกล่าวข้างต้นวิธีหนึ่ง แต่ด้วยความเปราะบางของไทเทเนียมออกไซด์และสังกะสีออกไซด์เอง ทำให้เกิดการแตกหักเส้นใยนาโนกลับมาเป็นอนุภาคนาโนและเกิดปัญหาเช่นเดิม โครงการวิจัยนี้นำเสนอการปรับปรุงเส้นใยนาโนของตัวเร่งปฏิกิริยาไทเทเนียมออกไซด์ และสังกะสีออกไซด์โดยการสังเคราะห์ให้เป็นเส้นใยนาโนที่มีแกนของพอลิเมอร์ เพื่อให้เกิดความยืดหยุ่น ไม่แตกหักได้ง่าย ด้วยการปั่นเส้นใยด้วยไฟฟ้าสถิตย์ชนิดมีแกนร่วมโดยมีพอลิเอคริโรไนไตรด์เป็นแกน และใช้สารผสมระหว่างเจลจากการสังเคราะห์ด้วยวิธีโซลเจลของไทเทเนียมออกไซด์หรือสังกะสีออกไซด์กับพอลิไวนิลไพโรลิโดนเป็นส่วนเปลือกนอกของเส้นใย พบว่าสามารถผลิตเส้นใยที่มีความยืดหยุ่นตามต้องการได้โดยการควบคุมตัวแปรในการสังเคราะห์ อาทิเช่น ความหนืดของสารละลาย ความเข้มข้นของพอลิเมอร์ที่ใช้ ค่าศักย์ไฟฟ้าที่ใช้ในการปั่นเส้นใย และอุณหภูมิในการเผาให้อยู่ในค่าที่เหมาะสม อย่างไรก็ตาม การจมน้ำของอนุภาคลงไปในแกนพอลิเอคริโรไนไตรด์ส่งผลให้ความว่องไวของตัวเร่งปฏิกิริยาที่เปลือกด้านนอกของเส้นใยลดลงเมื่อเทียบกับเมื่อสังเคราะห์เป็นอนุภาคนาโน ทั้งนี้ ในระหว่างการทดสอบความว่องไวในการเร่งปฏิกิริยาในโครงการนี้ ได้ค้นพบว่ารูปแบบการจัดเรียงตัวของอะตอมของตัวเร่งปฏิกิริยาบนพื้นผิว ส่งผลที่สำคัญต่อรูปแบบการดูดซับของสารที่จะย่อยสลายบนพื้นผิวของตัวเร่งปฏิกิริยา ซึ่งให้ผลกระทบต่อการเกิดปฏิกิริยาทั้งในแง่อัตราการเกิดปฏิกิริยาและเส้นทางการเกิดปฏิกิริยาซึ่งมีความสำคัญอย่างยิ่ง โดยเฉพาะในการย่อยสลายสารพิษเพื่อการบำบัด

**คำหลัก:** เส้นใยนาโนที่ยืดหยุ่นได้; ตัวเร่งปฏิกิริยาที่เร่งด้วยแสง; ปฏิกิริยาที่เร่งด้วยแสง

## **Abstract**

Heterogeneous photocatalytic reaction is an important reaction for various applications, such as degradation of contaminated compounds, disinfection, or even in the synthesis of various compounds. The common photocatalysts are titanium oxide and zinc oxide. The photocatalysts in a form of nanoparticle has several advantages, such as high activity and high surface area, which makes them favorable in the degradation of toxic contaminants in lab-scale. However, the application of nanoparticles in industrial scale is limited by the recovery of the particles from fluid after the treatment is completed because effective capturing of the nanoparticles is very difficult. Incomplete recovery of the particles from the fluid causes the loss of the catalyst and the problem in contamination of nanoparticles in the environment. One way to solve the problem is changing the morphology of the catalyst from nanoparticles to nanofibers. However, due to brittleness of titanium oxide and zinc oxide, the nanofibers usually are crumbling back to nanoparticles after usage. This research proposes the fabrication of the nanofibers of titanium oxide and zinc oxide into fibers with flexible polymer core via coaxial electrospinning, using polyacrylonitrile as core and a mixture of titanium oxide or zinc oxide gel derived from sol-gel technique and polyvinylpyrrolidone as sheath. It was found that the flexible nanofibers could be fabricated by controlling various parameters such as viscosity of solutions, concentrations of polymers, applied potential for electrospinning, and calcination temperature. However, the coverage of the photocatalyst crystals into polyacrylonitrile significantly decreases activity of the photocatalyst on the sheath of the fibers, compared to that of the same catalyst in nanoparticle form. Nevertheless, during the photocatalyst testing in the research, it was discovered that atomic configuration of the surface of the catalyst greatly affects adsorption configuration of the compound being degraded. Consequently, it affects both rate of the degradation and the degradation pathway, which is extremely important for the degradation of toxic contaminants.

**Keywords:** Flexible nanofibers; Photocatalyst; Photocatalytic reaction

## หน้าสรุปโครงการ (Executive summary)

1. ชื่อโครงการ (ภาษาไทย)      ตัวเร่งปฏิกิริยาที่เร่งด้วยแสงขนาดนาโนในรูปแบบเส้นใยที่มีความยืดหยุ่น  
(ภาษาอังกฤษ)      Flexible nanofibers of photocatalyst

### 2. ปัญหาที่ทำการวิจัย และความสำคัญของปัญหา

ปฏิกิริยาที่เร่งด้วยแสง (photocatalysis) เป็นปฏิกิริยาที่มีความสำคัญในหลายหลายสาขา เช่น การย่อยสลายสารปนเปื้อนตกค้าง การฆ่าเชื้อ การผลิตเชื้อเพลิงทางเลือก หรือการสังเคราะห์สารต่างๆ โดยในกระบวนการของปฏิกิริยาที่เร่งด้วยแสงในรูปแบบวิวิธพันธ์ (heterogeneous photocatalysis) นั้น ตัวเร่งปฏิกิริยาที่เป็นที่นิยมได้แก่ ไทเทเนียมออกไซด์ หรือสังกะสีออกไซด์ ซึ่งมีความสามารถปล่อยอนุมูล (radical) ที่มีความว่องไวต่อการทำปฏิกิริยาเมื่อได้รับแสง ซึ่งสำหรับการย่อยสลายสารปนเปื้อนตกค้างแล้ว อนุมูลเหล่านี้สามารถเข้าทำปฏิกิริยากับสารมลพิษต่างๆ เกิดเป็นก๊าซคาร์บอนไดออกไซด์ และสารตกค้างที่ไม่เป็นอันตรายเช่นไนเตรต ทั้งนี้ ความสำเร็จของการเกิดปฏิกิริยาขึ้นอยู่กับปัจจัยหลายประการ ทั้งในแง่ของสถานะของการเกิดปฏิกิริยาเช่น ค่าความเป็นกรดเบสของสารละลาย อุณหภูมิ หรือระดับความเข้มข้นของสารปนเปื้อนในสารละลาย และในแง่ของสมบัติของตัวเร่งปฏิกิริยาเช่น ขนาดพื้นที่ผิว ความสมบูรณ์ของผลึก หรือขนาด bandgap ของตัวเร่งปฏิกิริยา โดยในส่วนสมบัติของตัวเร่งปฏิกิริยานั้น พบว่าการใช้ตัวเร่งปฏิกิริยาในรูปของอนุภาคนาโนมีข้อได้เปรียบหลายประการ อาทิเช่น มีพื้นที่ผิวที่มาก ขนาดอนุภาคเล็กทำให้ไม่เกิดการบังแสง สามารถสังเคราะห์ให้ผลึกมีความสมบูรณ์สูงหรือให้ผลึกมีจุดบกพร่อง (defect) ภายในผลึกได้ตามต้องการ และสามารถสังเคราะห์ผลึกให้มีระดับของ bandgap ตามต้องการได้โดยง่าย ทำให้มีการประยุกต์ใช้อนุภาคนาโนของสารต่างๆ เช่นไทเทเนียมออกไซด์และสังกะสีออกไซด์ มาเป็นตัวเร่งปฏิกิริยาด้วยแสง (photocatalyst) สำหรับการย่อยสลายสารมลพิษต่างๆ ในระดับห้องปฏิบัติการอย่างแพร่หลาย อย่างไรก็ตาม การนำอนุภาคนาโนไปประยุกต์ใช้จริงในอุตสาหกรรมนั้นยังมีข้อจำกัดในการดักจับอนุภาคออกจากของไหล ภายหลังจากที่การย่อยสลายได้เสร็จสิ้นลง ด้วยขนาดของอนุภาคที่เล็กจนไม่สามารถดักจับได้อย่างมีประสิทธิภาพ ทำให้มีการหลุดลอดของตัวเร่งปฏิกิริยาติดไปกับกระแสของไหลออกสู่สิ่งแวดล้อมได้ ส่งผลทำให้เกิดผลเสียทั้งในด้านการสูญเสียตัวเร่งปฏิกิริยาและในด้านความเป็นพิษของอนุภาคนาโนหากมีการปนเปื้อนในสิ่งแวดล้อม

สำหรับตัวเร่งปฏิกิริยชนิดอื่นแล้ว ปัญหาการหลุดลอดจากการดักจับเช่นนี้สามารถแก้ไขได้ด้วยการทำให้ตัวเร่งปฏิกิริยาอยู่ในรูปเม็ด (pellet) ที่มีขนาดใหญ่ขึ้น แต่สำหรับตัวเร่งปฏิกิริยาที่เร่งด้วยแสงแล้ว ไม่สามารถแก้ปัญหาด้วยวิธีเช่นนี้ได้ เนื่องจากการทำเป็นเม็ดจะทำให้แสงไม่สามารถเข้าถึงส่วนด้านในของเม็ดและทำให้ตัวเร่งปฏิกิริยาในส่วนนั้นไม่ว่องไว ในขณะที่การเคลือบอนุภาคนาโนให้อยู่ในรูปฟิล์มนั้นส่งผลให้เกิดการลดลงของพื้นที่ผิวจำนวนมาก

ปัญหาเช่นนี้สามารถแก้ไขได้โดยการเปลี่ยนตัวเร่งปฏิกิริยาให้อยู่ในรูปแบบเส้นใยนาโน (nanofiber) ซึ่งยังคงมีขนาดเกรน (grain) อยู่ในระดับนาโนเมตร ทำให้ยังคงมีความว่องไวและสมบัติที่ดี

ของอนุภาคนาโน หากแต่สามารถดักจับออกจากของไหลได้ง่ายเนื่องจากเส้นใยมีความยาวอยู่ในระดับหลายร้อยไมโครเมตรถึงระดับมิลลิเมตร โดยการสังเคราะห์เส้นใยนาโนของตัวเร่งปฏิกิริยาเช่นไทเทเนียมออกไซด์ หรือสังกะสีออกไซด์ นั้นสามารถทำได้โดยง่ายด้วยวิธีการปั่นเส้นใยด้วยไฟฟ้าสถิตย์ (electrospinning) ซึ่งผลการทดลองได้แสดงให้เห็นว่าเส้นใยนาโนเหล่านี้มีความว่องไวในการเร่งปฏิกิริยาเทียบเท่ากับตัวเร่งปฏิกิริยาที่อยู่ในรูปสัณฐานของอนุภาคนาโน อย่างไรก็ตาม พบว่าเส้นใยเหล่านี้มีความเปราะและจะแตกหักกลายเป็นอนุภาคได้โดยง่าย เนื่องจากสมบัติความเปราะของไทเทเนียมออกไซด์ หรือสังกะสีออกไซด์เอง

โครงการวิจัยนี้จึงมีข้อเสนอในการปรับปรุงเส้นใยนาโนของตัวเร่งปฏิกิริยาไทเทเนียมออกไซด์ และสังกะสีออกไซด์โดยการสังเคราะห์ให้เป็นเส้นใยนาโนที่มีแกนของพอลิเมอร์เพื่อให้เกิดความยืดหยุ่นไม่แตกหักได้ง่าย แต่ยังคงไว้ด้วยความว่องไวจากเกรนที่มีขนาดระดับนาโน โดยเสนอการสังเคราะห์เส้นใยนาโนแบบมีแกนร่วม (co-axial nanofibers) ด้วยวิธีการปั่นด้วยไฟฟ้าสถิตย์

### 3. สรุปย่อผลการดำเนินงานของโครงการ

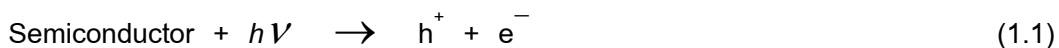
โครงการนี้เป็นการสังเคราะห์ตัวเร่งปฏิกิริยาไทเทเนียมออกไซด์และสังกะสีออกไซด์ให้อยู่ในรูปของเส้นใยนาโนที่มีความยืดหยุ่นโดยการสังเคราะห์ด้วยวิธีการปั่นเส้นใยด้วยไฟฟ้าสถิตย์แบบมีแกนร่วม โดยพบว่าวัสดุที่เหมาะสมกับการเป็นแกนที่สามารถให้ความยืดหยุ่นและในขณะเดียวกันสามารถทนต่อสภาวะการเผาเปลี่ยนสารตั้งต้นให้เป็นไทเทเนียมออกไซด์หรือสังกะสีออกไซด์ได้นั้นคือพอลิเอครีโรไนไตรด์ และสามารถสังเคราะห์เส้นใยนาโนที่มีแกนพอลิเอครีโรไนไตรด์และมีผลึกของไทเทเนียมออกไซด์หรือสังกะสีออกไซด์อยู่ภายนอกได้โดยการเลือกค่าตัวแปรในการสังเคราะห์อันได้แก่ ความหนืดของสารละลาย ความเข้มข้นของพอลิเมอร์ที่ใช้ ค่าศักย์ไฟฟ้าที่ใช้ในการปั่นเส้นใย และอุณหภูมิในการเผาให้อยู่ในค่าที่เหมาะสม โดยความหนืดของสารละลายและความเข้มข้นของพอลิเมอร์ที่ใช้ส่งผลกระทบต่อโครงสร้างของเส้นใยที่ปั่นออกมาได้ว่าจะเป็นแบบแกนร่วมหรือไม่ ค่าศักย์ไฟฟ้าที่ใช้ในการปั่นเส้นใยส่งผลกระทบต่อความสามารถในการผลิตเส้นใยและรูปร่างของเส้นใยในภาพรวม ส่วนอุณหภูมิในการเผานั้นส่งผลต่อการกำจัดพอลิเมอร์ในชั้นเปลือกและความเป็นผลึกของตัวเร่งปฏิกิริยา ซึ่งหากอุณหภูมิในการเผามีค่าน้อยเกินไปจะได้ตัวเร่งปฏิกิริยาที่มีความเป็นผลึกต่ำและมีพอลิเมอร์ห่อหุ้มอยู่ แต่หากอุณหภูมิในการเผาสูงเกินไปจะทำให้สูญเสียแกนพอลิเอครีโรไนไตรด์ไป ดังนั้นการสังเคราะห์เส้นใยนาโนที่มีลักษณะตามต้องการจึงต้องจำกัดตัวแปรเหล่านี้ให้มีค่าพอเหมาะ อย่างไรก็ตาม ไม่ว่าจะเปลี่ยนแปลงค่าตัวแปรในการผลิตอย่างไร การจมผิของอนุภาคลงไปในแกนพอลิเอครีโรไนไตรด์ส่งผลให้ความว่องไวของตัวเร่งปฏิกิริยาที่เปลือกด้านนอกของเส้นใยลดลงอย่างมีนัยสำคัญเมื่อเทียบกับตัวเร่งปฏิกิริยาชนิดเดียวกันที่สังเคราะห์เป็นอนุภาคนาโน ทั้งนี้ ในระหว่างการทดสอบความว่องไวในการเร่งปฏิกิริยาในโครงการนี้ ได้ค้นพบว่ารูปแบบการจัดเรียงตัวของอะตอมของตัวเร่งปฏิกิริยาบนพื้นผิว ส่งผลที่สำคัญต่อรูปแบบการดูดซับของสารที่จะย่อยสลายบนพื้นผิวของตัวเร่งปฏิกิริยา ซึ่งให้ผลกระทบต่อการศึกษาทั้งในแง่อัตราการเกิดปฏิกิริยาและเส้นทางการเกิดปฏิกิริยาซึ่งมีความสำคัญอย่างยิ่ง โดยเฉพาะในการย่อยสลายสารพิษเพื่อการบำบัด

## 1. Introduction

### 1.1 Photocatalytic reaction

Water pollution from organic compounds, either from industrial or agricultural activities, is one of the important problems in our country. Examples of the contaminants include dyes, fertilizers, and pesticides. These compounds lead to contamination of water resource, which may cause severe problem if the contaminants are toxic. The removal of the toxicant is needed. There are many kinds of water treatment techniques, each of which is suitable for particular application. In this work, heterogeneous photocatalytic degradation, which is one of the advanced oxidation processes (AOPs), is considered because it is effective in removal of organic contaminants, especially when the concentration is so low that other treatment techniques fail. It is particularly important when the contaminant is highly toxic and presents in water in very low concentration, but still enough to cause harmful effects to human and environment. An example of such substance is diuron [3-(3,4-dichlorophenyl)-1,1-dimethyl urea], which is an herbicide widely used in Thailand. Although diuron has low solubility in water, it is a bio-recalcitrant compound with great chemical stability. Hence, it can slowly dissolve in water and can penetrate through the soil, causing contamination of both underground and surface water.

The most commonly used photocatalysts are titanium (IV) oxide ( $\text{TiO}_2$ ) and zinc oxide ( $\text{ZnO}$ ) due to their high photocatalytic activity, low cost, good chemical stability and non-toxicity. Both compounds share similar band gap of 3.1-3.4 eV [1] and are expected to result in similar photocatalytic mechanism [2, 3]. Photocatalytic reactions take place when the semiconductor particle absorbs photon with energy equal to or more than the band gap, the electron is excited from the valence band (VB) to the conduction band (CB), producing electron-hole ( $e^-/h^+$ ). The generations of electron-hole pairs are represented in Eq. (1.1). The photo-generated holes and electrons give rise to oxidation and reduction processes, respectively. In an aqueous solution, water molecules adsorb onto surface of the catalyst. They are oxidized giving rise to  $\text{OH}^\bullet$  radicals. As the process is usually carried out in aerobic conditions, the species to be reduced is oxygen, generating the superoxide radical as following Eq. (1.2) to (1.4). Organic pollutants adsorb onto the surface of the catalyst are subsequently oxidized by  $\text{OH}^\bullet$  radicals.



Support of the  $\text{OH}\cdot$  radical as the main reactive oxidant derives from the observation that intermediates detected during the photocatalytic degradation of halogenated aromatic compounds are typically hydroxyl structures, as those found when similar aromatics react with a known source of  $\text{OH}\cdot$  radicals. The hydroxyl radical is an extremely strong, non-selective oxidant that brings about the degradation of organic compounds [4, 5]. Although the photogenerated holes could directly oxidize the contaminant, in aqueous solution, the holes normally react with the abundant water molecules to form hydroxyl radicals [6]. Hence, hydroxyl radicals are generally accepted to be the primary cause of mineralization of organic matters that are adsorbing on the surface of the photocatalyst.

## 1.2 Photocatalysts

### 1.2.1 Physical and chemical properties of $\text{TiO}_2$

Titanium (IV) oxide or titania occurs in nature as well-known minerals rutile (tetragonal), anatase (tetragonal) and brookite (orthorhombic), and additionally as two high pressure forms, a monoclinic baddeleyite-like form and an orthorhombic  $\alpha$ - $\text{PbO}_2$ -like form. The most common form is rutile, which is also the most stable form. Anatase and brookite can both convert to rutile upon heating. Anatase is a metastable phase, which tends to be more stable at low temperature. For brookite, it is formed under hydrothermal conditions and usually found only in mineral. Although titania is known to have three natural polymorphs, only anatase is generally accepted to have significant photocatalytic activity.

The transformation from anatase to rutile is accompanied by evolution of ca. 12.6 kJ/mol (3.01 kcal/mol). The rate of phase transformation is greatly affected by temperature and by presence of other substances which may either catalyze or inhibit the transformation. The lowest temperature at which the conversion from anatase to rutile takes place at a measurable rate is approximately 500-550°C [7]. The change is not reversible and it has been shown that  $\Delta G$  for the transformation from anatase to rutile is always negative.



### 1.2.2 Physical and chemical properties of ZnO

Zinc oxide is an *n*-type semiconductor with a band gap of around 3.20 eV and the free excitation energy of 60 meV, which makes it very high potential for room temperature light emission. This also gives zinc oxide strong resistance to high temperature electronic degradation during operation. Therefore, it is attractive for many optoelectronic applications in the range of blue and violet light as well as UV devices for wide range of technological applications. Zinc oxide also exhibits dual semiconducting and piezoelectric properties.

Zinc oxide is a II-VI compound semiconductor of which the ionicity resides at the borderline between covalent and ionic semiconductor. The crystal structures shared by zinc oxide are wurtzite (hexagonal), zinc blende (cubic), and rocksalt (cubic). At ambient conditions, the thermodynamically stable phase is wurtzite. The zinc-blende structure can be formed only by the growth of ZnO on cubic substrate. The rocksalt structure may be obtained at relatively high pressure.

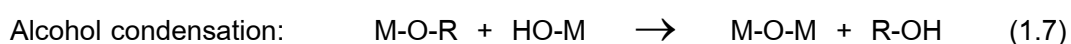
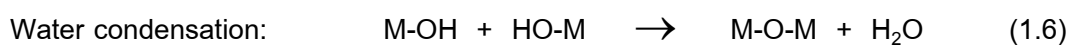
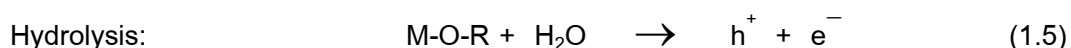
It has been reported that the activity of nanosized zinc oxide is higher than nanosized titania [8]. The smaller particle, the higher the photocatalytic activity and the coupling of titania with zinc oxide seems useful in order to achieve more efficient electron-hole pair separation under illumination and, consequently, a higher reaction rate. The increase in the lifetime of the photoproducts, due to hole and electron transfer between the two coupled semiconductors, is produced in many cases as key factor for the improvement of the photoactivity [9].

### 1.3 Sol-gel process

There are several methods that can be used to synthesize semiconductor photocatalysts. In general, methods which have been reported for titania and zinc oxide are: sol-gel method [10, 11], hydrothermal or solvothermal method [12, 13], and precipitation method [14, 15]. One of the popular techniques is sol-gel method because of its low cost, reliability, and simplicity. Sol-gel process is a route generally applied to prepare nanomaterial with notable advantages of high purity and good microstructure. More importantly, this technique can be incorporated to the electrospinning, which is a technique to produce nanofibers. So this method was selected to prepare photocatalyst in this work.

Sol-gel reaction is a common technique used in the synthesis of metal oxide compounds. Sol-gel process involves the formation of sol followed by that of gel. The process starts from a chemical solution or sol that acts as precursor for an integrated network or gel of either discrete particles or network polymers. Sol; a suspension solid in liquid with particle size ranging from 1 nm to 1  $\mu\text{m}$ , can be obtained by hydrolysis and partial condensation of a precursor such as inorganic salt or metal alkoxide. Further condensation of sol particles into a three-dimensional network produces gel, which is a diphasic material with a solid encapsulating liquid or solvent. Alternatively, destabilizing the solution of preformed sols can also produce gel. These materials are referred to be aquasol or aquagel if water is used as solvent, and alcosol or alcogel if alcohol is used.

The precursor in sol-gel preparation can either be metal salt/alkoxide dissolved in appropriate solvent or stable colloidal suspension of preformed sols. Metal alkoxides have been most extensively used because they are commercially available in high purity and their solution chemical has been well documented. At its simplest level, sol-gel chemistry with metal alkoxide can be described in term of two classes of reaction:



where M and R are metal atom and alkyl group, respectively.

Because hydrolysis and condensation are both nucleophilic displacement reactions, the reactivity of metal alkoxides depends on the positive charge of partially charged metal atom and its coordination number. For example, tetraethyl orthosilicate (TEOS) is the least reactive comparing with common alkoxides because of the small positive partial charge on silicon. Thus, the longer and bulkier the alkoxide group attaching to a particular metal atom, the less reactive in hydrolysis and condensation of that precursor is. Therefore, changing type of precursor and/or its concentration are effective means toward controlling the reaction rates.

For sol-gel parameters, an important parameter affecting the reaction rate is temperature, which can be adjusted to increase or decrease rate of reaction. Type of solvent can affect the condensation reaction directly. It is also possible to prepare gel without solvent as long as another mean, such as ultrasound irradiation, is used to homogenize an otherwise immiscible alkoxide/water mixture. Another parameter called gelation time, which is defined as the time that the solution undergoes rapid rising in viscosity, is corresponding to the transition

from viscous fluid to elastic gel. At the gel point, the solid phase forms a continuous structure that reflects the formation and branching of particles under specific growth condition. This particular phase is important because it is the genesis of structural evolution that takes place in all subsequent processing steps.

#### *1.4 Electrospinning*

Electrospinning has been recognized as a simple technique, which involves polymer science, electrical engineering, mechanical engineering, material engineering and rheology. Electrospinning technique produces fibers with diameter in the range of nanometer to micrometer. The conventional process consists of applying electrical potential between a grounded collector and a droplet of polymer solutions or melt held at the end of capillary tube because of its surface tension. As the voltage is increased, charge is induced on the surface of fluid. When the applied electric field overcomes the surface tension of the droplet, the droplet is distorted forming a conical shape, commonly referred to as the Taylor cone. Then, a charged jet of the solution or melt is ejected from the apex of a conical shape, then the jet grows longer and thinner due to bending instability or splitting [16, 17]. While the jet travels toward to a collector, the solvent evaporates or the polymer solidifies and randomly deposited as a non-woven on the collector [18].

When gel derived from the sol-gel technique is mixed with polymer and subjected to electrospinning, composite nanofibers made from polymer and amorphous gel could be formed. Upon the calcination, the polymer could be removed via combustion, while the amorphous gel is transformed into crystalline inorganic materials. The fibers remain as continuous structures with their average diameter reduced due to the loss of the polymer. Nanofibers of titania and zinc oxide have been fabricated using this technique [19, 20]. Nevertheless, nanofibers of both titania and zinc oxide prepared by the aforementioned technique are brittle and can be crumble into powder after repeated uses.

In this work, the crumbling problem of titania and zinc oxide nanofibers is prevented by introducing a flexible polymer core within the fiber. This can be achieved by using co-axial electrospinning. The principle of co-axial electrospinning is similar to that of the conventional electrospinning. In the co-axial electrospinning process, two different materials are used in producing core part and sheath part of the fiber. The core material and sheath material are delivered independently through a co-axial capillary forming compound droplet. The compound droplet is charged after the high voltage is supplied. Charges are induced on the surface of

sheath fluid predominantly [21]. Above the critical value of electrical potential supplied, fluid droplet will be distorted via repulsive force of charges, resulted in small jet forming from the compound cone of materials. Rapid stretching of the sheath material can create strong viscous stress inside sheath fluid and will be transferred to the core material [22]. The core part will be stretched and elongated by the shear stress at the interface between core part and sheath part, which results in the formation of nanofiber in core-sheath configuration [23]. Hence, it is designed in this work to supplied polymer solution as core fluid, while the mixture of polymer and gel to either titania or zinc oxide is supplied as sheath fluid. Polyacrylonitrile is considered to be a core material of the fiber because of its high decomposition temperature so that it can withstand calcination, which is required to transform amorphous gel to crystalline titania or zinc oxide.

## **2. Experimental**

### *2.1 Solution preparations*

#### *2.1.1 Preparation of core solution*

The core solution of polyacrylonitrile (PAN) was prepared by dissolving polyacrylonitrile (average molecular weight of 86,2000) in *n,n'*-dimethylformamide (DMF) at 60°C and constantly stirred for 1 h. The concentration of PAN in the solution was varied to get suitable value for the fabrication of core-sheath nanofibers via electrospinning.

#### *2.1.2 Preparation of TiO<sub>2</sub>/PVP sheath solution*

For the fabrication of titania core-sheath nanofibers, the sheath solution was prepared by combining polyvinylpyrrolidone (PVP), acetic acid, DMF and titania precursor i.e., titanium (IV) isopropoxide (TTIP). First, PVP solution was prepared by dissolving 2.5 g of PVP (average molecular weight of 1,300,000) in 20 ml of DMF. In the meantime, titania-precursor solution was prepared by stirring 3 ml of TTIP together with 6 ml DMF and 6 ml acetic acid for 15 min. The precursor solution was slowly added into the PVP solution and stirred for 70 min to obtain the sheath solution.

### 2.1.3 Preparation of ZnO/PVP sheath solution

For the fabrication of zinc oxide core-sheath nanofibers, the ZnO-precursor solution was prepared by mixing 3.29 g of zinc acetate and various amount of PVP in 20 ml of DMF. Then, a mixture of 0.26 ml of distilled water, 0.18 ml of hydrochloric acid, and 1.58 ml of diethanolamine (DEA) in 5 ml of DMF was added to the precursor solution under continuous stirring for 2 h to achieve a transparent ZnO/PVP sheath solution.

### 2.2 Co-axial electrospinning

The co-axial nozzle was fabricated in-house using a stainless needle (gauge number 22, i.e., outer diameter of 0.7 mm) inserted into a copper nozzle (inside diameter of 1.5 mm). Each electrospinning solution was instantly filled into each plastic syringe, which was furnished into the co-axial nozzle. The syringe which contains core solution was connected to the core of the nozzle (i.e., the stainless steel needle) and another syringe connected to the shell of the nozzle (i.e., the copper nozzle) contained the sheath solution. The emitting electrode from the power supply (R6243, DC voltage current source/monitor, Advantest, Japan) was attached to the nozzle. The grounding electrode from the same power supply was attached to a piece of aluminum foil, which was used as the collector plate and was placed in front of the tip of the nozzle. The distance between the tip of the nozzle and the collector would be varied in the study. Upon the application of high voltage across the nozzle and the collector in the range of 20-25 kV, which will also be investigated, a fluid jet will be ejected from the nozzle. As the jet accelerated towards the collector, the solvent evaporated, leaving only ultrathin fibers on the collector. In addition, the fibers products were left for completely evaporation of solvent for 24 h.

### 2.3 Calcination of the core-sheath fibers

The calcination of electrospun core-sheath nanofibers was performed in a box furnace. The temperature of the furnace was raised from room temperature to temperature in the range of 400 to 550°C with heating rate at 5°C/min, then hold at this temperature for 2 h.

### 2.4 Characterization of the products

Morphology of the obtained products was determined by using scanning electron microscopy (JEOL JSM-6400 at the Scientific and Technological Research Equipment Center (STREC), Chulalongkorn University). Size of the fibers were measured using image processing

program from SEM micrographs. The core-sheath structure was investigated using transmission electron microscopy at National Nanotechnology Center (NANOTEC).

The decomposition temperature and thermal behavior of the obtained products were studied by using thermogravimetric analysis on a Mettler-Toledo TGA/DSC1 STARe System at Center of Excellence in Particle and Technology Engineering laboratory, Chulalongkorn University. The samples were heated under the oxygen flow of 40 ml/h and the ramp rate of 10 °C/min.

A Fourier transform infrared spectrometer (Nicolet 6700) at Center of Excellence in Particle and Technology Engineering laboratory, Chulalongkorn University was used to investigate the functional group in the products. The samples of the products were mixed with KBr in a ratio of sample to KBr 1:100 and formed into a pellet before measurement.

The crystalline phase of the synthesized catalyst was analyzed by X-ray diffraction (XRD) using a Bruker AXS D8 Advance diffractometer under  $\text{CuK}\alpha$  radiation. The crystallite size of the products was estimated from the full-width at half-maximum (FWHM) of the peak with strongest intensity using Debye-Scherrer equation.

The tensile strength of the fiber products was measured by Lloyd Universal Testing Machine, using at The Analytical and Testing Service Center, The Petroleum and Petrochemical Collage, Chulalongkorn University. The sheets of fiber products were cut into a dimension of  $1 \times 3 \text{ cm}^2$  in width and length, respectively. The thickness of the films is control by the electrospinning time of 5 h. The specimens were pulled with the rate of 10 N/min while measuring.

## *2.5 Photocatalytic degradation*

The photocatalytic activity of the synthesise products was preliminarily evaluated by the degradation of methylene blue (MB) solution under UV-A irradiation (Phillips TLD 15W/05). The concentration of MB was fixed at 10 ppm. The content of the catalyst used was equivalent to 1 mg of the catalyst per 10 ml of the solution. The mixture was constantly stirred in the dark for 30 min to reach the adsorption equilibrium of MB on the surface of the catalyst, prior to the reaction. After that, the solution was irradiated while continuously stirred. The concentration of MB was periodically measured by UV-Vis spectrophotometer (Shimadzu, UV-1700) at the maximum absorption wavelength of MB (i.e., 664 nm).

### 3. Results and discussion

#### 3.1 Formation of PAN/PVP core-sheath fibers

According to the research objective, it is necessary to confirm that the core-sheath structure could be obtained by the co-axial electrospinning process. Nevertheless, mixing could occur in co-axial electrospinning process of miscible core/sheath solutions. Therefore, PAN/PVP co-axial fibers were fabricated to test the ability to form the core-sheath structure from PAN core solution and PVP sheath solution, both of which are miscible. Moreover, effects of solution viscosities on the fiber morphology were also studied as there is a range of suitable viscosity of the solution for producing fibers from the conventional electrospinning process. In the co-axial electrospinning, it is still not clear that the core solution and the sheath solution are necessary to be electrospun separately. In this research, the concentration of each solution that could produce the electrospinnable solutions was considered. Therefore, the starting concentration of PAN was in the range of around 8 wt%, which could produce the PAN smooth fibers [24]. In the same way for PVP solution, the concentration that can produce uniform PVP fibers around 10 wt%, while the measured viscosity is around 0.1 Pa.s. SEM images in Figure 3.1 show that the smooth and uniform fibers could be fabricated only when the concentration of both solutions are in proper range. Beads are formed on the fibers when the PAN concentration is 6 wt% On the other hand, when the concentration of PAN is increased to 10 wt%, the fibers formed are less uniform in size. The proper concentration of PAN was found to be 8 wt%

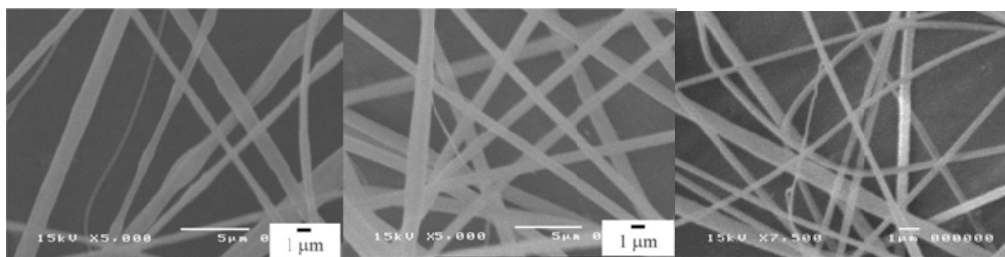


Figure 3.1 SEM images of products of PAN solution and PVP solution whereas the concentrations of PVP and PAN solutions are 10/6 (a), 10/8 (b), and 10/10 (c) wt%/wt%, respectively.

The co-axial electrospun fibers were observed by TEM micrographs as shown in Figure 3.2, which confirm that the obtained products are indeed core-sheath nanofibers. The boundary between core material and sheath material can be seen from these TEM micrographs.

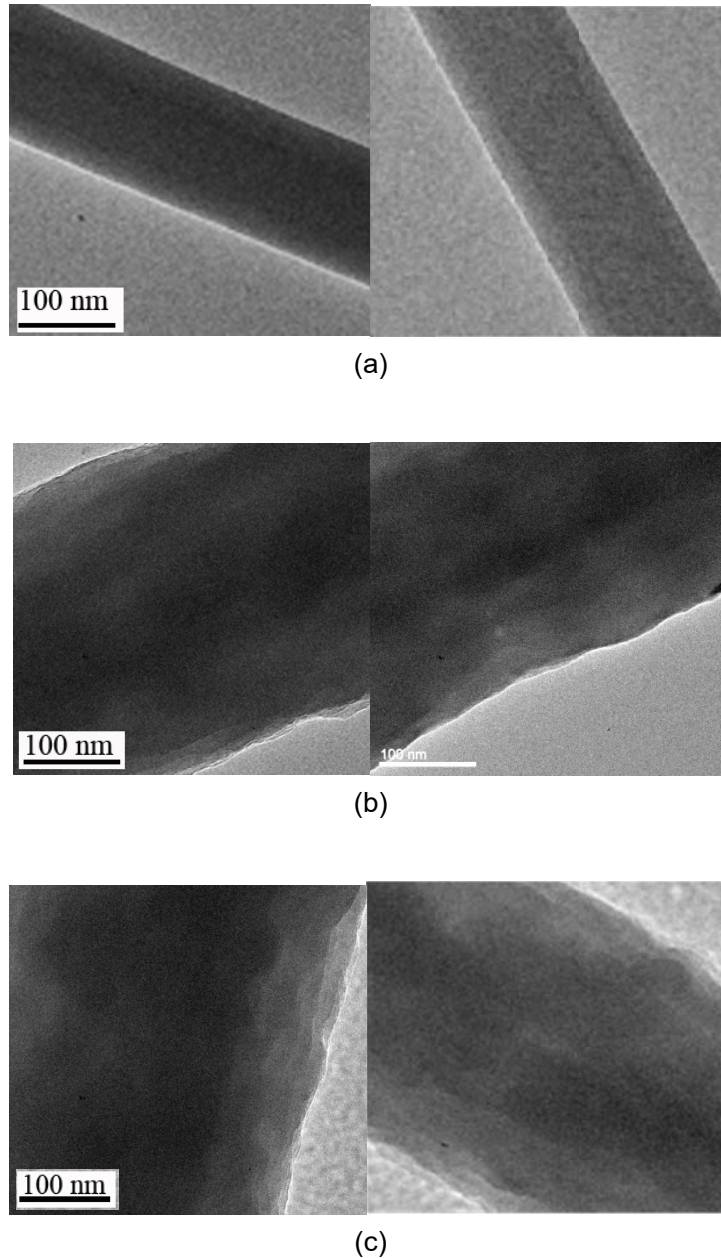


Figure 3.2 TEM micrographs of products obtained from co-axial electrospinning of PAN (core) solution and PVP (sheath) solution using applied potential of 22 kV and the distance from nozzle to collector of 22 cm, whereas the concentrations of PAN and PVP solutions are 8/10 (a), 8/13 (b), and 8/15 (c) wt%/wt%, respectively.

Miscibility of core and sheath solution is one of parameters affecting core/sheath structure of the fibers. In this research, even though it is possible to find the mixing between core and sheath solution during electrospinning, it is confirmed that miscible PAN core and PVP sheath solutions could be used for making core-sheath fibers. This can be explained by the fact that the diffusion at the boundary of core solution and sheath solution would take longer time



than the time that compound jet of solutions used for traveling to the collector. Thus, no mixing occurs at the boundary of core and sheath parts [25]. This hypothesis have been proved by some researches such as, in the preparation of miscible poly-L-lactide core and poly-DL-lactide co-axial fibers [26], in the preparation of co-axial fiber using  $\text{Ti}(\text{OiPr}_4)/\text{PVP}$  in ethanol as a sheath solution and PVP in ethanol that can be dissolved in the sheath solution as a core solution.

Considering the effects of viscosities on morphology of the co-axial fibers, when the viscosity of the sheath solution is increased higher than that of the core solution, the outer surface of the fibers becomes rough and the core-sheath structure is less defined. This can be explained by the conical flow of the solution from Taylor's cone, which develops the stress upon the interface between the core solution and the sheath solution. High viscosity of the sheath solution would produce large droplet at the end of the nozzle, which subsequently becomes conical shape after the electric potential is applied. As the result, high shear stress is introduced to the core/sheath interface leading to the mixing of the core/sheath solutions. It can be described that when high voltage is applied, the compound droplet is stretched to flow conically to form compound cone, in which shear stress developed in the sheath solution will exert on the core solution at the core-sheath interface. Large droplet yields larger angle of the Taylor's cone, which develops higher shear stress in sheath solution as well as at the interface of core-sheath.

It can be concluded that the suitable value of concentration of PAN solution for this co-axial system is 8 wt%, which provide the viscosity of around 0.2 Pa.s. The suitable viscosity of sheath solution of PVP is confirmed to be around 0.1 wt% as same as the preparation of PVP pure fibers. These viscosity values of core and sheath solutions were then chosen to use in PAN/titania or PAN/ZnO fabrication.

In addition, it can be seen from Table 3.1 that the sheath solution concentration has an influence on the size of the co-axial fibers. The increase in concentration of the sheath solution results in the increase in fiber size since the amount of sheath material is increased [27]. Hence, the increase in interaction between molecules of the sheath material, is increased, results in sheath thickness increased. Since the concentration of the core solution was kept constant, the major cause of the increase in the size of the fibers is related to that the sheath thickness increased, which is also confirmed by the decrease in core diameter to sheath thickness ratio.

Table 3.1 Ratio of the core diameter to the sheath thickness of fibers produced using different concentrations of PVP solution.

Concentration of PVP sheath solution (wt%)	Average fiber diameter (nm)	Average sheath thickness (nm)	Core diameter / Sheath thickness
10	130	26	3.2
13	340	84	2.1
15	370	97	1.9

### 3.2 Formation of PAN/TiO<sub>2</sub> core-sheath fibers

#### 3.2.1 Pre-calcination PAN/TiO<sub>2</sub>(PVP) core-sheath fibers

The preparation of PAN/TiO<sub>2</sub>(PVP) co-axial fibers is similar to that of PAN/PVP co-axial fibers. PAN (8 wt%) in DMF solution was used as the core solution, while the sheath solution was changed from PVP solution to be the solution of titania precursor, i.e., mixture of TTIP, acetic acid and DMF and PVP. Viscosity of the sheath solution was chosen from the suitable value studied in the fabrication of PAN/PVP co-axial fibers.

The viscosity of the solution of titania precursor was adjusted by varying concentration of PVP. Different concentration of PVP solution before mixing with titania sol were used for preparing different solution viscosities.

To confirm that the chosen viscosity of the sheath solution is suitable, Figure 3.3 shows the TEM image of the co-axial PAN/TiO<sub>2</sub>(PVP) fibers. The core/sheath structure can be defined clearly, even though the sheath part is not smooth as the PAN/PVP fibers. This may consider as the effect of titania precursor solution mixed with PVP solution. Furthermore, size of PAN/TiO<sub>2</sub>(PVP) fibers, which was prepared using solution with similar viscosities as that used to produce PAN/PVP fibers, is larger than that of PAN/PVP fibers. This result can be described that the titania precursor solution added in the sheath solution gives higher amount of material in solution, which makes fiber to become larger. Additionally, size of the PAN core is relatively close to that observed in PAN/PVP co-axial fiber. Therefore, a change in the sheath solution has no effect on PAN core as long as the same concentration of the core solution is used.

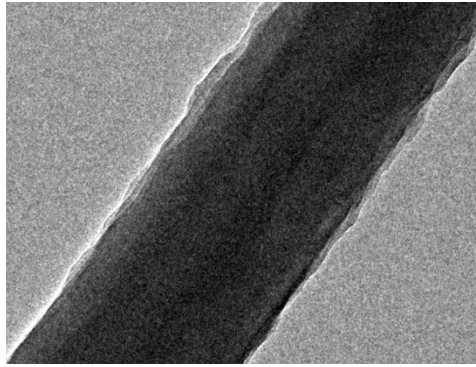


Figure 3.3 TEM of PAN/TiO<sub>2</sub>(PVP) co-axial electrospun fiber.

After the suitable condition for the solution preparation was selected for co-axial electrospinning process, the effects of processing parameters on the morphology of PAN/TiO<sub>2</sub>(PVP) as-spun co-axial fibers were studied and reported.

#### 3.2.1.1 Effects of solution flow rate

During co-axial electrospinning process, syringe pumps were used to control the solution flow rates, which would affect the electrospun fiber morphology. The effect of the flow rates of the solutions in the co-axial electrospinning process is shown in Scanning transmission electron microscopy (STEM) images in Figure 3.4. From Figure 3.4(a-c), it can be seen that the increased flow rate of the sheath solution, which consequently increases the shear stress in the solution, results in the rough surface and the mixing of two solutions in similar manner as the effect of viscosity previously discussed. When the electric potential is applied, large droplet of the sheath solution could develop high stress in the sheath solution at the interface between the core solution and the sheath solution. Size of the droplet is not only controlled by the viscosity of the solution, but also the flow rate of the solutions. The increase in the flow rate results in the increase in droplet size due to higher amount of material supplied. In addition, it can be seen from Figure 3.4(d-f) that the increase in the flow rate of the core solution, which increases the amount of supplied core material, results in the increase in the diameter of the fibers.

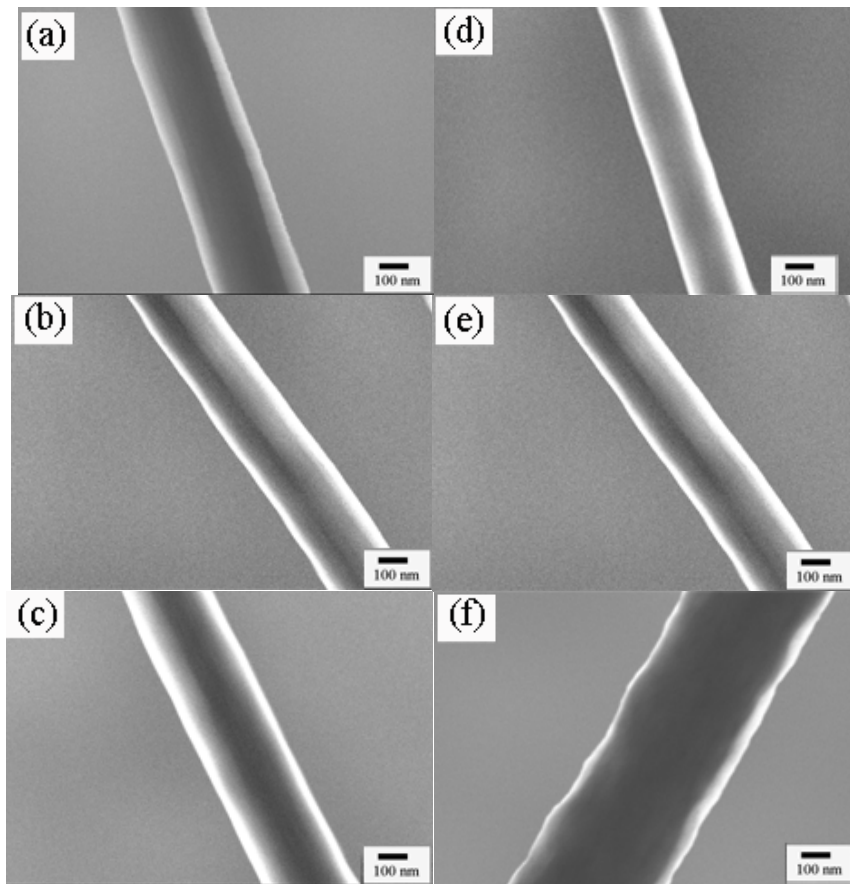


Figure 3.4 STEM images of products obtained from co-axial electrospinning of PAN solution and PVP/titania solution using applied potential of 22 kV and the distance from nozzle to collector of 22 cm, whereas the flow rate of PAN and PVP/titania solutions are 1.2/0.9 (a), 1.2/1.2 (b), 1.2/1.5 (c), 0.9/1.2 (d), 1.2/1.2 (e) and 1.5/1.2 (f) (ml/h)/(ml/h), respectively.

#### 3.2.1.2 Effects of applied potential

Another important factor that affects morphology of the electrospun fiber is the applied electric potential. In electrospinning system, stable jet of the spinning solution ejected from the Taylor's cone could be formed only when the applied potential is in suitable range.

The effect of the electric potential applied for the co-axial electrospinning depends on type of fluids used and the distance between the tip of the nozzle and the collector, i.e., working distance. Consider the PAN/TiO<sub>2</sub>(PVP) fibers fabricated, the electric potential of 20 and 21 kV could produce the fibers as shown in Figure 3.5(a) and 3.5(b) respectively. However, the fibers are not uniform in size due to the unstable jet formed during the electrospinning process. The proper electric potential for this system was found to be 22 kV, as shown in Figure 3.5(c),

in which uniform fibers without beads were produced. Distributions of the diameter of fibers are shown in Figure 3.6.

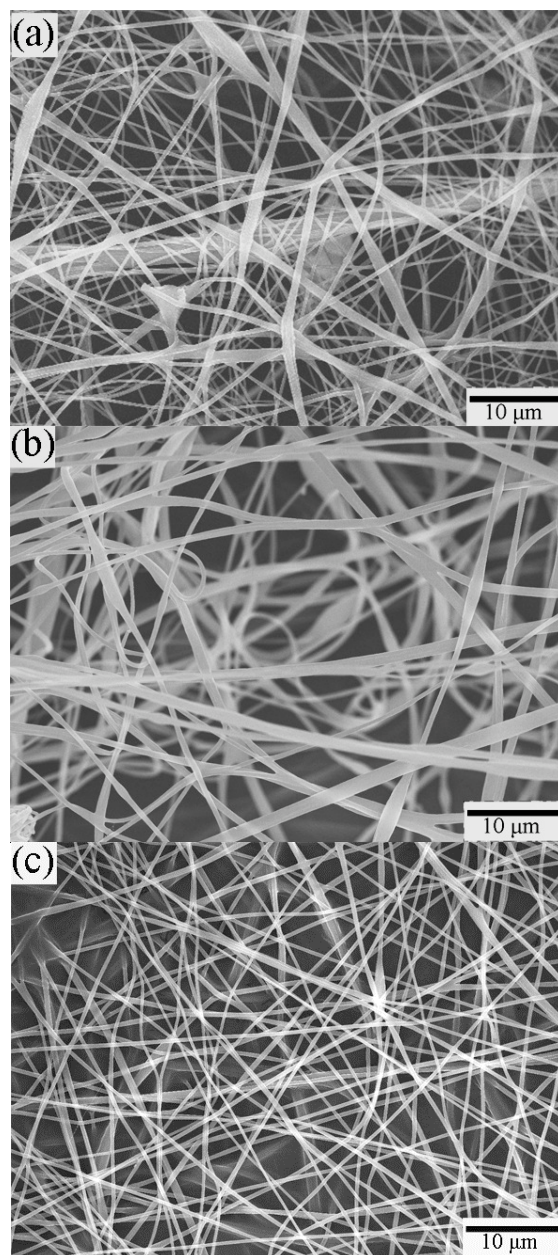


Figure 3.5 SEM images of the products obtained from the co-axial electrospinning of PAN solution and PVP/titania solution with the tip-to-collector distance of 22 cm and the applied electric voltage are 20 kV (a), 21 kV (b), 22 kV (c) respectively.

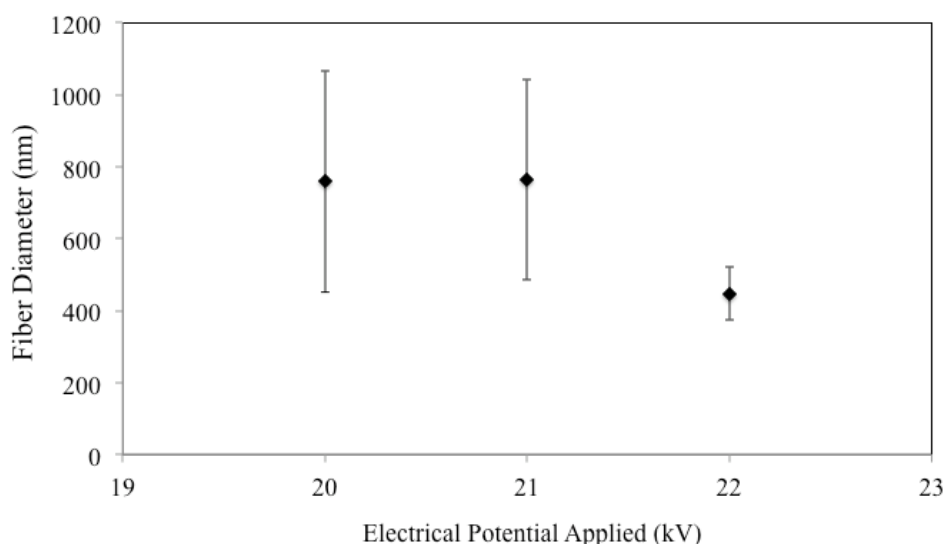


Figure 3.6 Average diameter of PAN/TiO<sub>2</sub>(PVP) co-axial fibers obtained from the co-axial electrospinning of PAN solution and PVP/titania solution with the tip-to-collector distance of 22 cm and the applied electric voltage 20 kV, 21 kV and 22 kV respectively. The error bar shows standard deviation of the data.

Generally, the average diameter of the fibers is decreased when the applied electric potential is increased. It should be noted that the change in diameter of the fibers when the applied potential is adjusted is not clear due to the presence of the beads. The decrease in size of diameter the can be explained by the fact that an increased potential heightened the electric repulsive force on the fluid jet, which consequently causes greater stretching of the solution due to the greater columbic forces in the jet as well as a strong electric field and leads to the reduction in the fiber diameter [28].

### 3.2.2 Calcined PAN/TiO<sub>2</sub> core-sheath fibers

#### 3.2.2.1 Characteristic of PAN/TiO<sub>2</sub> core-sheath fibers

To obtain PAN/TiO<sub>2</sub> co-axial fibers, calcination of as-spun PAN/TiO<sub>2</sub>(PVP) co-axial fiber is necessary. The temperature of the calcination should be high enough to remove PVP polymer in the sheath part of the fibers as well as to crystallize titania to anatase form.

The temperature of calcination was firstly determined by thermal gravimetric analysis result of the pre-calcined PAN/TiO<sub>2</sub>(PVP) co-axial fibers. Figure 3.7 shows the TGA

thermogram of PAN/TiO<sub>2</sub>(PVP) as-spun co-axial fibers being heated up to temperature of 800 °C under oxygen gas.

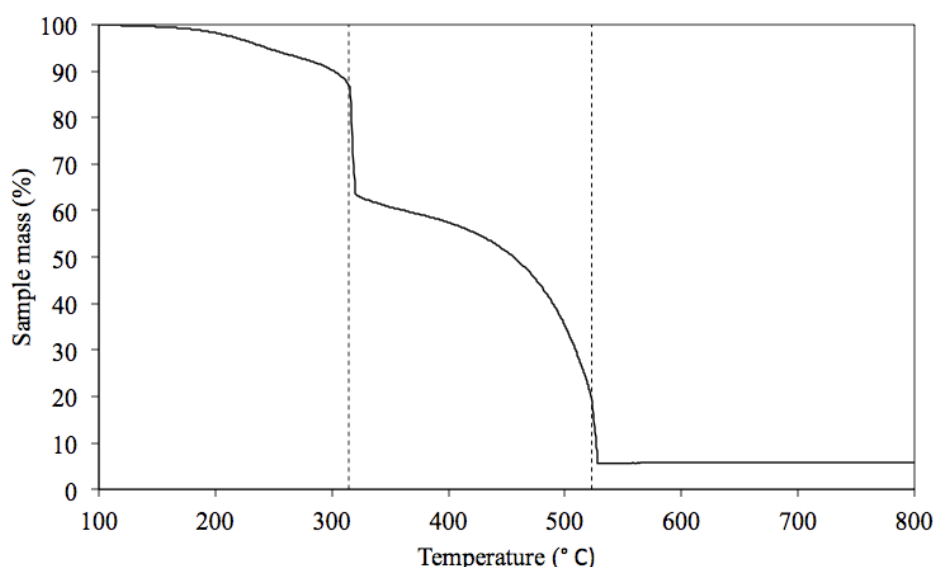


Figure 3.7 TGA curve of pre-calcined PAN/TiO<sub>2</sub>(PVP) co-axial electrospun fibers

The result shows the sample mass loss in two steps, which is similar to the degradation of PAN pure fiber. The first decrease of mass in both co-axial fibers and PAN pure fibers is at temperature around 315°C, which is around the beginning of degradation temperature of PVP. Therefore, the mass decrease at first step of co-axial fibers is expected to be the effects of the degradation of PVP and stabilization of PAN fibers.

The stabilization of PAN normally occurs when PAN is heated in air at around 300°C. In this process, some exothermic chemical reactions of cyclization oxidation and dehydrogenation occur. The rate of weight loss in the first step is quite rapid due to the dehydrogenation of PAN. Figure 3.7 shows that the decrease of mass in the first step of co-axial fibers is around 40 wt%, which is larger than the summation of mass loss of each PAN and PVP calculated separately from TGA thermogram of pure polymer fibers. It can be implied that titania has influenced the dehydrogenation of some compound [29]. Besides, the data from DSC shows that there is heat flow from exothermic reaction at the same temperature, which conforms to the dehydrogenation of PAN and the decomposition of pure PVP fiber normally decomposing at temperature around 320°C.

The second mass decrease is not rapid as in the first step, hence the mass of fibers is slowly decreased when they are heated up above 320°C. This can be explained by the partial evaporation of small compound, such as NH<sub>3</sub> and HCN from the fragmentation of polymers. At

temperature of 525°C, it is expected to be the temperature of the complete degradation of PAN and PVP in fibers. In this temperature, mass of the fibers decreases rapidly and the DSC curve confirms that the exothermic reaction occurs.

Considering the amount of titania in co-axial fibers, the TGA curve in Figure 3.7 shows the amount of titania remaining in fibers. It can be seen that the mass of the co-axial fibers is constant while being heated up at the temperature in the range of 600°C to 800°C. At 800°C, all carbonaceous materials including PAN core should be totally decomposed by reacting with oxygen gas. The temperature of complete degradation of PAN was found to be around 780°C [30]. Thus, only titania remains after heating. The amount of titania determined by TGA curve is found to be around 7 wt% of the fibers, which is less than the calculated value of 10 wt%. It might be affected from the non-uniformity of titania in the fibers.

For the calcination temperature, although PVP is decomposed at the temperature of 320°C, it still remains its mass around 50%. Consider the TG curve of the co-axial fiber, mass of fibers decreased slowly after the first step of mass lost referring to the decrease of PVP, while PAN curve is almost constant. The chosen temperature for calcination was found to be 450°C since after 450°C the second decrease of PAN is started again, which can be seen from both TG curves of co-axial fiber and PAN fibers.

As a result from TGA, the calcination temperature was chosen to be 450°C, which is high enough for removing PVP polymer from the sheath part of co-axial fibers and not too high to degrade most part of PAN core. After calcination of the electrospun fibers at 450°C for 2 h, the products remain in fiber form as shown in Figure 3.8(b) and still retains its flexibility. The flexibility of the calcined fibers implies for the presence of the PAN core.

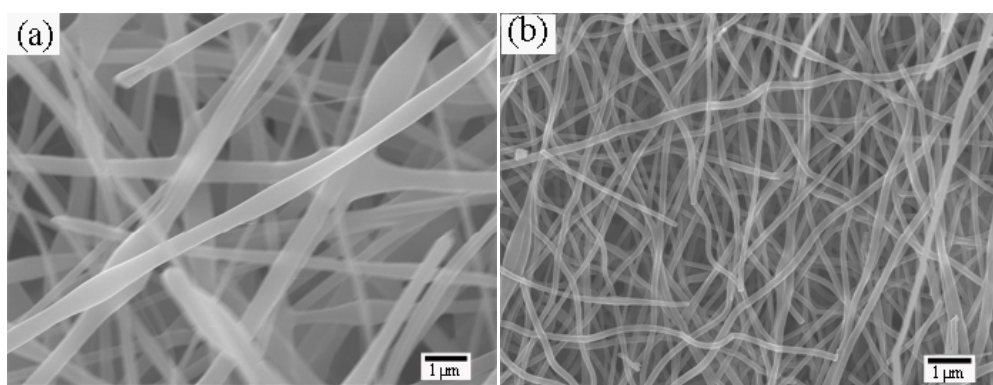


Figure 3.8 SEM images of the products obtained from the co-axial electrospinning of PAN solution and PVP/titania solution with the tip-to-collector distance of 22 cm and the applied electric voltage of 22 kV, before (a) and after calcination at 450°C for 2 h (b).



Figure 3.9 shows size distribution of co-axial fibers before and after calcination. The average diameter of the fibers decreases from 370 nm to 160 nm after calcination, which could be explained by the removal of PVP in the sheath structure of the fibers by the calcination.

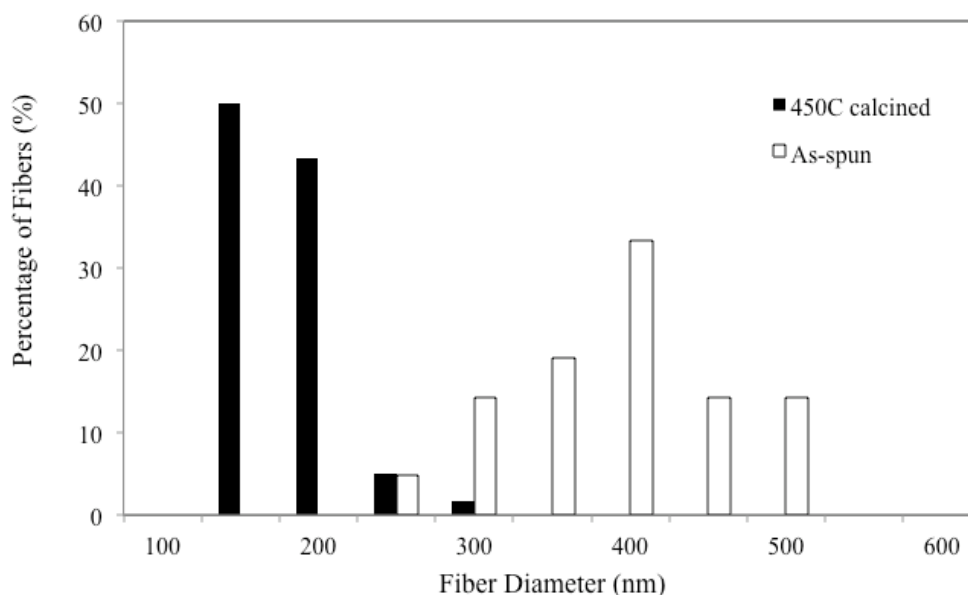


Figure 3.9 Histogram of diameter size distribution of as-spun PAN/TiO<sub>2</sub>(PVP) co-axial fibers and PAN/TiO<sub>2</sub> co-axial fibers after calcination at 450°C for 2 h.

According to the TGA analysis, when the calcination temperature is increased, mass of the obtained fiber decreases. The morphology of the products after being calcined at different calcination temperature was investigated to confirm the fiber structure during calcination process.

Figure 3.10 shows SEM images of co-axial fibers of PAN/TiO<sub>2</sub> after being calcined at 300°C, 450°C and 800°C respectively. It can be seen from the figure that all obtained fibers remain in fiber form. The as-spun co-axial fibers and the fibers after calcination at temperature of 300°C shown in Figure 3.10(a) and 3.10(b), respectively, are similar in size and morphology. This supports the TGA result that no polymer loss occurs below the temperature of 315°C. While heating up to 450°C, the fibers lost their mass according to the removal of PVP, which also results in the decrease in diameter of fibers. Finally, when the calcination temperature is raised to 800°C, both of PAN polymer and PVP polymer are removed of the fibers. Figure 3.10(d) shows the titania fibers with rough surface and having a chain-like structure, which could be affected from the removal of PAN core from the fibers.

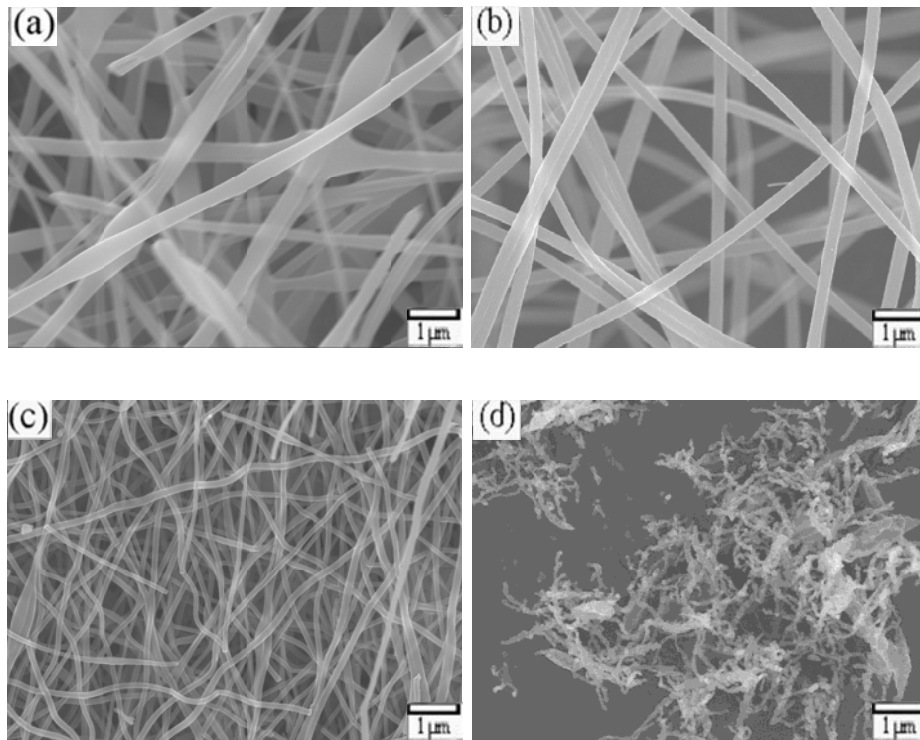


Figure 3.10 SEM images of the fibers obtained from the calcination of co-axial electrospun fiber of PAN solution and PVP/titania solution with the tip-to-collector distance of 22 cm and the applied electric voltage of 22 kV, before (a) and after calcination at 300°C (b), 450°C (c) and 800°C (d) respectively.

Furthermore, it can be seen from Figure 3.11(b) that the calcination of titania(PVP) fibers without PAN core at 800°C results in smooth fibers, which is different from the chain-like structure of the PAN/titania(PVP) co-axial fibers calcined at the same temperature. The difference in fiber structure indirectly confirms that PAN polymer was inside the fibers.

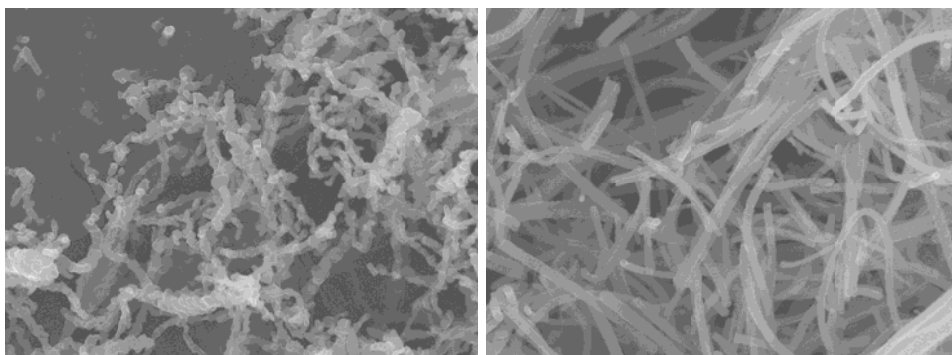


Figure 11. SEM images of 800°C calcined fibers from PAN/TiO<sub>2</sub>(PVP) co-axial fibers (a) and from TiO<sub>2</sub>(PVP) simple fibers (b).

Figure 3.12 shows the average diameter of co-axial fibers after being calcined at different temperatures. The average fiber diameter does not change much at the calcination temperature of 300°C, which is lower than the degradation temperature of both PVP and PAN. The decrease in the average diameter of the co-axial fibers is clearly observed when the calcination temperature is increased from 300°C to 450°C, which was found to be the range for PVP removal. After the calcination at 800°C, the average diameter of fibers is decreased to be as low as 50 nm, which is expected to be the diameter of the residual titania fibers.

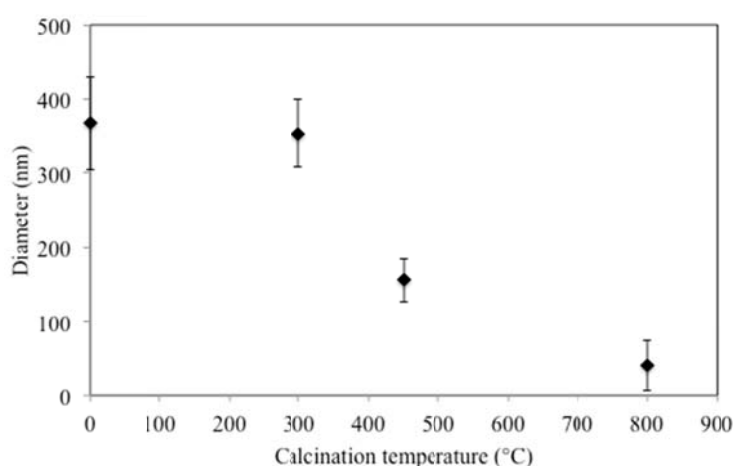


Figure 3.12 Diameter size with deviation of PAN/TiO<sub>2</sub>(PVP) co-axial fibers at different calcination temperature.

Another way to confirm the core-sheath structure of the fibers is the observation of the fiber cross section. TEM images of the cross-section of PAN/titania (after calcination at 450°C) co-axial fibers are investigated. It can be seen from Figure 3.13 that a core polymer is covered with titania particles. The particles are quite uniform with an average particle size of 4.3 nm and a standard deviation of 0.8 nm. For cross section sample preparation, it is necessary to cut the fibers by microtome. As the glass temperature transition ( $T_g$ ) of PAN is around 100°C [30], which is higher than the temperature while cutting the fibers for cross-sectional observation. Therefore the non-circular shape observing from TEM image Figure 3.13(b) is considered not to be the deformation of polymer core while cutting. Nevertheless, it is expected to be the difference plane of cut fiber, which results in the oval shape of cross sectional of fiber in TEM image.

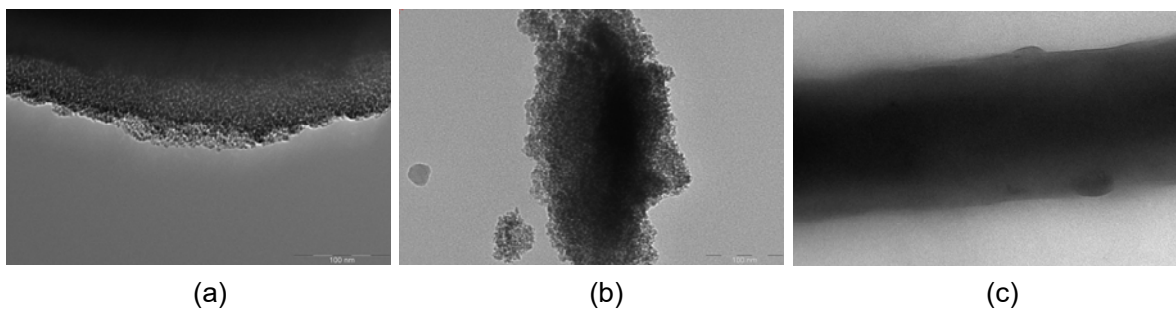


Figure 3.13 TEM image of cross-section of PAN/titania co-axial fiber (a-b), and PAN/titania coaxial fibers (c).

For this reason, core size observed from the cross section image, which is shown in Figure 3.13(b), is not exactly same as that shown in Figure 3.13(c) of co-axial PAN/titania. The fiber in the Figure 3.13(c) has a diameter of around 200 nm and in a cylindrical shape, which is difficult to see the titania grains in the sheath part clearly. Moreover, there is an objective lens below the sample and electrons of different energies are focused at different focal positions in TEM resulting in the well-known effect of chromatic aberration. This leads to blurring of the image and a loss of resolution and contrast. However, the difference between core and sheath parts still can be seen from this TEM image that the fibers. Beside, both core sizes observed from two ways are in a range of 80 to 100 nm.

To confirm that core remaining in the fibers after calcination is PAN, the functional groups of electrospun products before and after calcination at 450°C were investigated by FT-IR.

According to Figure 3.14(a), FT-IR spectra of as-spun PAN shows a signal corresponding to  $\text{C}\equiv\text{N}$  stretching at wavenumber around  $2244\text{ cm}^{-1}$ , besides, the bands at wavenumber around 2850, 2939, 1444, 1353, and  $1253\text{ cm}^{-1}$ , which are assigned to the aliphatic CH group vibrations of different modes in CH,  $\text{CH}_2$  and  $\text{CH}_3$ , respectively [30] are also observed. It can be seen from Figure 3.14(b-d) that when the calcination temperature is raised, the bands of aliphatic CH group vibrations are decreased due to the partial evaporation of small molecule from the polymers. Moreover, Figure 3.14(b-c) confirms the stabilization of PAN fibers when the fibers are heated up to 300°C, which is previously explained in TGA/DSC thermogram. One of the most important reactions in the stabilization is cyclization, which is the reaction producing stable ladder polymer as shown in Figure 3.15. The cyclization can be confirmed by the fact that the intensity of  $\text{C}\equiv\text{N}$  stretching band is decreased when the calcination temperature is increased from 200°C to 350°C as shown in Figure 3.14(b-c), while

new peak assigning to the stretching bond of C=N is presented at wavenumber of  $1590\text{ cm}^{-1}$ . Further heating up results in the conjugation in cyclic structure of PAN forming aromatic ring [31], which is confirmed by the band of aromatic C=C at wavenumber of  $810\text{ cm}^{-1}$  appearing in Figure 3.14(c-d).

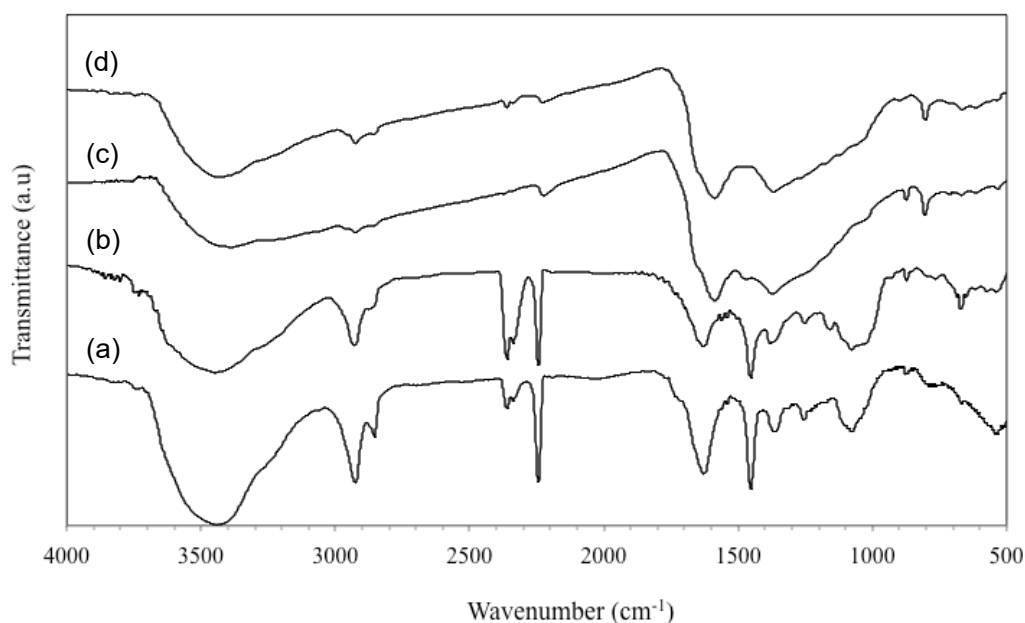


Figure 3.14 FT-IR spectrum of PAN as-spun fiber (a) and PAN pure fiber after calcination at  $200^{\circ}\text{C}$  (b),  $350^{\circ}\text{C}$  (c) and  $400^{\circ}\text{C}$  (d) respectively.

The band at  $1630\text{ cm}^{-1}$ , which appears only in the spectrum of as-spun fiber and fibers calcined at  $200^{\circ}\text{C}$  is assigned to be the stretching of C=O bond from the DMF solvent, which remains in fibers. The decrease of doubles peaks at  $2340$  and  $2360\text{ cm}^{-1}$  can be observed in the spectrum, which are assigned to be the decrease of the absorption of  $\text{CO}_2$ .

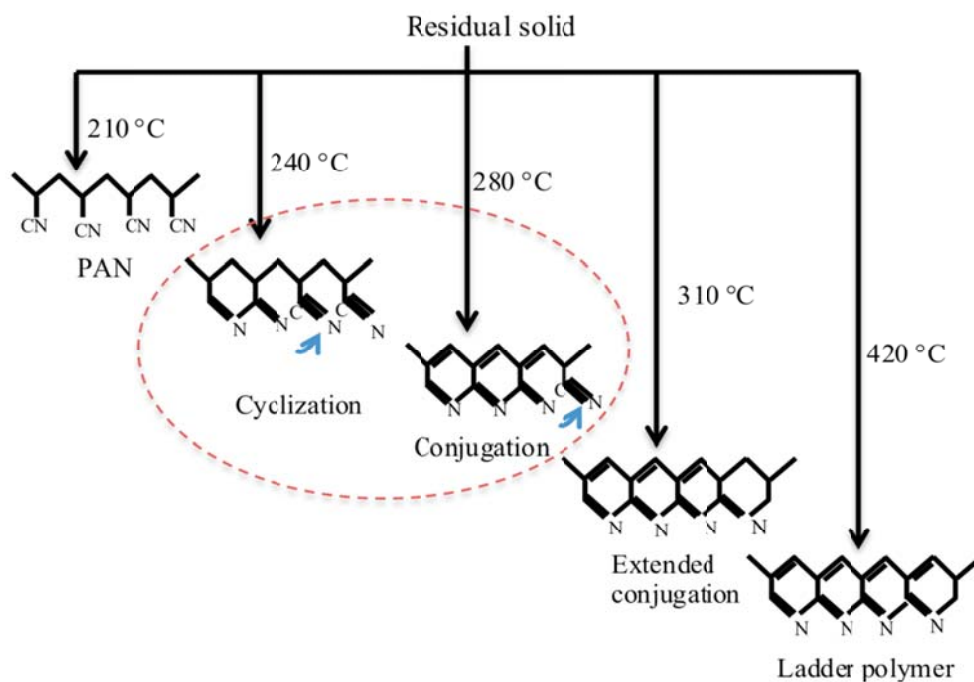


Figure 3.15 The possible degradative path and cyclization of PAN heated at various temperature [31].

From Figure 3.16(c-d), FT-IR spectra of PAN/titania co-axial fibers is almost same as the spectra of PAN pure fiber after being calcined at 400°C. It can be learned from this result that PAN in the core of fibers remains in the stable ladder polymer form after the calcination of the co-axial PAN/TiO<sub>2</sub>(PVP). However, the change of PAN does not affect the flexibility significantly, since the modified PAN is still a polymer. As the objective of this research is to synthesis the flexible fibers of titania, thus the change in molecular structure of PAN after calcination is acceptable. On the other hand, PVP in the sheath is removed after calcination as noticed in the absence of C=O bond at wavenumber of 1630 cm<sup>-1</sup>.

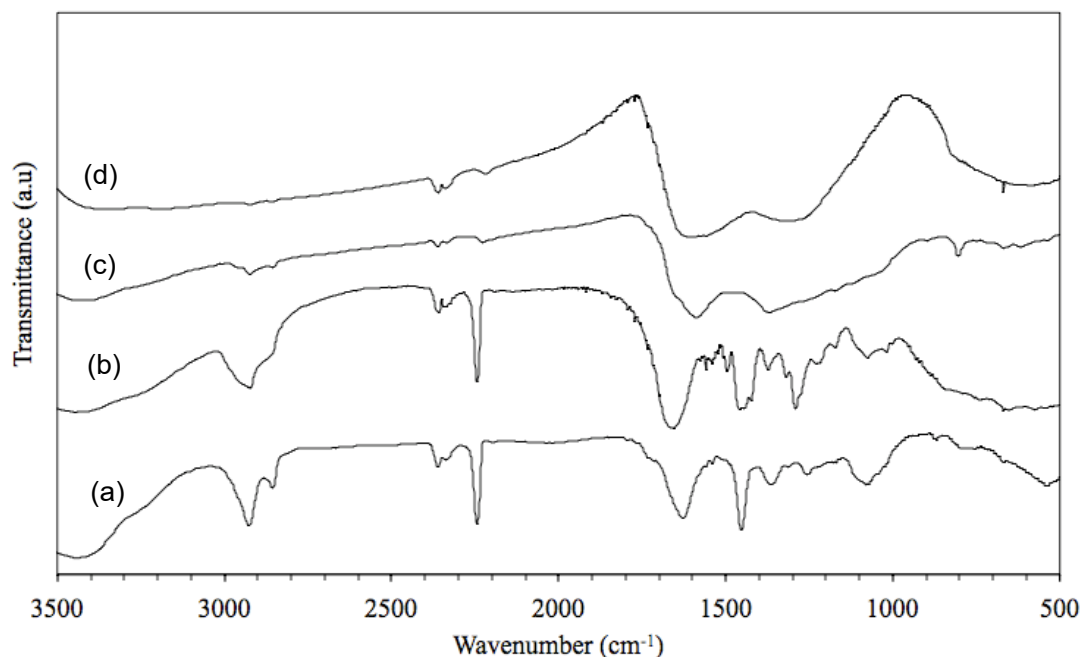


Figure 3.16 FT-IR spectrum of (a) as-spun PAN pure fibers, (b) as-spun PAN/TiO<sub>2</sub>(PVP) co-axial fibers, (c) PAN pure fiber after calcination at 450°C, and (d) PAN/titania co-axial fibers after calcination at 450°C.

According to the low content of titania in the fibers, the FTIR spectra of PAN/titania co-axial fibers shows the band corresponding to PAN predominantly. Beside, the FT-IR spectrum of the fiber after calcination shows the similar band to that of PAN fiber after calcination, thus only the change of polymers occurs without the interaction between core material and sheath material.

After confirming that the PAN/titania co-axial fibers can be fabricated, the crystal structure of titania was investigated by X-ray diffraction (XRD). It can be confirmed that the calcination temperature of 450°C is high enough to crystallize TiO<sub>2</sub> in the co-axial as-spun fibers to anatase as shown in Figure 3.17(a). The XRD patterns in Figure 3.17(a-b) show the presence of both anatase and rutile phases in the core-sheath products after the calcination. The fraction of anatase and rutile within the fibers depends on the temperature of calcination. The calculated content of rutile phase is increased from 0.34 to 0.4 with the increase in the calcination temperature from 450°C to 500°C respectively.

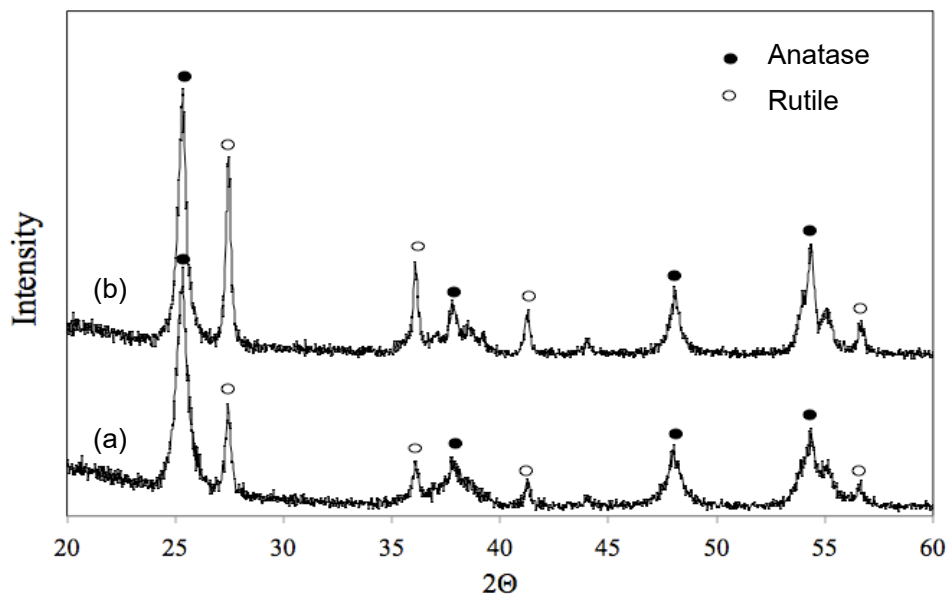


Figure 3.17 XRD patterns of the PAN/TiO<sub>2</sub>(PVP) core-sheath fibers calcined for 2 h at 450°C (a), and 500 °C (b) respectively.

Furthermore, it was found according to Figure 3.18 that the presence of DMF in the sheath solution also contributes to the formation of rutile phase. When ethanol was used as the solvent instead of DMF in the fabrication of PVP/titania nanofibers, only anatase phase is observed, as shown in Figure 3.18(a). Organic species, i.e., DMF in this case, induced the formation of smaller dimensions of the crystallites that leads to the decrease in the anatase-to-rutile phase transformation temperature [32]. It was proposed that organic solvent would produce the small crystallite of titania by reprecipitation effect leading to the decrease of phase transformation temperature. It was not clear about the reason why smaller crystallite size reduces the transformation temperature [33], only the experimental results shows that small crystallite size obtained. Therefore, further study about the mechanism of phase transformation in organic solvent added system is recommended.



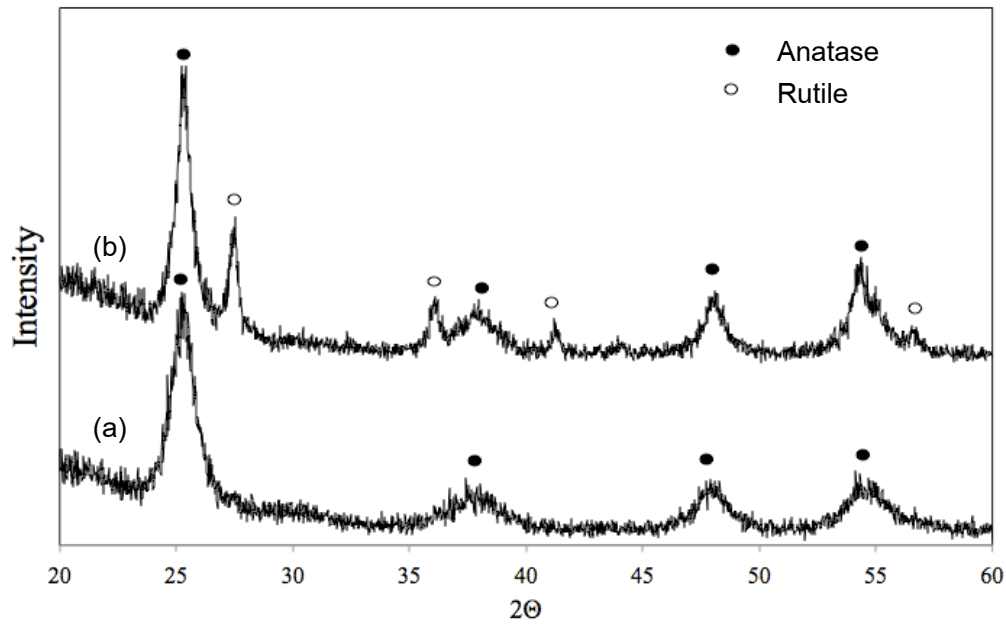


Figure 3.18 XRD patterns of the calcined PVP/titania fiber at 450°C for 2h using EtOH (a), DMF (b) as a solvent in the spinning solution.

### 3.2.2.2 Flexibility of PAN/TiO<sub>2</sub> core-sheath fibers

Tensile strength of the fibers was analyzed to confirm flexibility of the co-axial fibers. Figure 3.19 shows stress-strain curves of PAN/TiO<sub>2</sub>(PVP) co-axial as-spun fibers and that of PAN/titania co-axial fibers obtained after calcination at 450°C for 2 h.

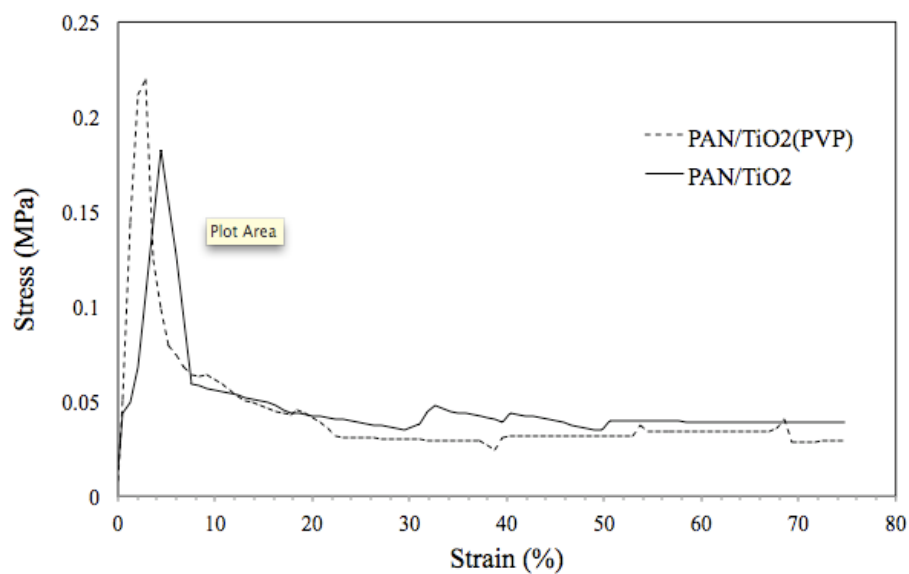


Figure 3.19 Stress-strain curves of PAN/TiO<sub>2</sub>(PVP) as-spun co-axial fibers and PAN/TiO<sub>2</sub> co-axial fibers.

Both fibers give the same pattern of curves having two regions, which represent the elastic region and plastic region. In elastic region, stress and strain are proportional. In this case, when a stress is applied and then removed, the fibers move back to their original position. For plastic region, permanent deformation occurs when stress is applied in this region. The curve starts from a linear elastic region reaching to the yield point, followed by a drop in stress, deformations of specimens of fibers, which is in the plastic region and finally fracture. This pattern represents a semi-crystalline polymer, which is consistent with property of PAN. Thus, it is confirmed that PAN core retains its mechanical properties, i.e., tensile strength, which refers the strength of the fibers. The measurement shows stress-strain curve of the sample. As seen in the curve of both as-spun fibers and calcined fibers, the plastic region is still existed. This result informs that the fibers can be bent before its fracture, which is different from pure titania fibers that easy to be crumble in to powder. In addition, the fibers can absorb tensile force even the fibers are not align in the same direction, thus the fibers can absorb force from any directions confirming its flexibility both before and after calcination.

### *3.3 Formation of PAN/ZnO core-sheath fibers*

#### *3.3.1 Effects of various parameters on the PAN/ZnO core-sheath fibers*

In addition to parameters already investigated in the fabrication of PAN/TiO<sub>2</sub> core-sheath fibers, other factors were also investigated. Their effects will be discussed on both as-spun and calcined fibers.

##### *3.3.1.1 Effect of polymer viscosity*

Viscosity plays an important role in achieving successful co-axial electrospinning. The viscosity of either core or sheath solution can be controlled by controlling molecular weight or concentration of the polymer in the solution. However, in this work, the molecular weight of the polymers was fixed. Figure 3.20 shows viscosity as a function of polymer concentration.

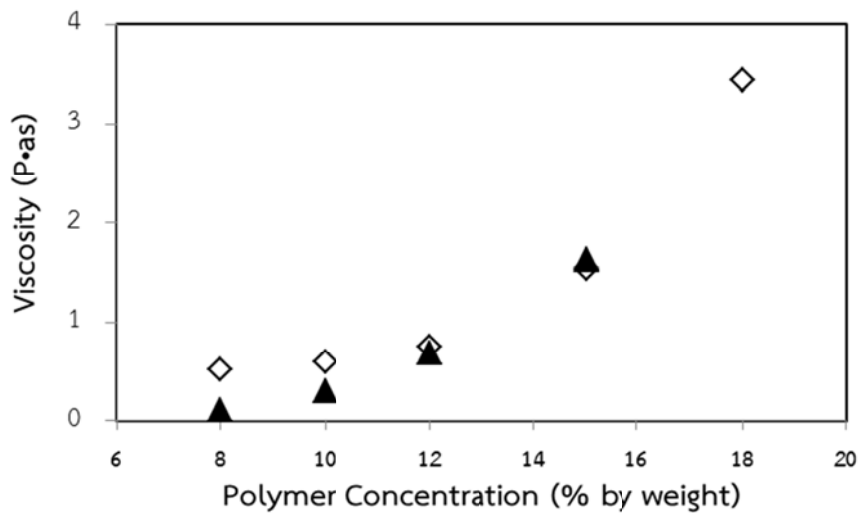


Figure 3.20 Viscosity of PAN solution (▲) and sheath solution (◇) as functions of polymer concentration.

The viscosity of sheath solution is required to be higher than the viscosity of core solution [23]. The comparison between the lower and the higher viscosity of sheath than that of core solution in Figure 3.21(a) shows that the lower viscosity of sheath solution than that of core solution could not lead to successful fabrication of the co-axial structure. On the other hand, the co-axial structure could be formed using the sheath solution with higher viscosity than that of core solution as shown in Figure 3.21(b). The viscosity of the sheath solution is critical [34, 35]. A sufficiently high viscosity of the sheath solution, such that the viscous stress imparted by it on the core solution needs to overcome the interfacial tension between the two solutions, is needed to form the compound Taylor cone and the subsequent compound jet [23].

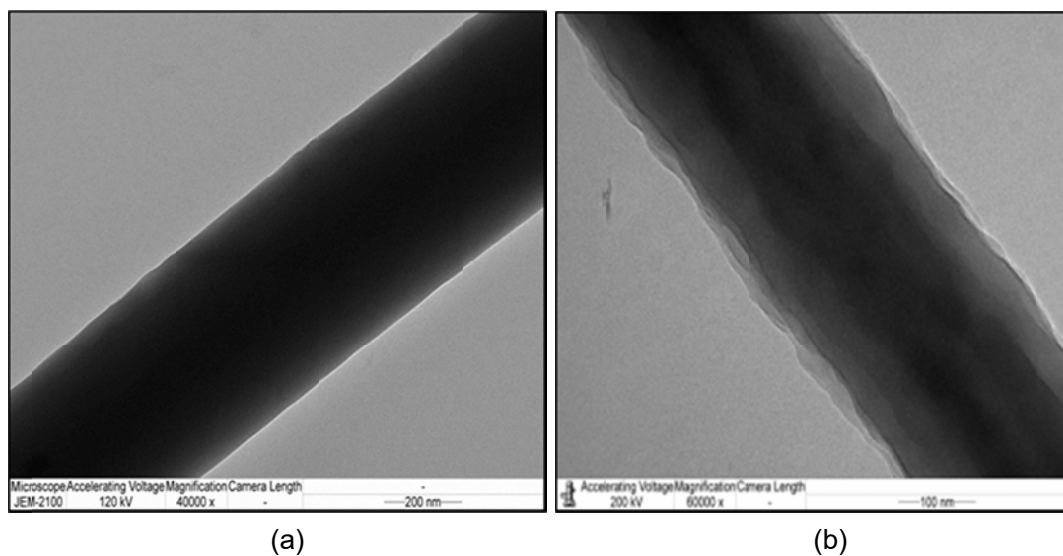


Figure 3.21 The comparison of the co-axial structure between using the sheath solution with lower viscosity (a), and with higher viscosity (b) than that of core solution.

### 3.3.1.2 Effect of PVP concentration in sheath solution

In this study, the concentration of PVP in the sheath solution was varied from 8% to 18% by weight, which corresponds to the viscosity in the range of 0.52 to 3.43 P.s, respectively. As shown in Figure 3.22, the diameter of the as-spun fibers tends to gradually rise as the PVP concentration is increased. It should be noted that the concentration of PAN in the core solution, the feeding rate and the applied potential were fixed at 8 wt%, 0.8 ml/h, and 1 kV/cm, respectively. The average diameter of as-spun co-axial fibers is in the range of  $403 \pm 73$  to  $516 \pm 93$  nm. It can also be noted that this effect remains even after calcination. It is indicated that the interaction between the viscosities of the sheath and the core solutions controls the shape of the composite Taylor cone. From this reason, although the concentration of PAN in the core solution was fixed, the diameter of the core is still affected by the concentration of the PVP in the sheath solution. Size distributions of the co-axial nanofibers before and after being calcined at 450°C and 500°C are shown in Figure 3.23.

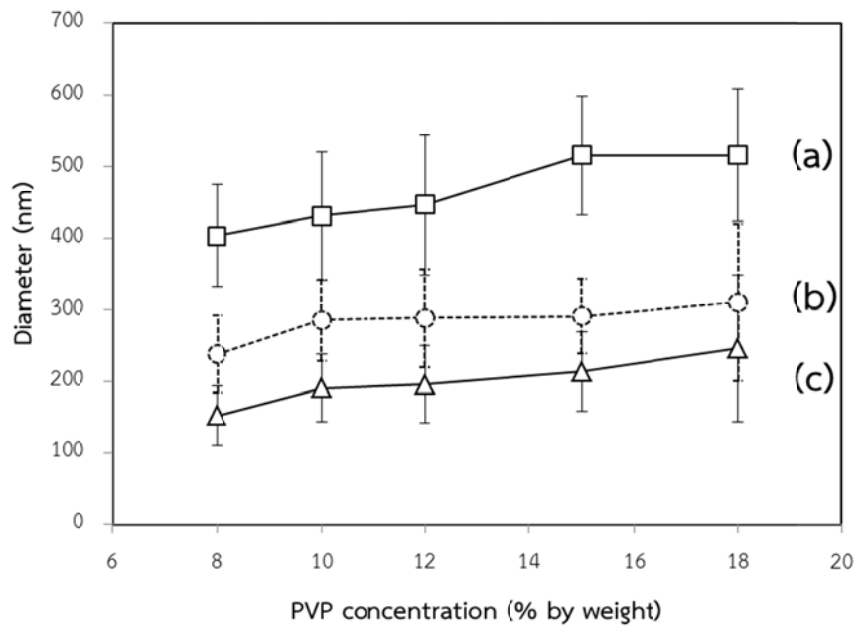


Figure 3.22 Diameters of co-axial nanofibers as the concentration of PVP in sheath solution is varied, while that of PAN in core solution is fixed at 8 wt%: (a) before being calcined, and after being calcined at (b) 450°C, and (c) 500°C.

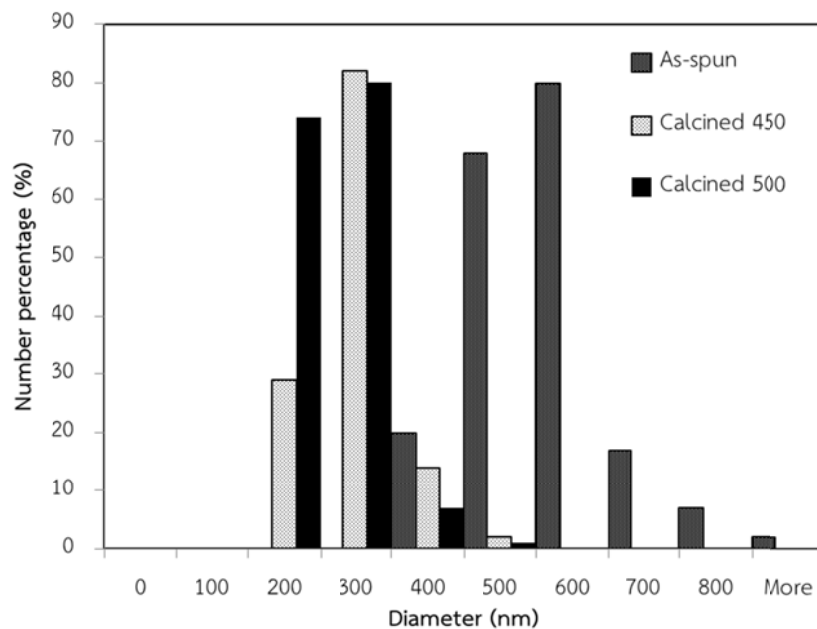


Figure 3.23 Size distribution of co-axial nanofibers before and after it had been calcined at 450°C and 500°C.

### 3.3.1.3 Effect of PAN concentration in core solution

In this study, the PAN concentration was varied from 4 to 12% by weight, while the concentration of PVP in the sheath solution was fixed at 12 wt%. The products using PAN concentration lower than 8 wt% are beaded fibers. On the other hand, for the PAN concentration in the range of 8-12 wt%, smooth fibers are obtained. The effect of PAN concentration on size of the as-spun fibers is shown in Figure 3.24. The size is sharply increased when the PAN concentration is increased from 10 to 12%. It should be noted that the feeding rate and the electric field were fixed at 0.8 ml/h and 1 kV/cm, respectively. The average diameter of as-spun co-axial fibers is in the range of  $447 \pm 98$ ,  $866 \pm 234$ , and  $3407 \pm 816$  nm when the PAN concentration used is 8, 10 and 12%, respectively. It should be point out that, when compared with the effect of PVP concentration in the sheath solution shown in Figure 3.22, changing in PAN concentration affects size of the fibers more dramatically.

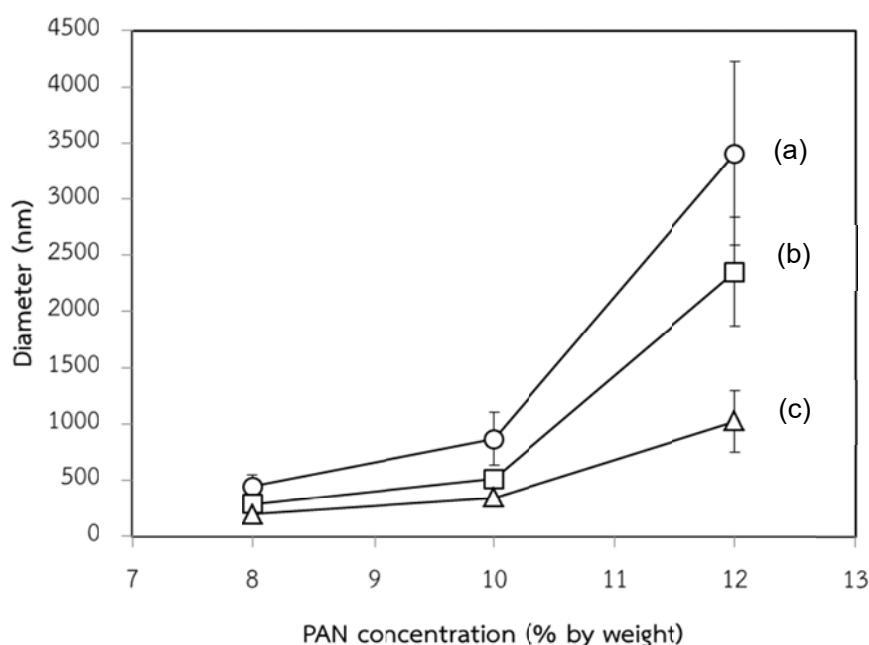


Figure 3.24 The diameters of co-axial nanofibers as the concentration of PAN in core solution is varied, while that of PVP in sheath solution is fixed at 12 wt%: (a) before being calcined, and after being calcined at (b) 450°C, and (c) 500°C.

The results from varying polymer concentration in both core and the sheath solutions indicate that the increase in the core concentration increases overall fiber diameters more significantly than the increase in the sheath concentration. So the PAN concentration is the significant factor to predict the diameter of co-axial fibers.

### 3.3.2 Characteristic of PAN/ZnO core-sheath fibers

The thermal-gravimetric (TG) and differential scanning calorimetry (DSC) diagrams for as-spun co-axial nanofibers are shown in Figure 3.25. There are four-gravimetric steps. The first step is broad range between 54 and 110°C, corresponding to about 9.22% weight loss, due to the volatilization of HCl and physio-sorbed water of which the boiling points are 57 and 100°C respectively. The second step is between 110 and 351°C, corresponding to about 29.95% weight loss, accompanied by a strong thermopositive peak at 280°C in DSC curve. It is probably due to the partial decomposition of PVP in the sheath, partial decomposition of PAN in the core structure, and removal of other organic matters such as DMF and diethanolamine, which has boiling point of 152, and 259°C respectively. The third step is accompanied by about 24.83% weight loss locating at around 351-477°C. This is due to the decomposition of polymer such as PVP and part of PAN according to reports by many researches about the decomposition temperature of PVP (molecular mass of 1,300,000) and PAN (molecular mass of 150,000) in the range of 250-420°C [36, 37] and 350-500°C [30] respectively. It should be noted that the results correspond with TG-DSC data of pristine PAN and PVP fibers. The forth step is around 510°C, corresponding to about 25.33% weight loss, accompanied by a sharp thermopositive peak in the DSC curve. This step corresponds to the main decomposition of PAN core polymer.

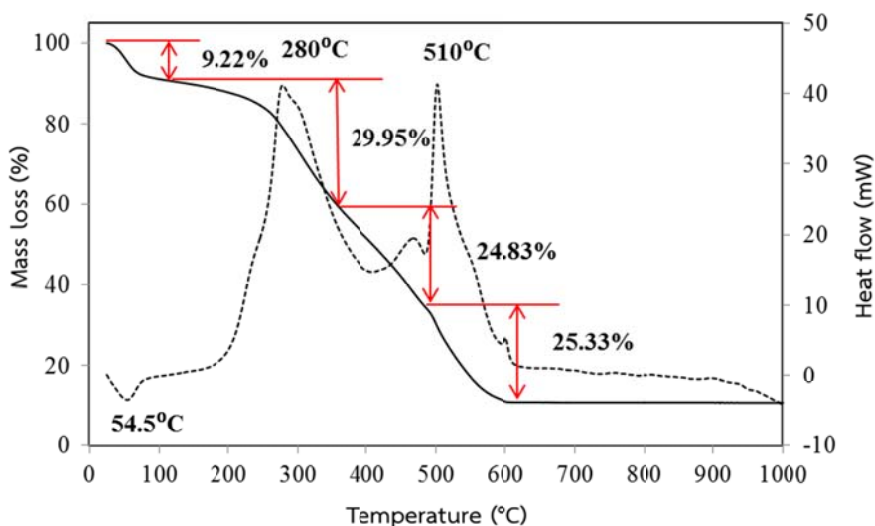


Figure 3.25 Thermal gravimetric analysis (TGA) and differential scanning calorimetry (DSC) of the as-spun ZnO/PAN co-axial fibers

According to the TG-DSC diagram shown in Figure 3.26, for ZnO/PAN co-axial nanofibers after calcination at 450°C, the TG graph shows a significant mass loss about 85%, accompanied by a strong thermopositive peak at 523°C which is due to the removal of residual PAN in the fibers.

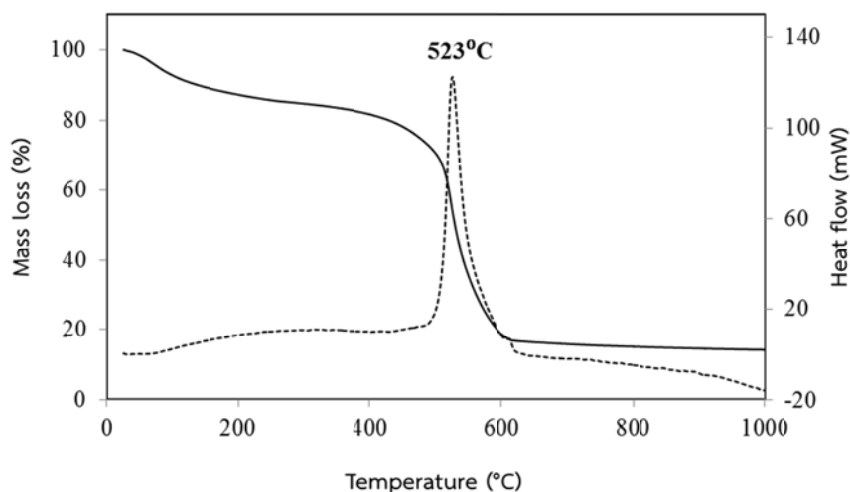


Figure 3.26 Thermal gravimetric analysis (TGA) and differential scanning calorimetry (DSC) of ZnO/PAN co-axial nanofibers after calcination at 450°C for 2 h.

According to TG-DSC results in Figure 3.25 and 3.26, there is no significant weight loss at temperature higher than 600°C, indicating the completion of ignition loss from the organic constituent and the remainder corresponding to ZnO. The TG-DSC analysis shows the significant constraint of the calcination temperature to remove PVP in the sheath while keeping PAN in the core to sustain flexibility of final ZnO nanofibers. The proper calcination temperature is considered to be the range of 400 to 500°C. Nevertheless, it must also be considered that the calcination temperature should be high enough to convert amorphous ZnO to crystalline ZnO. So, as a result from TGA, the calcination temperature was chosen to be 450°C for 2 hours. After calcination, the products remain in fiber form with co-axial structure characterized from electron microscopy is shown in Figure 3.27.



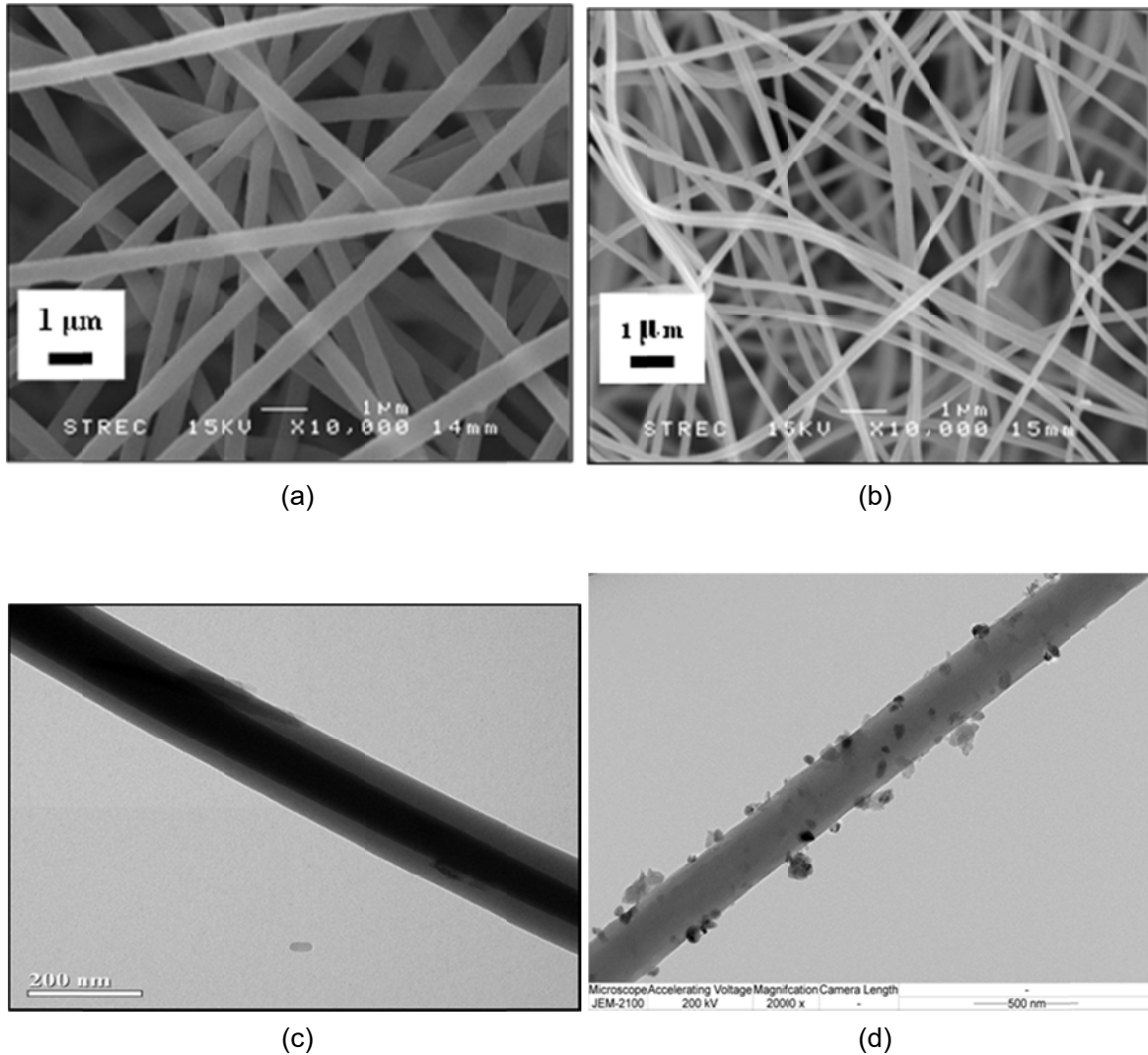


Figure 3.27 Electron microscopy images of co-axial nanofibers with 15% PVP sheath and 8% PAN core; SEM images of (a) fibers before calcination, (b) fibers after it had been calcined at 450°C and TEM images of; (c) fibers before calcination, (d) fibers after it had been calcined at 450°C.

The nitrogen adsorption-desorption analysis of ZnO/PAN co-axial fibers after the calcination reveals type III isotherm according to IUPAC classification, which is a typical characteristic adsorption-desorption isotherm of nonporous material. The specific surface area measured is  $4.8 \text{ m}^2/\text{g}$ , which is in the same order of magnitude as the ZnO powder synthesized by the same sol-gel technique ( $2.9 \text{ m}^2/\text{g}$ ). Nevertheless, it should be noted that the specific surface area of the PVP/PAN co-axial fibers (i.e., without ZnO) after calcination at 450°C is 5.2

$\text{m}^2/\text{g}$ . Hence, part of the surface area of the ZnO/PAN co-axial fibers might be contributed by the carbon from the polymer core.

The presence of crystalline ZnO in the ZnO/PAN core-sheath fibers was confirmed by XRD, as shown in Figure 3.28. The ZnO nanocrystals are in Wurtzite (hexagonal) phase. The crystallite size of the ZnO phase calculated by the Debye-Scherrer was found to be 21 nm.

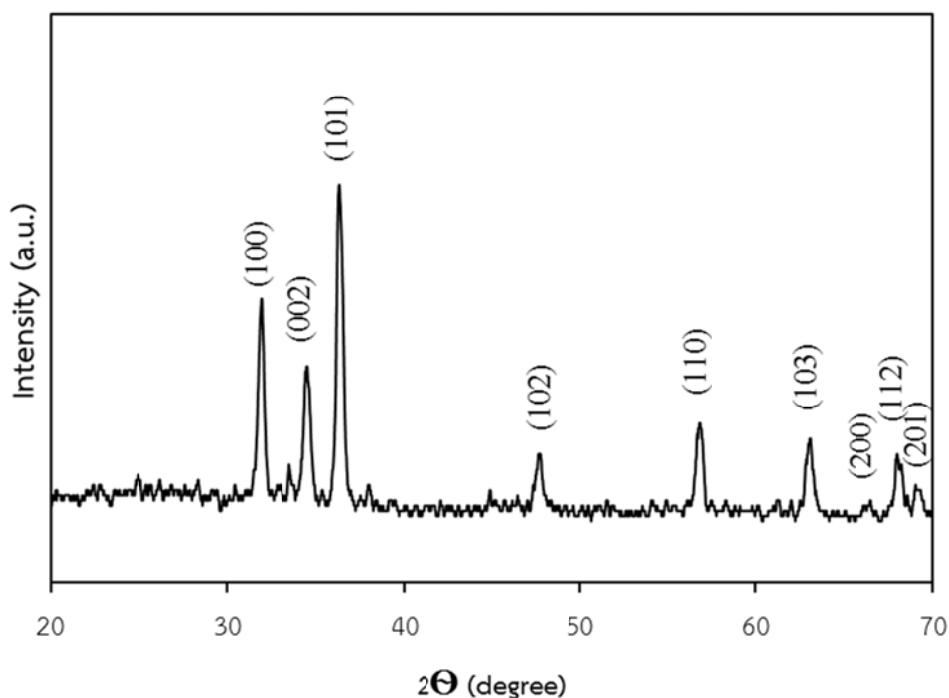


Figure 3.28 XRD pattern of ZnO/PAN nanofibers after calcination at 450°C for 2 hours.

The grain size of the ZnO crystals was measured from TEM to be about  $65 \pm 10$  nm (see Figure 3.29). The clear lattice fringe in HRTEM image and the SAED pattern suggest that ZnO particles distributing on the PAN core are single crystalline. It should be noted that the lattice spacing measured from the HRTEM image is  $2.586 \pm 0.145$  Å, which corresponds to (002) plane of ZnO.

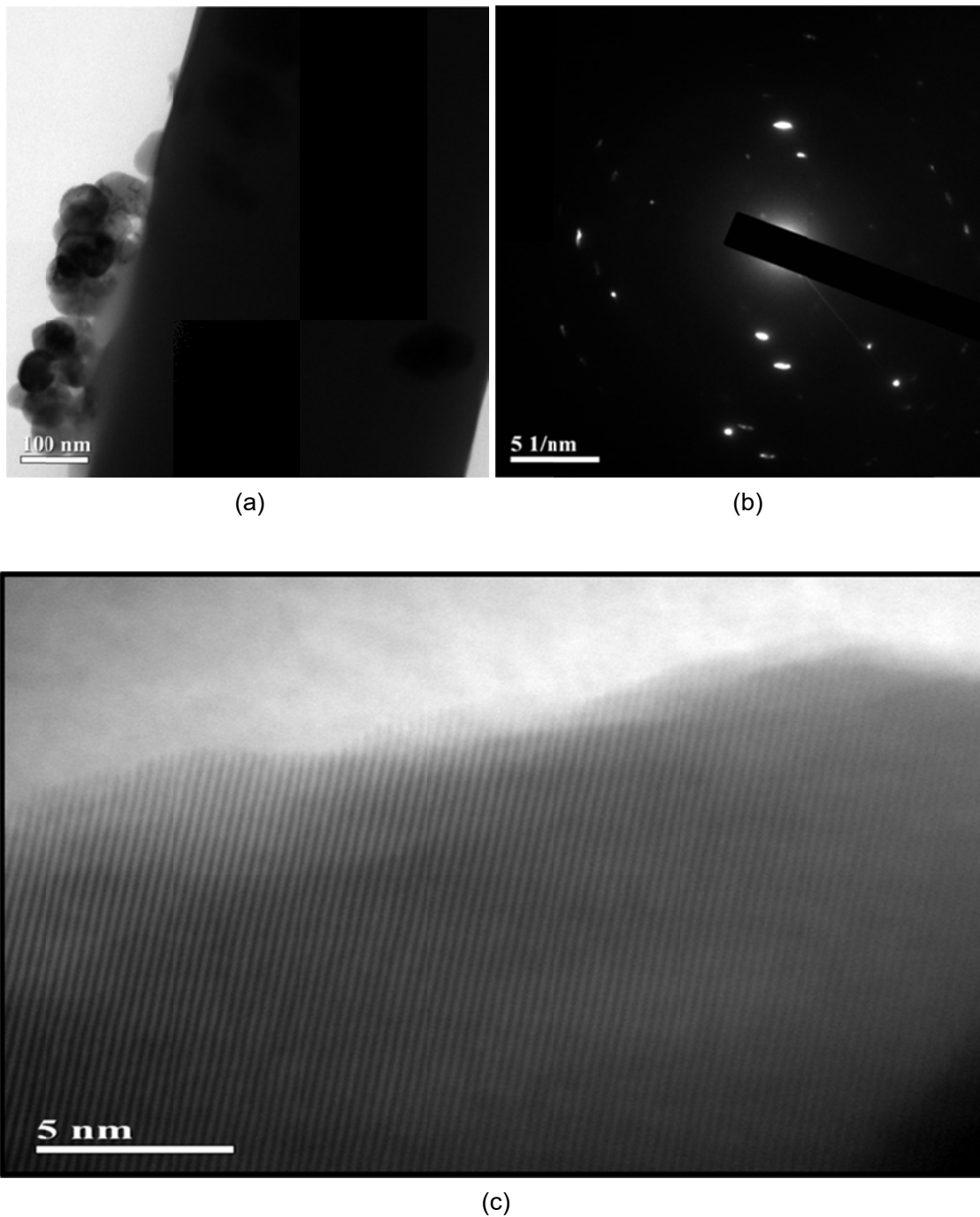


Figure 3.29 TEM image of (a) ZnO nanocrystals distributing on nanofibers after calcination at 450°C for 2 hours, (b) SAED pattern, and (c) HRTEM image showing lattice fringes of ZnO.

Figure 3.30 shows the FT-IR spectra of PAN nanofibers calcined at different temperatures. The vibration characteristic of PAN pristine fibers are those of  $\text{C}\equiv\text{N}$  nitrile group at about  $2,243\text{--}2,241\text{ cm}^{-1}$ , and the bands in regions of  $2,925\text{ cm}^{-1}$ ,  $1,450\text{ cm}^{-1}$ ,  $1,361\text{ cm}^{-1}$  and  $1,254\text{ cm}^{-1}$  are assigned to the aliphatic CH group vibrations of different modes in CH,  $\text{CH}_2$ , and

CH<sub>3</sub>, respectively [38, 39]. As the calcination temperature is increased, the most prominent structural changes were the decrease in the intensities of the 2,243-2,241 cm<sup>-1</sup>, attributed to C≡N band, and also the decrease of those for aliphatic C-H ones, concomitant with the advent and increase of a shoulder-like peak around 1,700 cm<sup>-1</sup> due to cyclic C=O. These shoulders are assigned to the free ketones in hydronaphthyridine rings and the conjugated ketones in acridone rings, resulting from the oxygen uptake reaction [40]. Peaks around 1,590 and 1,620 cm<sup>-1</sup> corresponds to C=N, C=C, N=H mixed in-plane bending of the ladder frame, and the band at 810 cm<sup>-1</sup> due to C=C-H (aromatic ring) [41]. The latter may correspond to a side reaction taking place in the process. With the progression of the stabilization, the magnitudes of the band at 810 cm<sup>-1</sup> from (=C—H) is increased, while that of signal for methylene (CH<sub>2</sub>) at 1,450 cm<sup>-1</sup> is decreased [42].

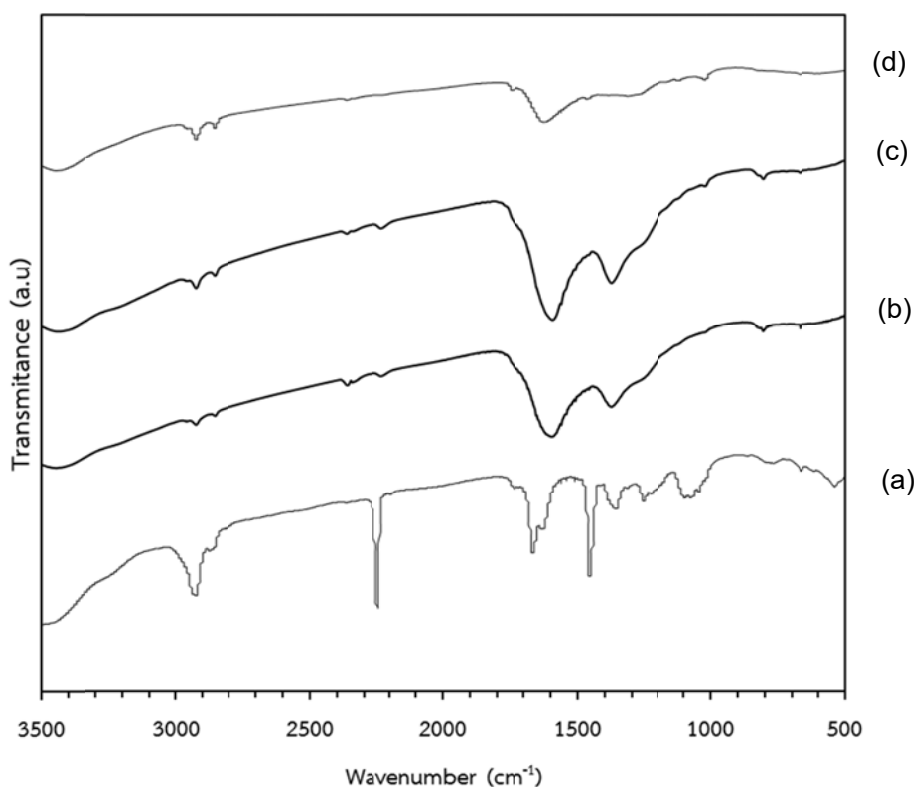


Figure 3.30 FT-IR spectra of PAN pristine fibers (a) as-spun fibers and after calcination (b) at 400°C, (c) 450°C and, (d) 500°C respectively.

### 3.3.3 Flexibility of PAN/ZnO core-sheath fibers

The fibers flexibility is recognized as one of the most important feature in this work. The carbon core from PAN sustained the flexibility of co-axial fibers after calcination at relatively high temperature in order to eliminate PVP and form the ZnO crystalline. The expectation of the final PAN/ZnO co-axial nanofibers should have the flexibility implied by the appearance of plastic region in stress-strain curve.

#### 3.3.3.1 Effect of calcination temperature on flexibility of fibers

The flexibility of the PAN/ZnO core/sheath nanofibers was investigated by universal testing machine. It can be seen from Figure 3.31 that mechanical behavior of the products after calcination at 450°C is somewhat similar to that of the as-spun fibers, i.e., consisting of two regions starting from linear elastic region and subsequent plastic region. The ductile behavior shown by the plastic region is the significant indicator for the flexibility of the fibers. Nevertheless, it should be noted that the yield strength of the calcined fibers is about 18% lower than that of the as-spun fibers due to the deterioration of PAN by heat. When the calcination temperature was raised to 500°C, however, the obtained fibers reveal the lack of the plastic region representing brittle behavior. So the suitable calcination temperature was below 500°C to keep the residual PAN carbon in the flexible form such as ladder structure.

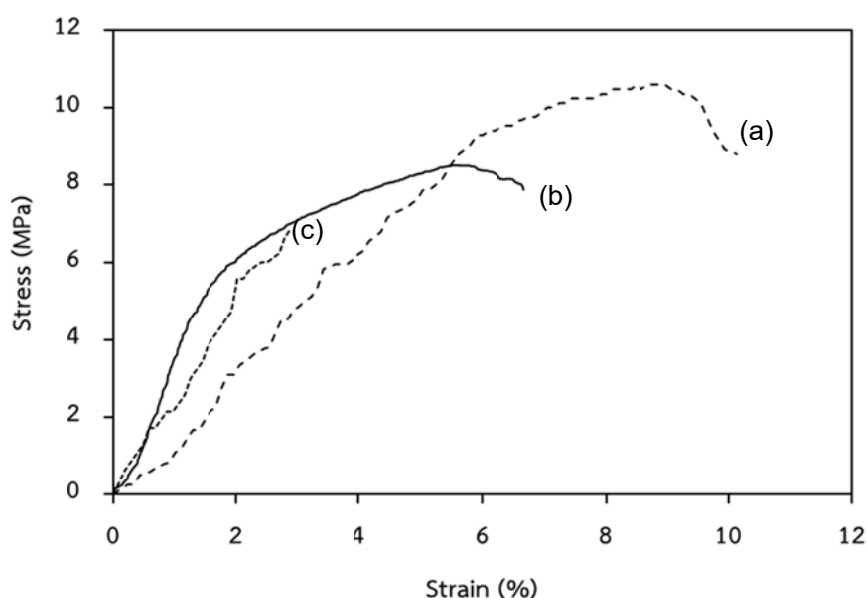


Figure 3.31 Stress-strain curves of co-axial fibers before calcination (a) and after it had been calcined at 450°C (b) and at 500°C (c).

### 3.3.3.2 Effect of polymer concentration on flexibility of fibers

In this work, the polymer concentrations, both PVP in sheath and PAN in core, were varied in order to achieve the co-axial structure and flexibility of the fibers. The PVP sheath concentration was varied five values i.e., 8, 10, 12, 15 and 18 % by weight. PAN core concentration was varied three values i.e., 8, 10, and 12 % by weight. After being calcination at 450°C, either residual PAN in the core or ZnO crystals including remainder PVP in the sheath, depending on the varied PVP sheath concentration, affects the flexibility of products. Figure 3.32 shows the stress-strain curves of the products. The dash line shows the behavior of pristine PAN at 8, 10, and 12%. From the stress-strain curves, it can obviously divide into two groups; one is below the stress of 10 MPa, the other is above this value. The conditions that stress higher than 10 MPa were 8%PVP-8%PAN, 8%PVP-10%PAN, 8%PVP-12%PAN, 10%PVP-8%PAN, and 10%PVP-12%PAN. It may be the effect between the viscosity of core and sheath. At relatively low viscosity of sheath i.e., 8% and 10%, the effect of core was stronger than sheath. So the performance of curves was near the behavior of the pristine PAN. Most of the co-axial fibers abide by the former group, which the stress is lower than 10 MPa (not shown in Figure). The behavior of stress-strain deviated from pristine PAN significantly.

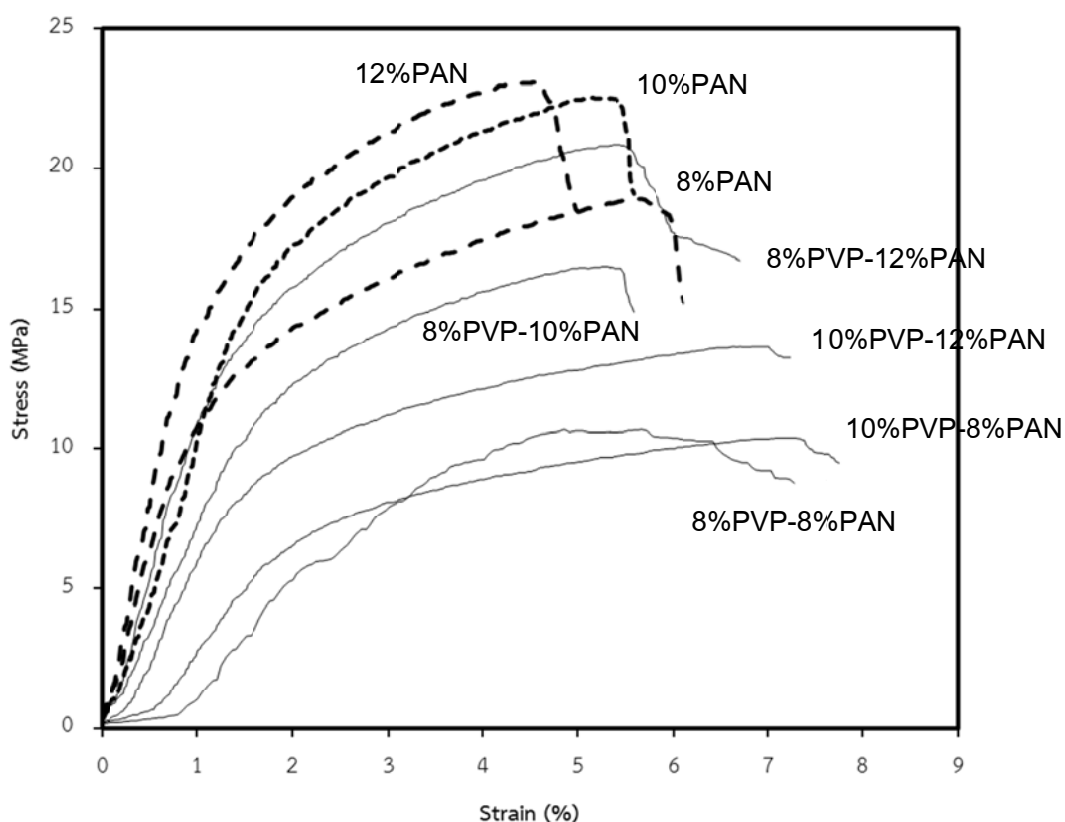


Figure 3.31 Stress-strain curves of co-axial fibers after it had been calcined at 450°C.

### 3.4 Photocatalytic degradation

#### 3.4.1 Photocatalytic activity of PAN/TiO<sub>2</sub> core-sheath fibers

As mentioned earlier, the photocatalytic activity of the synthesized products was preliminarily evaluated by the degradation of methylene blue (MB) solution. For the products with high activity, they will be further used for degradation of highly stable toxic compound, i.e., diuron [3-(3,4-dichlorophenyl)-1,1-dimethyl urea]. Unfortunately, the PAN/TiO<sub>2</sub> core-sheath fibers do not show significant photocatalytic activity toward the degradation of MB, as shown in Table 3.2.

Table 3.2 MB degradation percentage after 3-h reaction using various kinds of TiO<sub>2</sub> catalysts

Catalyst	% degradation
PAN/TiO <sub>2</sub> core-sheath fibers	1.79
TiO <sub>2</sub> fibers derived from sheath solution	33.55
Commercial P25 TiO <sub>2</sub> powder	53.22

It should be noted that all fibers were calcined at 500°C to ensure complete removal of PVP from sheath part of the fibers, although it was found from XRD characterization that the content of rutile in TiO<sub>2</sub> formed would increase. Despite the fact that anatase phase, which is the photoactive phase of TiO<sub>2</sub> is still present on the fibers, its photocatalytic activity was inhibited. The inhibiting effect should be the result of the structure of the core-sheath fiber itself, because the TiO<sub>2</sub> fibers that were derived from the same sheath solution and were subjected to the same calcination process showed much higher activity (although the activity was not as high as that of the commercial TiO<sub>2</sub> powder). Many attempts were tried to adjust the core-sheath structure so that the photocatalytic activity of the PAN/TiO<sub>2</sub> could be improved, but all attempt failed, as shown in the results in Table 3.3. It should be noted that the ranges of the parameters investigated were limited by the desired structure of the fibers to be core-sheath fibers.

Table 3.3 MB degradation percentage after 3-h reaction using PAN/TiO<sub>2</sub> core-sheath fibers derived from various recipe. DMF was used as the solvent for sheath solution.

Varied parameter	Condition	% degradation
PVP concentration	10 %wt.	1.11
	11.5 %wt.	2.35
	13 %wt.	0
TTIP concentration	11 %wt.	0
	15.5 %wt.	2.35
	20 %wt.	2.94
Aging time	0 min	0
	15 min	2.35
	30 min	0
Applied potential	22 kV	0
	24 kV	2.35
	26 kV	0

Since the calcination temperature used (i.e., 500°C) was high enough to remove all PVP from the sheath of the fibers, it was speculated that PAN in the core of the fibers might diffuse into the sheath part of the fibers and cover TiO<sub>2</sub> crystal, hence hindering the activity of the TiO<sub>2</sub>. To prevent the diffusion of PAN to the sheath, the solvent of the sheath was changed from DMF to ethanol. Ethanol could prevent PAN diffusion because PAN does not dissolve in ethanol. Then, various parameters were varied again to obtain the PAN/TiO<sub>2</sub> core-sheath nanofibers. Their photocatalytic activities are reported in Table 3.4. The results reject the hypothesis because insignificant improvement in the photocatalytic activity was achieved even after the prevention of PAN diffusion to the sheath of the fibers. Further investigation to reveal the reason for such low photocatalytic activity failed.



Table 3.4 MB degradation percentage after 3-h reaction using PAN/TiO<sub>2</sub> core-sheath fibers derived from various recipe. Ethanol was used as the solvent for sheath solution.

Varied parameter	Condition	% degradation
PVP concentration	10 %wt.	0
	11.5 %wt.	1.79
	13 %wt.	6.75
TTIP concentration	11 %wt.	0
	15.5 %wt.	1.79
	20 %wt.	0
Aging time	0 min	6.12
	15 min	1.79
	30 min	0
Applied potential	22 kV	0
	24 kV	1.79
	26 kV	0

Due to negligible photocatalytic activity of the PAN/TiO<sub>2</sub> core-sheath fibers, it was unethical to publish the results of the research in the fabrication part knowing that the PAN/TiO<sub>2</sub> products do not have photocatalytic activity.

#### 3.4.2 Photocatalytic activity of PAN/ZnO core-sheath fibers

The photocatalytic activity of PAN/ZnO core-sheath fibers was investigated in the same manner as that for PAN/TiO<sub>2</sub> core-sheath fibers. At first, the PAN/ZnO products that were calcined at 450°C were tested. Their activity was compared with the ZnO powder derived from the sheath solution and with the commercial ZnO powder. The results are shown in Figure. 3.32.

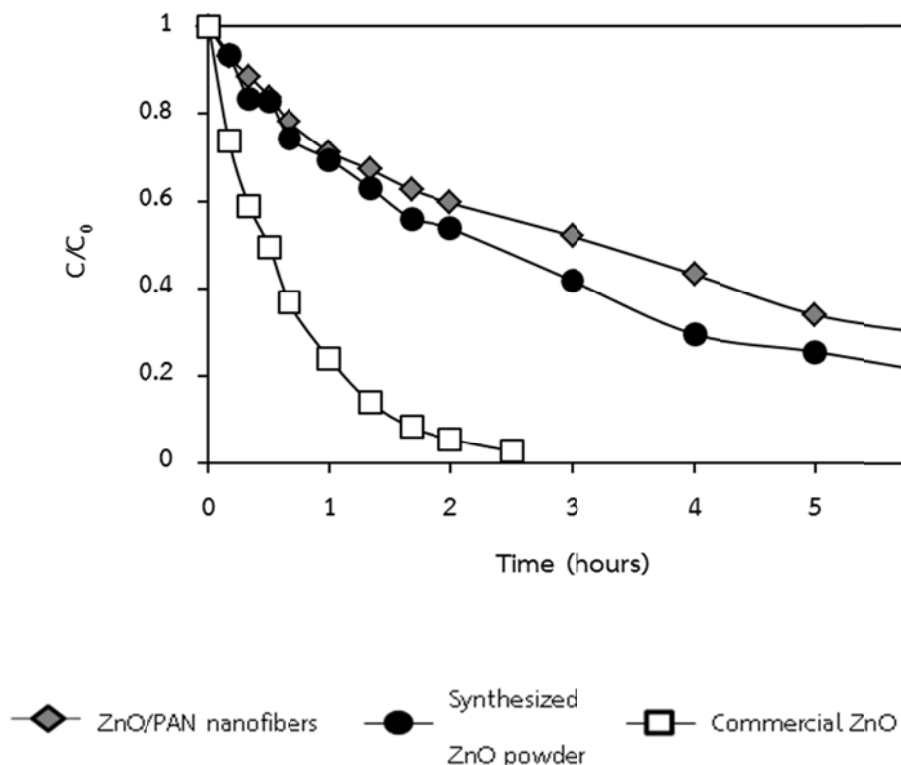


Figure 3.32 Photocatalytic degradation of MB using PAN/ZnO nanofibers, ZnO powder and commercial ZnO powder.

Although the activity of the synthesized ZnO is lower than that of the commercial ZnO, substantial activity was observed, unlike in the case of PAN/TiO<sub>2</sub>. The study of degradation kinetics revealed that the reaction follows the pseudo-first order kinetic model in similar manner as that on ZnO nanoparticles. The kinetic parameters obtained are shown in Table 3.5. It should also be noted that the activity of the core-sheath fibers is roughly the same as that of the ZnO powder derived from the sheath solution. The slight decrease in the activity of the PAN/ZnO fibers may be the result from the loss of the surface area of ZnO crystals, which adhere to the PAN core. Several attempts were done to improve their activity.

Table 3.5 Pseudo-first order kinetic parameter for MB degradation using various kinds of ZnO catalysts.

Catalyst	k (h <sup>-1</sup> )	R <sup>2</sup>
PAN/ZnO core-sheath fibers	0.218	0.960
ZnO powder derived from sheath solution	0.283	0.976
Commercial ZnO powder	1.462	0.999

#### 3.4.2.1 Effect of calcination temperature

The effect of calcination temperature on the photocatalytic activity is an important parameter to be studied. Calcination at higher temperature induces growth of crystallite and also eliminates some contaminants which often decrease photocatalytic activity.

The MB degradation activity of the PAN/ZnO products calcined at various temperatures is shown in Figure 3.33. It should be noted that the calcination temperature lower than 300°C is not high enough to convert amorphous ZnO to crystalline ZnO. The rate constant for the catalyst calcined at 400, 450, and 500°C is 0.122, 0.218, and 0.508 h<sup>-1</sup>, respectively.

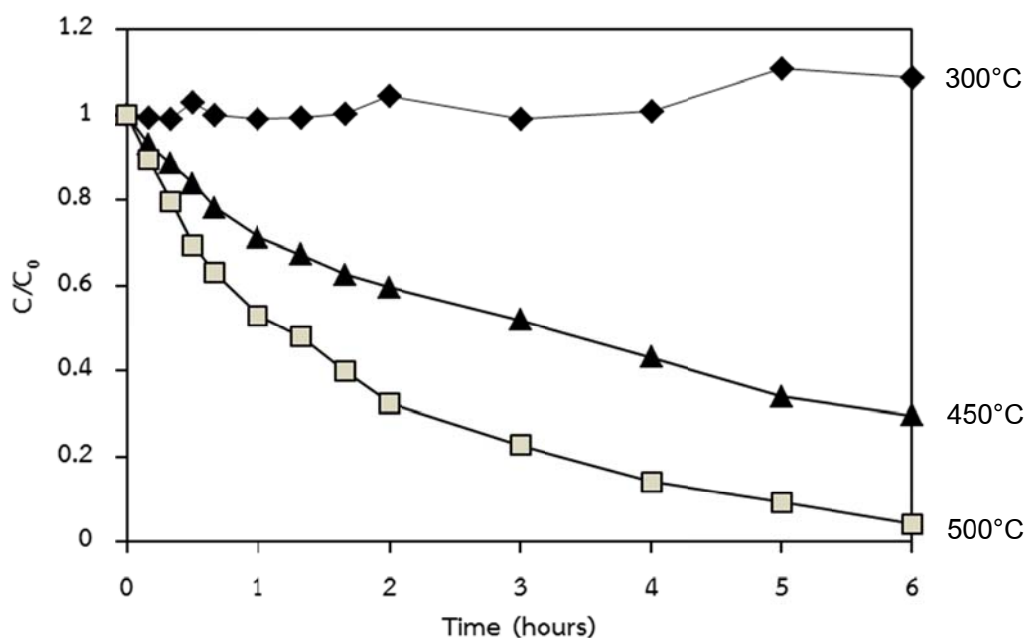


Figure 3.33 Photocatalytic degradation of MB using PAN/ZnO nanofibers calcined at various temperatures.

The crystalline phase of ZnO is an important factor influencing its photocatalytic activity. According to XRD results, the ZnO crystals in wurtzite phase, which is the photactive phase, are detected in the co-axial products after being calcined at temperature higher than 400°C. However, the crystallite size is increase with the increase in calcination temperature. The crystallite size of the ZnO phase calculated by the Debye-Scherrer was found to be 13.1 and 20.8 nm for calcination at 400 and 450°C, respectively. Nevertheless, regarding the effect of the calcination temperature for ZnO, which naturally has low surface area, the loss in surface area by the growth in crystal size is outweighed by the increase in crystallinity. Hence, high calcination temperature is preferred, but it is limited by the thermal decomposition of PAN core.

#### 3.4.2.2 Effect of aging time

ZnO in the sheath was prepared by sol-gel method. The effect of sol aging time was investigated. In this study, it was serendipitously found that sol aging time of 7 days could be fabricated into the co-axial fibers and yielded the high photocatalytic activity rather than the one that was not aged. Figure 3.34, shows the degradation of MB using PAN/ZnO products that were aged for different aging time, i.e., no aging, 4, and 7 days.

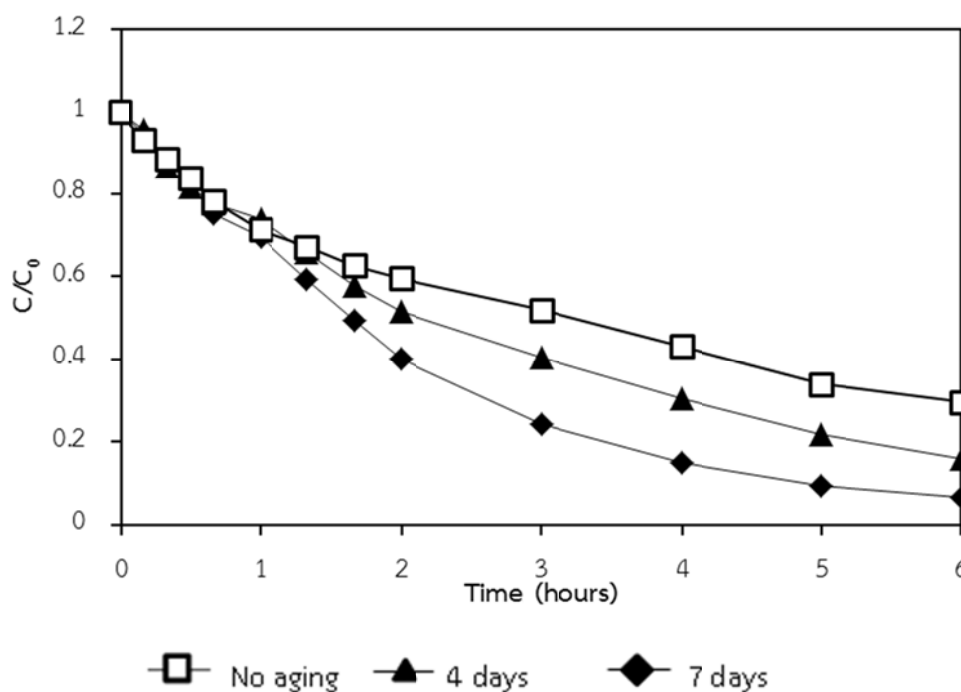


Figure 3.34 Effect of ZnO aging time on MB degradation.

The prolonged aging time results in higher crystallinity of the ZnO particles in the PAN/ZnO core-sheath fibers, as shown by the XRD analysis in Figure 3.35.

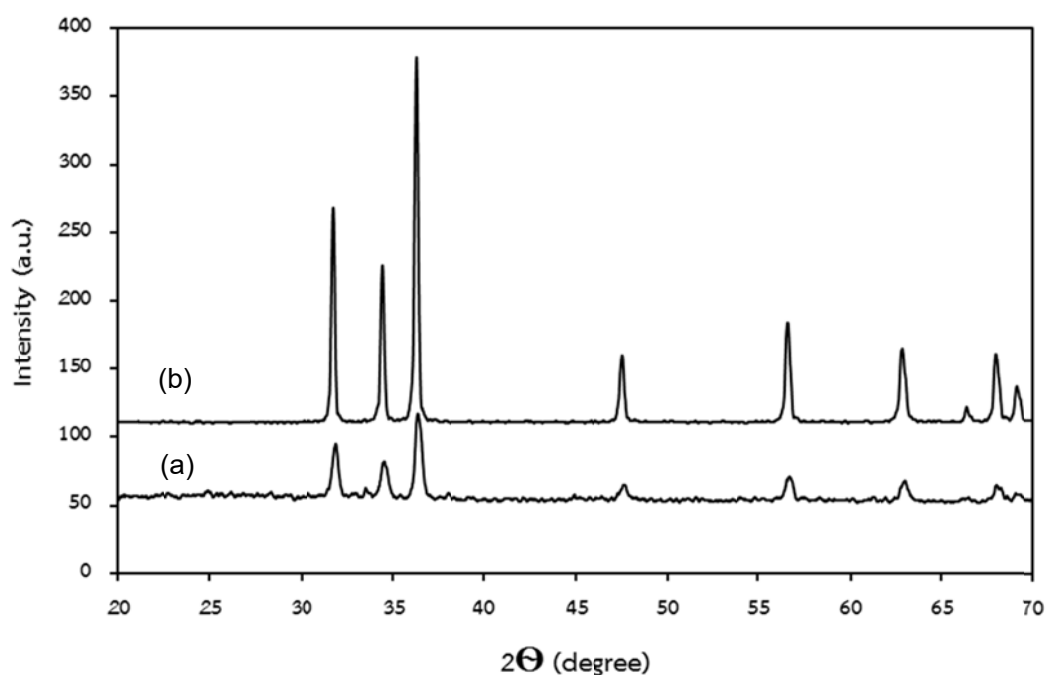


Figure 3.35 XRD patterns of the ZnO/PAN co-axial fibers calcination at 450°C for aging time of (a) no aging, (b) 7 days.

Despite the investigation of various factors, the attempt to increase the photocatalytic activity of the PAN/ZnO core-sheath fibers to be in the same order as the commercial ZnO powder failed. The rate constants from the PAN/ZnO fibers are still one order of magnitude smaller than that of the regular ZnO particles. Again, it was unethical to withhold the fact in the publication that the product is far worse than the commercially available catalyst. Hence, although novel form of the product could be fabricated, the results could not be published.

### 3.4.3 Photocatalytic degradation of diuron on TiO<sub>2</sub> and ZnO particles

#### 3.4.3.1 Degradation kinetics

At the same time, while the PAN/TiO<sub>2</sub> and PAN/ZnO fibers were tested for their photocatalytic activity, the TiO<sub>2</sub> and ZnO particles derived from the sheath solutions were tested for their activities as well. Not only that there were tested for MB degradation (as shown in the previous sections), but they were also tested for diuron degradation. The physical properties of the TiO<sub>2</sub> and ZnO particles are shown in Table 3.6.

Table 3.6 Properties of TiO<sub>2</sub> and ZnO particles derived from sheath solutions. Both compounds were calcined at 500°C for 2 h.

Properties	TiO <sub>2</sub>	ZnO
Phase	Anatase & rutile	Wurtzite
Crystallite size (nm)	14	104
Specific surface area (m <sup>2</sup> /g)	36	4
Type of N <sub>2</sub> adsorption isotherm	Type IV	Type III
Band gap (eV)	3.1	3.1

Conventionally, it has been reported that the photocatalytic system produces hydroxyl radical during the reaction. The radical is a strong oxidizing agent that reacts with diuron and causes degradation toward its mineralization. In this work, the photodegradation of diuron aqueous solution was conducted in a pyrex reactor. The content of the photocatalyst was kept at 1 mg of the catalyst per 10 ml of the solution (initial diuron concentration of 10 ppm). The photodegradation of diuron solution using zinc oxide or titania as a catalyst was achieved within 6 hours of UV irradiation. The experiments under UV-light without catalyst, confirmed the absence of photolysis of diuron. It can be inferred that there is no appreciable degradation when the aqueous solution is irradiated in the absence of titania or zinc oxide. The degradation of diuron is less than 5% after 6 hours of irradiation without the catalyst, which is similar to the result reported for self-degradation in the dark at room temperature indicating that hydrolysis of diuron can be neglected [43].

Figure 3.36 shows the disappearance of diuron by photocatalytic degradation using titania and zinc oxide. Both zinc oxide and titania have been known to be capable of producing of radicals upon the exposure with UV light. It should be noted that high surface area of titania

is expected to facilitate greater amount of diuron adsorbed on the surface, leading to higher rate of degradation, because the band gap energy of both catalysts are the same. However, comparison of the catalytic activities of zinc oxide and titania, in regard of the decrease in both diuron concentration and the total organic carbon in the solution, clearly indicates the difference in the degradation efficiency. It was found that the synthesized zinc oxide has higher performance in degrading and mineralization of diuron than titania, regardless of much lower surface area. This observation implies that the degradation via oxidation of hydroxyl radicals generated from the photocatalyst is much more complicated than expected. The catalyst itself should play a role in degradation rather than being a source of the hydroxyl radicals. Detailed study is needed.

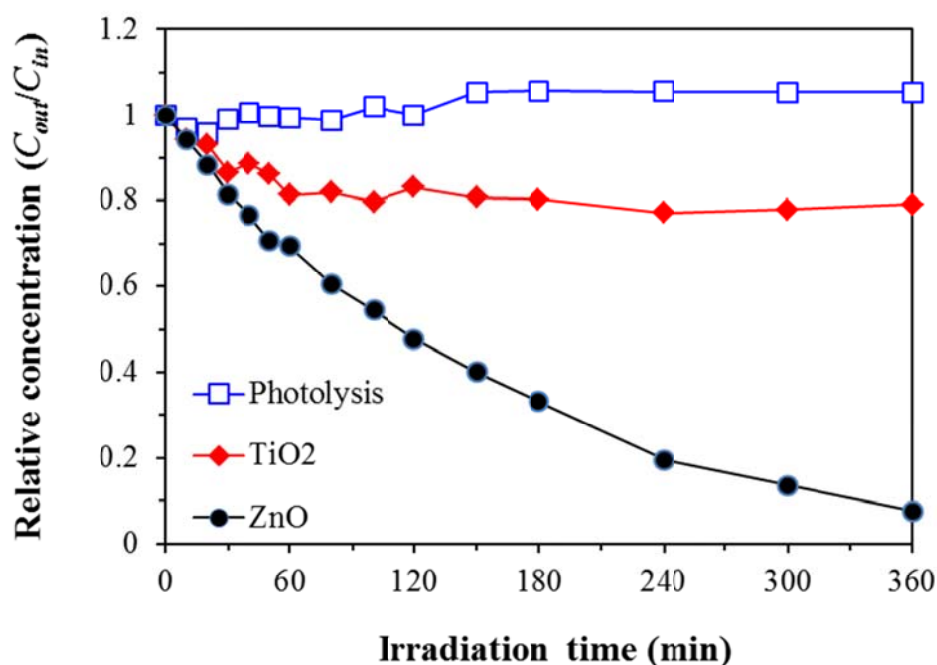


Figure 3.36 Concentration of diuron with respect to initial diuron concentration during photocatalytic degradation on TiO<sub>2</sub> and on ZnO.

Regardless of the difference in the rate of degradation on different catalyst, the degradation on both catalysts still follows the pseudo-first order kinetic model. The fitted kinetic parameters are shown in Table 3.7. It should be noted that the  $R^2$  for the fitting for the degradation of titania is significantly lower than that on zinc oxide. Hence, the mechanisms for the degradation on both catalysts are suggested to be different.

Table 3.7 Comparison of the pseudo-first order kinetic parameter for diuron degradation on TiO<sub>2</sub> and on ZnO particles derived from sheath solutions.

Catalyst	k (min <sup>-1</sup> )	R <sup>2</sup>
TiO <sub>2</sub> powder	0.0010	0.7783
ZnO powder	0.0067	0.9935

### 3.4.3.2 Degradation intermediates

During the photocatalytic reaction, radicals formed from the photocatalysts react with diuron to generate the intermediates. Structure of functional groups attaching to aromatic ring of diuron is mainly responsible for the structure of the intermediates formed. Diuron clearly offers two sites for the reaction, i.e. the aromatic ring and the aliphatic side chain.

In the preliminary investigation of the intermediates formed during the degradation, samples collected at different irradiation time were freeze-dried for the purpose of concentrating the intermediates. These powders were re-suspended in a solution consisting of 70% acetonitrile and 30% water and injected into LC/MS. Table 3.8 shows comparison of intermediates appeared in LC/MS spectrum for the degradation of diuron on titania and zinc oxide, which includes the structure of each unknown intermediates evaluated. Products were identified based on the molecular ion and mass spectrometric fragmentation peak.

Table 3.8 Possible intermediates generated from photodegradation of diuron on TiO<sub>2</sub> and ZnO.

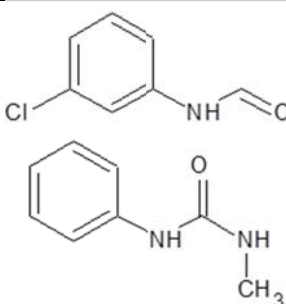
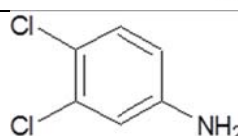
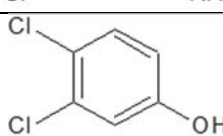
Compound	Possible structure(s)	TiO <sub>2</sub>	ZnO
1		Yes	Yes
2		Yes	Yes
3		Yes	Yes



Table 3.8 (continued)

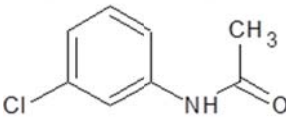
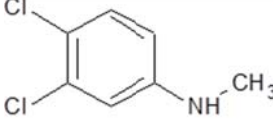
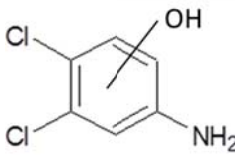
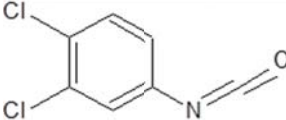
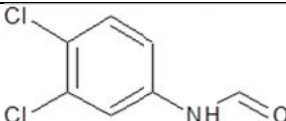
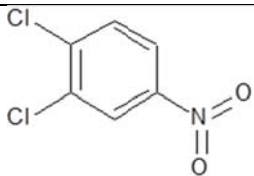
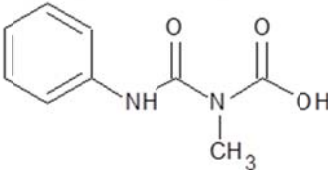
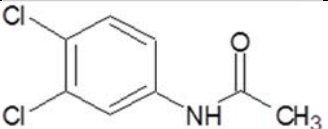
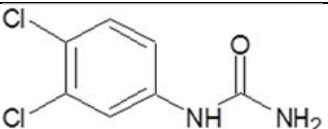
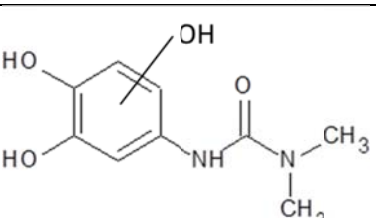
Compound	Possible structure(s)	TiO <sub>2</sub>	ZnO
4		No	Yes
5		Yes	No
6		Yes	No
7		Yes	No
8		Yes	No
9		No	Yes
10		Yes	No
11		Yes	Yes
12		Yes	Yes
13		Yes	No

Table 3.8 (continued)

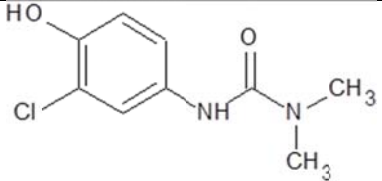
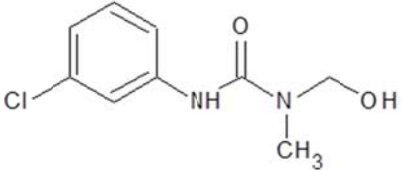
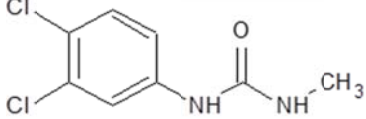
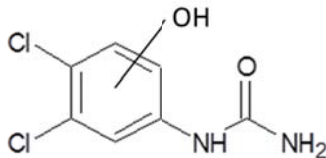
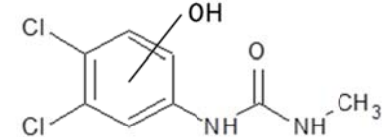
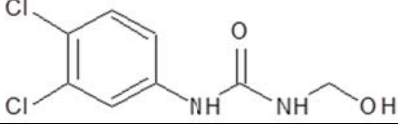
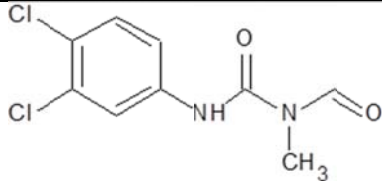
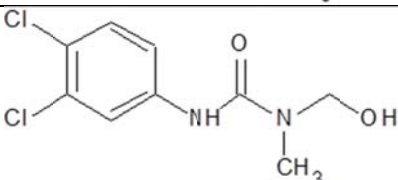
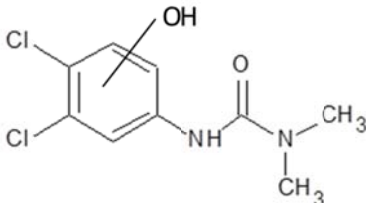
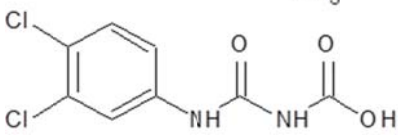
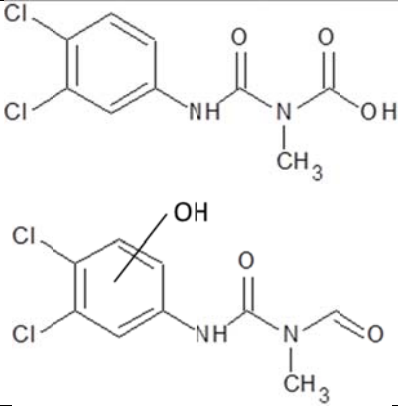
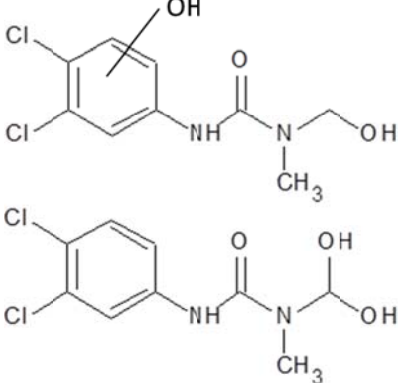
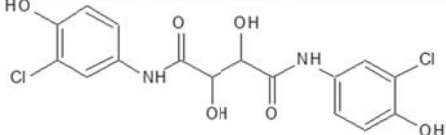
Compound	Possible structure(s)	TiO <sub>2</sub>	ZnO
14	 	Yes	Yes
15		Yes	Yes
16		Yes	Yes
17	 	No	Yes
18		Yes	Yes
19	  	Yes	Yes

Table 3.8 (continued)

Compound	Possible structure(s)	TiO <sub>2</sub>	ZnO
20		No	Yes
21		No	Yes
22		No	Yes

Comparison of the intermediates formed from the reaction using different photocatalysts, i.e., titanium dioxide and zinc oxide, reveals common intermediates as well as different intermediates. As many of the intermediates listed in the Table 3.8 are common with those reported in other researches, it confirms that the main degradation pathway of diuron using zinc oxide and titanium dioxide follows the mechanisms previously proposed. They included hydroxylation of the aromatic ring and of the side chain, dehalogenation or dechlorination of the aromatic ring, demethylation, and condensation. However, it was postulated that different type of catalyst has different surface properties, which affect the interaction between diuron and the catalyst surface. The dissimilarity in the degradation mechanism arises from the difference in interaction between the catalyst surface and the adsorbed diuron. Nevertheless, it was difficult to compare different surfaces from different catalysts. Hence, further investigation was

conducted using the same catalyst that was synthesized in different manner to result in different exposing surfaces.

#### 3.4.4 Photocatalytic degradation of diuron on different surfaces of ZnO

According to the hypothesis stated in the previous section, zinc oxide was chosen as the catalyst for further investigation because it can be synthesized with control of the dominating surface on the particles. A hexagonal crystal of wurtzite ZnO consists of two main sets of surfaces: (i) zinc-terminated (0001) and oxygen-terminated ( $\bar{0}00\bar{1}$ ) polar surfaces located at the top and bottom planes of the crystal, and (ii) mixed-terminated (10-10) nonpolar surfaces as the side planes. Herein, the adsorption and photocatalytic degradation of diuron on two different types of ZnO particles, i.e., conventional hexagonal ZnO particles with polar surfaces as the dominating planes, and ZnO nanorods with the mixed-terminated surfaces, were systematically studied.

##### 3.4.4.1 Synthesis of ZnO with different morphologies

Conventional ZnO powder was synthesized via the sol-gel technique. The procedure was an adaptation from the previous report [11]. A mixture containing ethanol, diethanolamine, hydrochloric acid, and deionized water in amounts of 5, 1.58, 0.18, and 0.25 mL, respectively, was slowly dropped into a solution of zinc acetate (3.29 g) in 20 mL of deionized water. The mixture was stirred for 2 h and was aged without stirring for 24 h. After being dried at 80°C overnight, the mixture transformed into a gel. The gel was aged further for 3 days before being calcined at 500°C for 2 h to obtain ZnO powder.

In contrast, ZnO nanorods were synthesized via the hydrothermal method modified from that the previous report [44]. A precursor solution was prepared from 1.1 g of zinc acetate in 4 mL of deionized water and 6 mL of 8 M sodium hydroxide aqueous solution. Then, 2 mL of the precursor solution was mixed with 5 mL of polyethylene glycol and 20 mL of ethanol. The mixture was heated at 140°C for 1 h under autogenous pressure in a Teflon-lined autoclave. The precipitate was washed with ethanol and deionized water before being dried at 60°C overnight.

Micrographs shown in Figure 3.37 indicate that ZnO synthesized by both techniques are significantly different in particle size and morphology. The product from the sol-gel technique is micron-sized particles with low aspect ratio. The hexagonal plane, which is either (0001) or

(000-1) plane, can be obviously seen in Figure 3.37a. On the other hand, the product from the hydrothermal process (Figure 3.37b) is high-aspect ratio hexagonal nanorods with average length in the range of 200-400 nm. The results from selected area electron diffraction (shown as insets in Figure 3.37) and X-ray diffraction analysis (Figure 3.38) suggest that both catalysts are single crystals of ZnO in wurtzite phase. Therefore, comparing between these catalysts, the nanorods expose more mixed-terminated (10-10) nonpolar surface and less polar surfaces (i.e., (0001) and (000-1)) than the conventional particles. This is consistent with the difference in zeta-potential, i.e., -14 mV for the nanorods versus -30 mV for the conventional particles, measured in deionized water, using Zetasizer (Nanoseries S4700). The optical band gaps of these catalysts, measured using Tauc plot, are about the same at 3.1 eV. Lastly, the specific surface area of the conventional particles and the nanorods measured by nitrogen adsorption via Brunauer-Emmett-Teller is 1.4 and 17 m<sup>2</sup>/g, respectively. The nitrogen adsorption isotherms of both catalysts (Figure 3.39) are Type III, which indicates that they are non-porous.

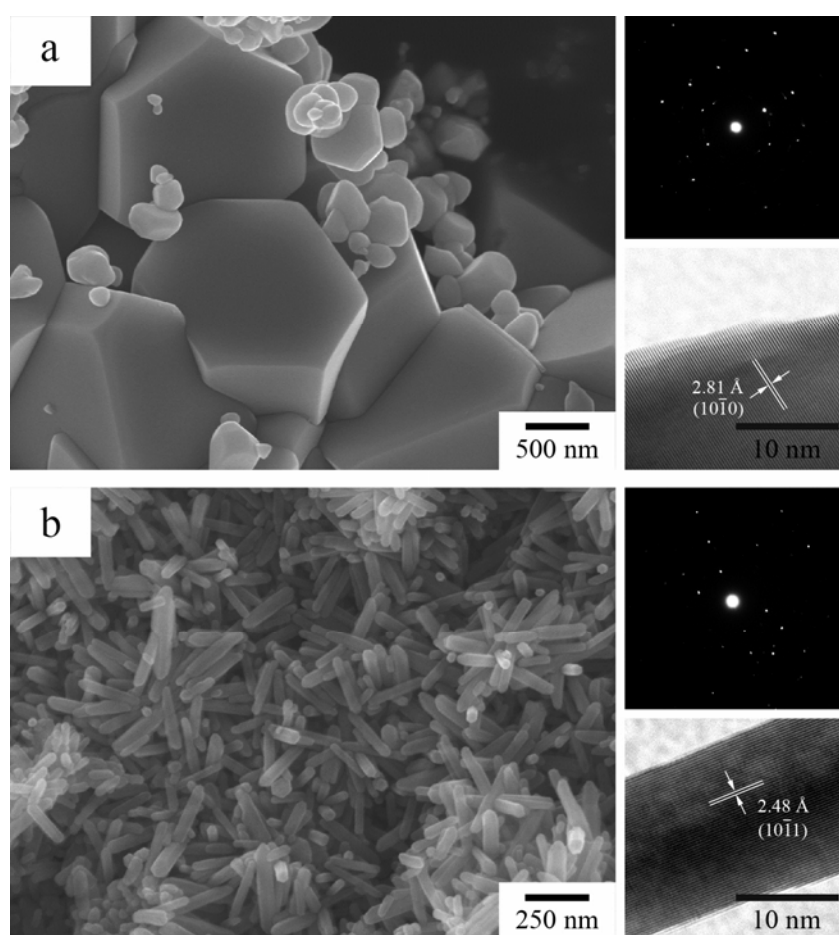


Figure 3.37 SEM micrograph, HR-TEM micrograph and SAED pattern of ZnO synthesized by (a) sol-gel and (b) hydrothermal techniques.

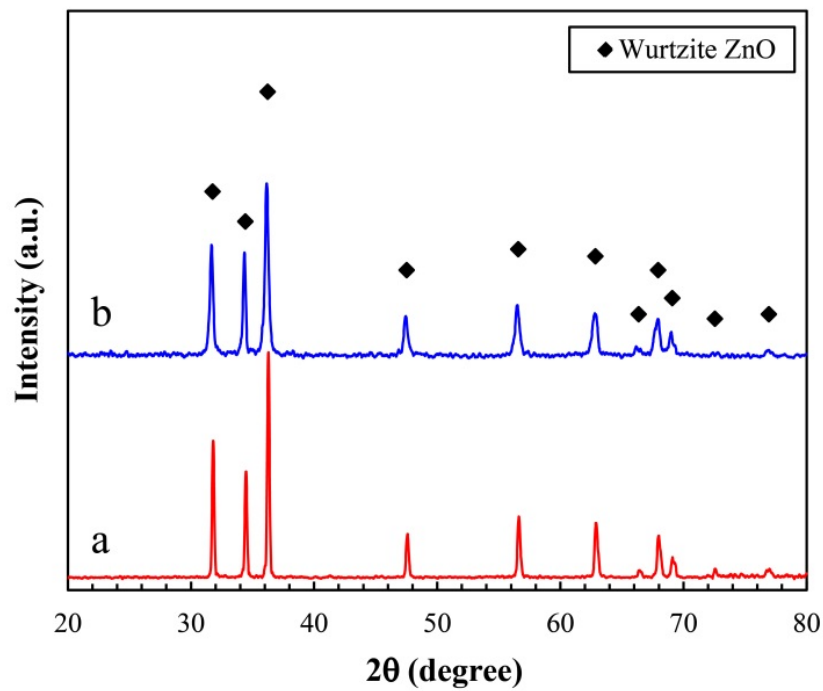


Figure 3.38 X-ray diffraction patterns of (a) conventional ZnO particles synthesized by the sol-gel technique and (b) ZnO nanorods synthesized by the hydrothermal method.

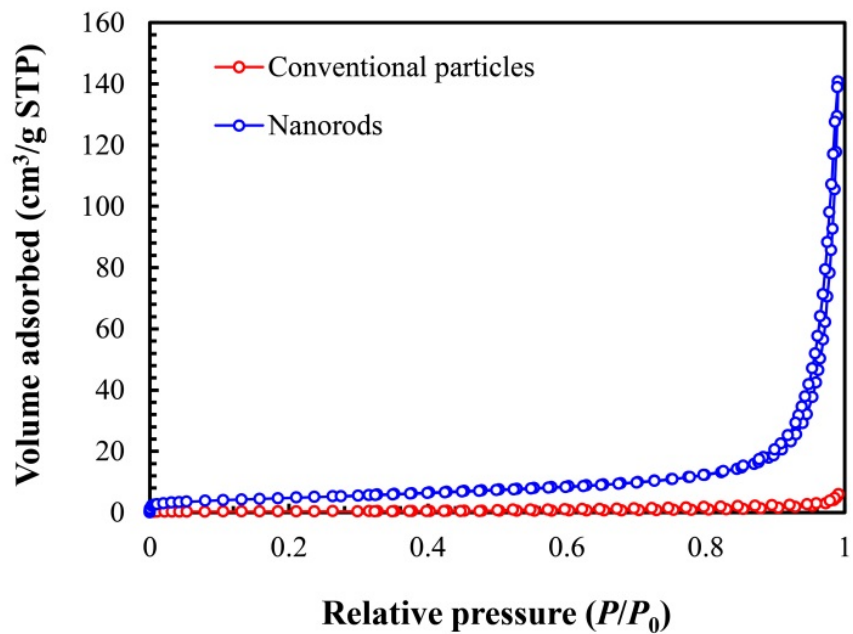


Figure 3.39 Nitrogen adsorption/desorption isotherms of conventional ZnO particles and ZnO nanorods.

#### 3.4.4.2 Adsorption of diuron on ZnO with different morphologies

Adsorption experiments were performed by immersing the catalyst into the diuron solution with predetermined concentration, of which the temperature was controlled to be  $25 \pm 2^\circ\text{C}$ . The catalyst content was 10 mg/10 mL of the solution. The system was kept in the dark. After 6 h, which was experimentally determined to be sufficient to reach adsorption equilibrium, the concentration of the solution was determined by reverse-phase high-performance liquid chromatography (HPLC)

Experimental data for the adsorption of diuron on both types of ZnO catalyst are shown in Figure 3.40. The Freundlich model, which has previously been shown valid for the adsorption of some organic compounds on solid surfaces, was found to represent the adsorption data well, while the Langmuir adsorption model failed to fit the experimental data. The fitted Freundlich parameters are presented in Table 3.9. The value of the Freundlich parameter relating to adsorption intensity ( $1/n$ ) show that diuron adsorbs on both catalysts by physical adsorption [45]. The adsorption intensities show unambiguously that diuron adsorbs more strongly on the conventional ZnO particles than on the ZnO nanorods.

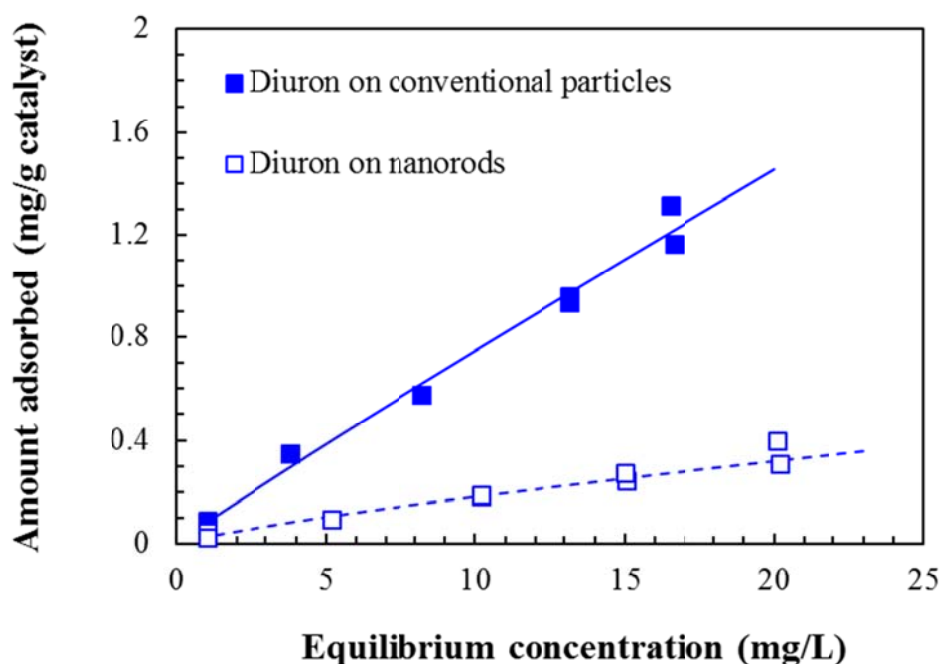


Figure 3.40 Adsorption isotherms of diuron on conventional ZnO particles and on ZnO nanorods. The lines represent fitted Freundlich adsorption isotherms.

Table 3.9 Fitted parameters for Freundlich adsorption model for diuron adsorption on ZnO particles and ZnO nanorods.

Parameter	Conventional ZnO	ZnO nanorods
$K_f [L^{1/n} mg^{(1-1/n)}/g_{ZnO}]$	0.082	0.028
$1/n$	0.959	0.815
$R^2$ for parameter fitting	0.992	0.963
$R^2$ for model fitting	0.986	0.947

Figure 3.40 clearly illustrates that greater amounts of diuron was adsorbed on the conventional ZnO particles than on the ZnO nanorods, even though the surface area of the former is one order of magnitude lower than the latter, which might be expected to produce the opposite result. The fitted parameter relating to adsorption capacity ( $K_f$ ) for adsorption on the conventional ZnO particles is about twice the value for the nanorods.

To further understand the adsorption of diuron onto various surfaces of ZnO, molecular calculations were performed using density functional theory in the Dmol3 program in the Materials Studio 6.0 package. Each simulation modeled one molecule of diuron on 1 layer of a (6 unit cell  $\times$  6 unit cell) ZnO surface. The generalized gradient approximation (GGA) with the Perdew-Wang 1991 (PW91) function was used. A set of polarization functions (DNP) was set up as the basis set with the cutoff radius of 4.4 Å. The electron basis set was used for all elements except Zn, which was treated by an effective core potential. The maximum energy change, the maximum force, and the maximum displacement were set at  $1 \times 10^{-5}$  hartree,  $2 \times 10^{-3}$  hartree/Å, and  $5 \times 10^{-3}$  Å, respectively. The effect of water as solvent was incorporated in the simulation via conductor-like screening model (COSMO). The adsorption energy on the surface was calculated as the difference between the energies of the system before and after adsorption.

For each surface, several initial positions and orientations of the adsorbate molecule were tested to obtain the most stable adsorption configuration. The associated adsorption energy for each case is shown in Table 3.10, while the optimized molecular configurations for the adsorption of diuron on the surfaces are shown in Figures 3.41. The calculated energies support the experimental finding that adsorption on the mixed-terminated nonpolar surface of ZnO is less favorable than that on polar surfaces.



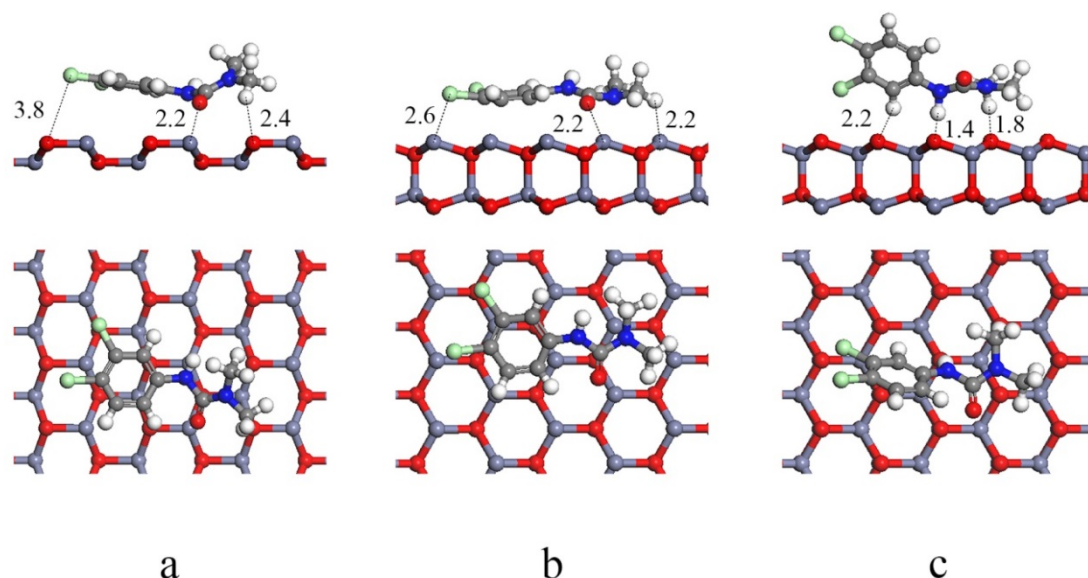


Figure 3.41 The optimized models for adsorption of diuron on: (a) mixed-terminated (10-10) surface, (b) zinc-terminated (0001) surface, and (c) oxygen-terminated (000-1) surface, where the distances between adsorbed diuron and ZnO-surface atoms are given in Å.

Table 3.10 Calculated adsorption energy for adsorption of diuron on each surface of ZnO.

Surface	Adsorption energy (kcal/mol)
Mixed-terminated	-31.89
Zinc-terminated	-38.17
Oxygen-terminated	-42.86

According to the adsorption configurations in Figure 3.41, the observation that negatively charged part of the molecule, such as methoxy oxygen of diuron, approaches positively charged atom on the surface (i.e., zinc atom), while chlorine atoms are repelled by negatively charged surface atom (i.e., oxygen atom) suggested that the interactions between diuron and the surfaces of ZnO are electrostatic. For diuron, electrons in the aliphatic part of the molecule are localized at the oxygen and nitrogen atoms. The aromatic part is relatively electron-rich, i.e., with electron density delocalized in the ring and localized around chlorine atoms.

According to the simulation of adsorption on the mixed-terminated surface of ZnO (Figure 3.41a), diuron adopts a bent conformation so that the most negatively charged part of the molecule, i.e., the amide oxygen and nitrogen attached to the aromatic ring, can approach

positively charged zinc atoms on the surface at distances of 2.2 and 2.6 Å, respectively. At the same time, the hydrogen atoms in both methyl groups are attracted by the oxygen atoms of ZnO at distances of 2.4 Å. This C—H···O interaction is considered as a weak hydrogen bond [46]. Being restricted by the size of the molecule, the two chlorine atoms on the aromatic end of diuron are located near oxygen atoms on the surface and thereby are repelled from the surface.

On the zinc-terminated surface (Figure 3.41b), diuron adsorbs in planar configuration, i.e., the aromatic ring is parallel to the surface. Because the surface is uniformly composed of positively charged zinc atoms, both ends of diuron molecule, which are electron-rich, are attracted to the surface simultaneously. However, the aliphatic chain of diuron is twisted such that the methoxy oxygen tilts toward the surface while both methyl groups are repelled away from the surface. The distance between the oxygen atom in diuron and the closest zinc atom on the surface is 2.2 Å, which is approximately the same as the corresponding distance for adsorption on the mixed-terminated surface. The energy of adsorption on the zinc-terminated surface is significantly higher than that on the mixed-terminated surface (by c.a. 6.3.6 kcal/mol), which is consistent with reports that polar surfaces have higher surface energy than nonpolar surfaces [47].

On the oxygen-terminated surface, diuron tilts almost perpendicularly so that the electron-rich amide oxygen moves away from the negatively charged oxygen on the surface, while positively charged hydrogen atoms turn toward the surface. The repulsion between the surface and the delocalized electrons in the aromatic ring is also minimized. Tilting allows hydrogen atoms in the methyl group and the aromatic ring to form C—H···O interactions with the surface, which are stronger than the conventional attraction between opposite charges [46]. Hence, the adsorption energy on the oxygen-terminated surface (-42.86 kcal/mol) is much more negative (i.e., more favorable) than that on the zinc-terminated surface (-38.17 kcal/mol).

If the atom on the surface that is closest to the adsorbate molecule is defined as the adsorption site, Figures 3.41 shows that, on the mixed-terminated surface, zinc is the adsorption site for diuron. In the other words, only half of the surface atoms of the mixed-terminated surface are sites for stable adsorption. On the other hand, for the polar surfaces, all atoms can serve as adsorption sites. Furthermore, the adsorbate molecules that are already adsorbed on the surface will exert steric effects hindering adsorption on nearby sites. This steric effect will more severely reduce the adsorption capacity on the mixed-terminated surface, where not all atoms are potential adsorption sites. These factors contribute to the result that the adsorption capacity on the conventional ZnO particles is much higher than that on the

nanorods. Last, the simulation results confirm the experimental finding that the adsorption of diuron on any surface of ZnO is still physical in nature because the distances between the adsorbate molecules and the adsorption sites are too long to be considered as chemical bonds [48].

#### 3.4.4.3 Photocatalytic degradation kinetics

In this part, since it is desired to verify the actual intermediates formed during the degradation so that the degradation pathway could be correctly identified, the photocatalytic degradation was studied in a microreactor because the residence time within the reactor could be easily controlled. The microreactor was fabricated in a plate-like manner. A piece of glass that had been coated by 6.8 mg of the catalyst via spin-coating was assembled with another piece of glass into which inlet and outlet streams had been drilled. A Teflon sheet with a 0.8 cm × 4.8 cm opening was placed between the pieces of glass, forming a channel. The height of the channel was determined by the thickness of the Teflon sheet (250 μm). The microreactor assembly was then mounted in a stainless-steel housing.

A 10 ppm aqueous solution of diuron was constantly supplied into the microreactor via a syringe pump for 1 h prior to the irradiation to ensure complete adsorption of the compound undergoing degradation onto the catalyst. Then, the reactor was irradiated with light from a 40-W mercury lamp (Philips F40T12/BL), with an emission spectrum in the wavelength range of 350-410 nm, to initiate the reaction. The power flux at the location of the reactor was found to be  $3.18 \times 10^{-6} \text{ W/cm}^2$ , measured by an ILT1700 Research Radiometer (International Light Technologies) with SED005 GaAsP UV detector. The flowrate was controlled to correspond to the desired residence time in the range of 1-15 min. The concentration of the compound undergoing degradation was monitored at the outlet by HPLC. After reaching a steady state, a sample was collected for identification of the intermediates via liquid chromatography equipped with tandem mass spectroscopy (LC-MS/MS, Thermo Finnigan, LCQ Advantage). The experiments were repeated three times. It should be noted that, according to a preliminary test using inductively coupled plasma optical emission spectroscopy (ICP-OES, PerkinElmer Optima7000DV), less than 0.5% of the catalyst detached from the reactor throughout the whole period of the experiment.

The photocatalytic oxidation of an organic compound adsorbed on a catalyst can in principle take place either via direct oxidation by photogenerated holes or indirect oxidation by generated radicals (e.g., hydroxyl radicals). It has been generally known that photogenerated

holes ( $h^+$ ) play an important role in degradation of organic compounds [49]. However, the holes are likely to react with plentiful surrounding water molecules to form hydroxyl radicals. More importantly, it has been reported that chemisorption is a prerequisite for direct oxidation while physisorption is favorable for indirect oxidation [50]. Because it was shown in the previous section, via both the experimental and calculated results, that diuron attaches to conventional ZnO particles and ZnO nanorods via physical adsorption, it is suggested that the photocatalytic degradation in this work occurs via indirect oxidation. Since photocatalyst is stimulated under UV light, photogenerated electrons will enter excited state and leave positive holes on valence band. These holes then transfer to the surface of catalyst and react with water to produce hydroxyl radicals. Hydroxyl radicals are strong oxidizing agent which have high capability to attack pollutant molecule causing  $CO_2$  and  $H_2O$  as the terminal products [49]. Although the radicals can in principle diffuse into the bulk liquid and react with the pollutant there, this homogeneous reaction is considered negligible compared with oxidation on the surface [6].

The results for the photocatalytic degradation of diuron using the two different ZnO catalysts are shown in Figure 3.42. After 15 minutes of residence time, concentration of diuron in the solution was decreased from 10 ppm to 1.85 and 1.75 ppm when the conventional ZnO particles and ZnO nanorods was used as the catalyst, respectively. The experimental data obtained at several residence times are used to fit the steady-state mathematical model of the degradation. In similar manner as MB degradation, the degradation rate of diuron on zinc oxide can be described by a pseudo-first order kinetics. The fitted models are shown as lines in Figure 3.42 and the fitted parameters are shown in Table 3.11. The reaction rate constants obtained are in the same range as reported in literature [51], although the intensity of the light used in this work is approximately three orders of magnitude lower. This is one of the advantages of a microreactor.

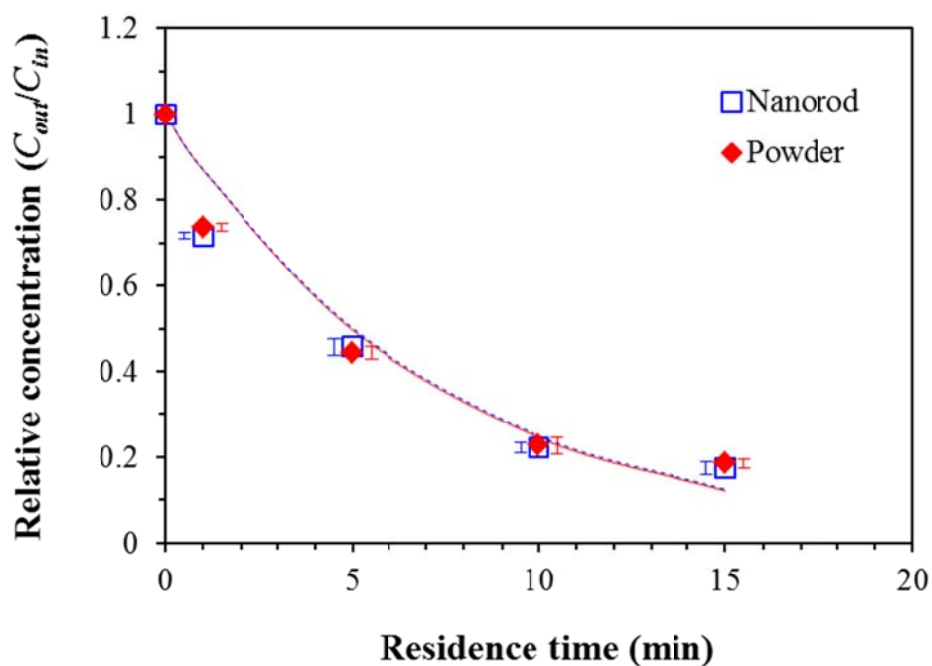


Figure 3.42 Photocatalytic degradation of diuron using conventional ZnO particles (diamonds) and ZnO nanorods (squares). The marks show experimental data, while the lines represent values calculated by the pseudo-first order kinetic model. The error bars are intentionally shifted for clarity of the plot.

Table 3.11 Fitted kinetic parameters for photocatalytic degradation of diuron on ZnO with different morphologies

Catalyst	k (min <sup>-1</sup> )	R <sup>2</sup>
ZnO powder	0.141	0.949
ZnO nanorods	0.139	0.940

The diuron degradation kinetics are not significantly different between the two catalysts, even though the experimental adsorption results showed that the adsorption capacity of diuron on the conventional particles was about 4 times larger than that on the nanorods. Because the surface area of the nanorods is one order of magnitude larger than that of the conventional particles, diuron molecules on the surface of the nanorods are expected to be much more dispersed than those on the conventional particles. This lowers probability for diuron on the nanorods to be attacked by the hydroxyl radicals. On the other hand, considering the adsorption configuration, the aliphatic side of diuron adsorbs onto the mixed-terminated surface

of the nanorods, while the aromatic part is repelled away from the surface. Hence, the oxidation of diuron by a hydroxyl radical should occur at the aliphatic moiety. This is supported by the structures of diuron degradation intermediates that show sign of oxidation only on their aliphatic moiety (more detail in the next section). For the polar surfaces, however, the hydroxyl radical can attack the molecule of diuron on either the aliphatic or aromatic side because both sides adsorb onto the surfaces at the same time. Because the aromatic ring is much more stable than the aliphatic part of the molecule, as witnessed from the widely reported observation that ring-opening is the last step of the degradation pathway [52], the attack on the aromatic side is not as effective toward the degradation of diuron as that on the aliphatic side. The actual rate of diuron degradation on the surface of the conventional particles is therefore slower than on the nanorods.

#### 3.4.4.4 Photocatalytic degradation intermediates

The outlet stream from the reactor was collected and analyzed by LC-MS/MS to determine the structures of the diuron degradation products. Figures 3.43 and 3.44 report the major intermediates detected at different residence time when the ZnO nanorods and the conventional particles were used as the catalyst, respectively. The use of a microreactor, i.e., a continuous flow reactor, allows better identification of the sequence of intermediates formation than the experiment in a batch reactor. Within 15 minutes of residence time, the total of 8 reaction intermediates are formed on the ZnO nanorods, while 11 intermediates are generated from the diuron degradation on the conventional ZnO particles. The intermediates formed on these two catalysts are markedly different. Only 5 intermediates are common intermediates. Comparing with the intermediates reported in the previous work on the photocatalytic degradation of diuron on ZnO [53], 11 new intermediates were identified in this work. The pathways are inferred from the molecular structures of the intermediates. No intermediate was detected from the photolysis of diuron in the absence of a catalyst, because the extent of degradation was very low, i.e.,  $C_{out}/C_{in}$  was equal to only 0.98 even after a residence time of 15 min. In the presence of catalysts, intermediates were detected in the experiments with residence time of at least 1 min (but not with shorter residence time). It is therefore assumed that the intermediates detected at the residence time of 1 min were derived from photocatalytic diuron degradation. The concentrations of the detected intermediates could not be measured because of the lack of commercial standard reference compounds. However, all of the intermediates reported in Figure 3.43 and 3.44 were assumed to have concentrations on the

same order of magnitude because their corresponding chromatographic peak heights were similar. All paths shown are therefore major degradation pathways of diuron.

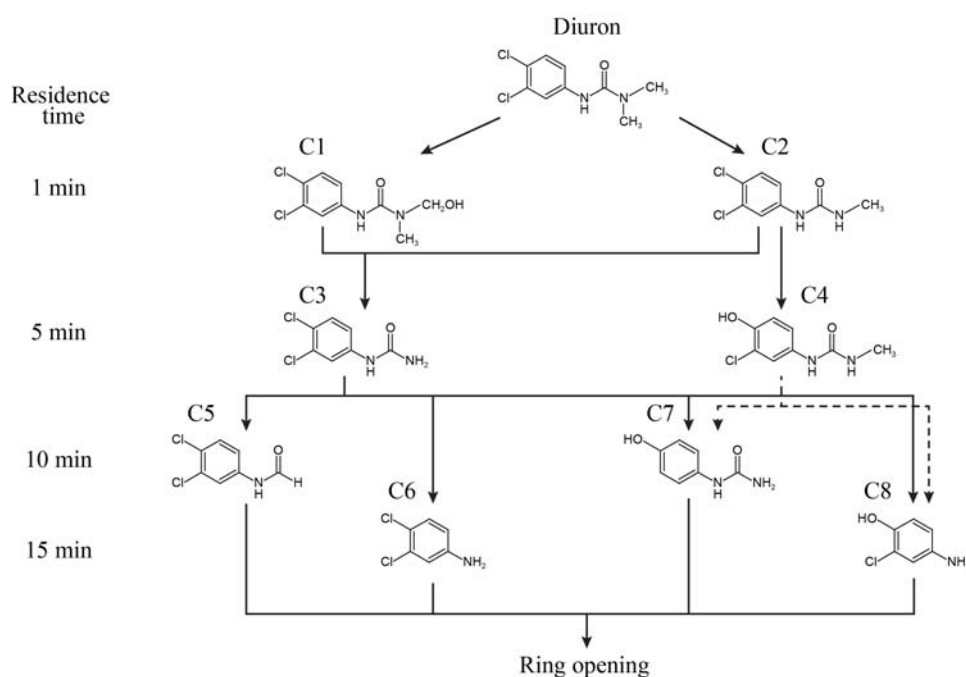


Figure 3.43 Structures of diuron degradation intermediates identified by LC-MS/MS and proposed degradation pathway of diuron catalyzed by ZnO nanorods.

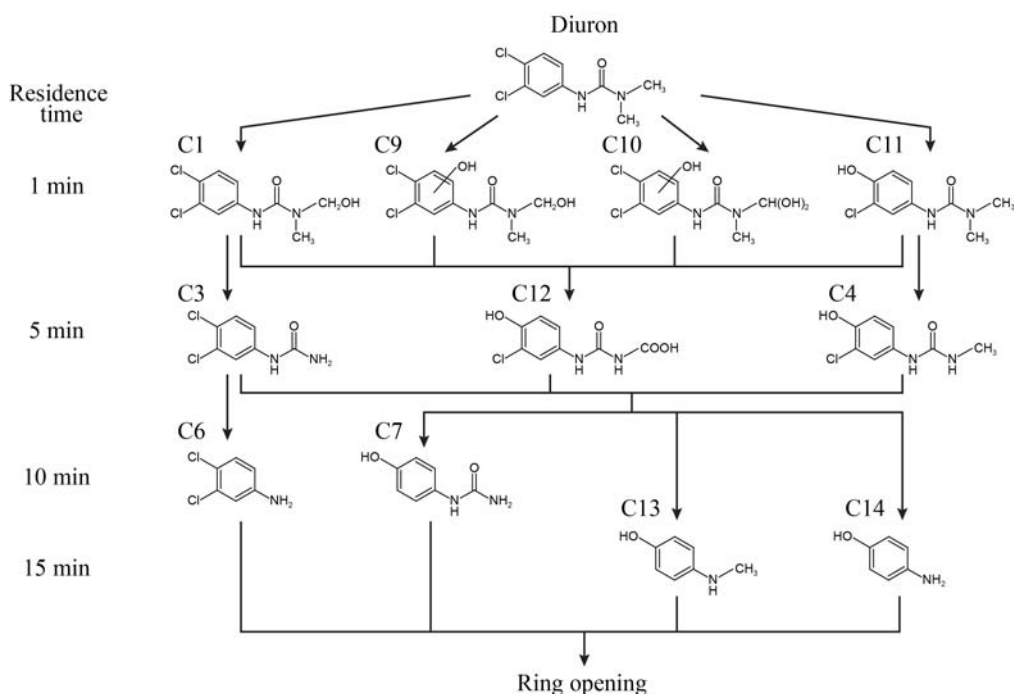


Figure 3.44 Structures of diuron degradation intermediates identified by LC-MS/MS and proposed degradation pathway of diuron catalyzed by conventional ZnO particles.

For the degradation on the ZnO nanorods, the first set of intermediates, i.e., C1 and C2, are formed by hydroxylation and demethylation at the methyl group, respectively. Interestingly, these reactions take place at the aliphatic moiety of diuron, which is the part of the molecule adsorbed on the mixed-terminated surface of the nanorods. Nevertheless, the methoxy oxygen, which is the closest part of the adsorbed diuron to the surface, is not attacked by the hydroxyl radical. An attack by hydroxyl radicals involves two steps, i.e., initiation and termination. In the initiation step, a hydroxyl radical transfers its radical character to a part of the adsorbate molecule. Then, the adsorbate radical combines with another hydroxyl radical in the termination step. It has been reported that the initiated adsorbate radical is more stable and more likely to proceed to the termination step when the attack of the hydroxyl radical takes place on either an atom with low electronegativity, such as carbon or hydrogen, or an atom attached to an atom with lone-pair electrons [54]. Therefore, for diuron, the attack on the methyl group would produce a more stable adsorbate radical than that on the methoxy oxygen; hence the formation of C1 and C2. It should be noted that there is no sign of an attack by the hydroxyl radical on the aromatic side of diuron within short residence time because the aromatic ring is lifted away from the surface by the repulsion between chlorine atoms on the ring and oxygen atoms on the surface. The lengthening distance of the ring from the surface lowers the probability of attack by the hydroxyl radical. However, as the residence time is prolonged, an attack on the aromatic side is eventually witnessed. The fact that DCA (i.e., C6) was detected only at long residence time discourages the suggestion from the previous report, which was conducted in a batch reactor, that DCA could be formed via direct hydrolysis of diuron or C2 [53].

Despite the similar conversion rates, the degradation pathway on the conventional ZnO particles is markedly different from that on the nanorods. We propose that the difference in pathways is caused by the adsorption configurations of diuron onto the surfaces. As previously discussed, diuron adsorbs in a planar configuration on the zinc-terminated surface, while it turns perpendicularly to the oxygen-terminated surface. Both of these give rise to equal probabilities of attack by the hydroxyl radicals on either the aliphatic or aromatic parts of diuron, hence the formation of both C1 and C11. Intermediates resulting from diuron being attacked on both sides of the molecule simultaneously, i.e., C9 and C10, were also observed during the degradation experiment even within short residence time. By the nature of physical adsorption, these intermediates can easily desorb from the surface. Nevertheless, as the residence time is prolonged, the intermediates re-adsorb and undergo further degradation until mineralization is achieved [55]. The structure of the subsequent intermediates should therefore depend on the adsorption characteristics of the products from the prior step in the pathway. It should also be



noted that, although the presence of the intermediates may not interfere with diuron adsorption within short residence time because of low concentration of the intermediates due to low conversion of diuron, the accumulated amount of the intermediates would compete with diuron adsorption and may exert interfering effect toward diuron adsorption configuration. Further detailed study is needed.

#### 4. Conclusions

Flexible nanofibers of  $\text{TiO}_2$  and  $\text{ZnO}$  could be fabricated by introducing PAN core. The process involves a formation of core-sheath structure via coaxial electrospinning, in which PAN solution is the core and a mixture of sol-gel derived  $\text{TiO}_2$  or  $\text{ZnO}$  and another polymer (e.g. PVP) is the sheath. After proper calcination to simultaneously convert the gel into either  $\text{TiO}_2$  or  $\text{ZnO}$  and remove the sheath polymer, the  $\text{PAN/TiO}_2$  or  $\text{PAN/ZnO}$  nanofibers could be formed. Many parameters, including viscosities of both solutions, polymer concentration, applied potential for electrospinning, and calcination temperature, limit the operating windows to product flexible  $\text{PAN/TiO}_2$  or  $\text{PAN/ZnO}$  nanofibers. However, after rigorous testing, although the presence of the photocatalyst crystals on the nanofibers was confirmed, the photocatalytic activity of the synthesized products is significantly inferior to the nanoparticles of the same photocatalyst.

In addition to the fabrication of the flexible nanofibers of photocatalyst, this work has discovered that the adsorption configuration of molecule being degraded on the surface of the catalyst greatly affects the characteristics of the reaction, including the adsorption capacity, rate of degradation on the surface, and the degradation pathway. The exposing surface of the catalyst is a crucial factor in determining the dominant degradation pathway.

#### 5. References

- [1] C.S. Lim, Synthesis and characterization of  $\text{TiO}_2$ - $\text{ZnO}$  nanocomposite by a two-step chemical method, *J Ceram Process Res.* 11 (2010) 631-635.
- [2] B. Dindar and S. Icli, Unusual photoreactivity of zinc oxide irradiated by concentrated sunlight, *J Photoch Photobio A.* 140 (2001) 263-268.
- [3] E. Leyva, C. Montalvo, E. Moctezuma, and S. Leyva, Photocatalytic degradation of pyridine in water solution using  $\text{ZnO}$  as an alternative catalyst to  $\text{TiO}_2$ , *J Ceram Process Res.* 9 (2008) 455-462.

- [4] N. Daneshvar, M.H. Rasoulifard, A.R. Khataee, and F. Hosseinzadeh, Removal of C.I. Acid Orange 7 from aqueous solution by UV irradiation in the presence of ZnO nanopowder, *Journal of Hazardous Materials*. 143 (2007) 95-101.
- [5] N. Daneshvar, D. Salari, and A.R. Khataee, Photocatalytic degradation of azo dye acid red 14 in water on ZnO as an alternative catalyst to TiO<sub>2</sub>, *Journal of Photochemistry and Photobiology A: Chemistry*. 162 (2004) 317-322.
- [6] D. Lawless, N. Serpone, and D. Meisei, Role of OH\* radicals and trapped holes in photocatalysis. A pulse radiolysis study, *J Phys Chem*. 95 (1991) 5166-5170.
- [7] L.E. Depero, Bonzi, P., Zocchi, M., Casale, C. and Gennaro, D.M., Study of the anatase-rutile transformation in TiO<sub>2</sub> powders obtained by laser-induced synthesis, *Journal of Materials Research* 8(1993 ) 2709-2715.
- [8] C.A.K. Gouvea, F. Wypych, S.G. Moraes, N. Durn, N. Nagata, and P. Peralta-Zamora, Semiconductor-assisted photocatalytic degradation of reactive dyes in aqueous solution, *Chemosphere*. 40 (2000) 433-440.
- [9] G. Marci, Augugliaro, V., Lopez-Munoz, M. J., Martin, C., Palmisano, L., Rives, V., Schiavello, M., Tilley, R. J. D. and Venezia, A. M., Preparation characterization and photocatalytic activity of polycrystalline ZnO/TiO<sub>2</sub> systems. 1. Surface and bulk characterization, *Journal of Physical Chemistry B*. 105 (2001) 1026-1032.
- [10] C. Su, B.Y. Hong, and C.M. Tseng, Sol-gel preparation and photocatalysis of titanium dioxide, *Catalysis Today*. 96 (2004) 119-126.
- [11] J. Tian, Wang, J., Dai, J., Wang, X. and Yin, Y., N-doped TiO<sub>2</sub>/ZnO composite powder and its photocatalytic performance for degradation of methyl orange, *Surface and Coatings Technology*. 204 (2009) 723-730.
- [12] W. Payakgul, O. Mekasuwandumrong, V. Pavarajarn, and P. Praserttham, Effects of reaction medium on the synthesis of TiO<sub>2</sub> nanocrystals by thermal decomposition of titanium (IV) n-butoxide, *Ceramics International*. 31 (2005) 391-397.
- [13] K. Sue, K. Kimura, M. Yamamoto, and K. Arai, Rapid hydrothermal synthesis of ZnO nanorods without organics, *Materials Letters*. 58 (2004) 3350-3352.
- [14] N. Daneshvar, Aber, S., Seyed Dorraji, M. S., Khataee, A. R. and Rasoulifard, M. H., Photocatalytic degradation of the insecticide diazinon in the presence of prepared nanocrystalline ZnO powders under irradiation of UV-C light, *Separation and Purification Technology*. 58 (2007) 91-98.

- [15] S. Janitabar-Darzi and A.R. Mahjoub, Investigation of phase transformations and photocatalytic properties of sol-gel prepared nanostructured ZnO/TiO<sub>2</sub> composites, *Journal of Alloys and Compounds*. 486 (2009) 805-808.
- [16] D.H. Reneker and A.L. Yarin, Electrospinning jets and polymer nanofibers, *Polymer*. 49 (2008) 2387-2425.
- [17] Y.M. Shin, M.M. Hohman, M.P. Brenner, and G.C. Rutledge, Experimental characterization of electrospinning: the electrically forced jet and instabilities, *Polymer*. 42 (2001) 9955-9967.
- [18] G. Srinivasan and D.H. Reneker, Structure and Morphology of Small-Diameter Electrospun Aramid Fibers, *Polym Int*. 36 (1995) 195-201.
- [19] D. Li and Y.N. Xia, Fabrication of titania nanofibers by electrospinning, *Nano Lett*. 3 (2003) 555-560.
- [20] X.H. Yang, C.L. Shao, H.Y. Guan, X.L. Li, and H. Gong, Preparation and characterization of ZnO nanofibers by using electrospun PVA/zinc acetate composite fiber as precursor, *Inorg Chem Commun*. 7 (2004) 176-178.
- [21] A. Greiner, J.H. Wendorff, A.L. Yarin, and E. Zussman, Biohybrid nanosystems with polymer nanofibers and nanotubes, *Appl Microbiol Biot*. 71 (2006) 387-393.
- [22] D. Li and Y.N. Xia, Direct fabrication of composite and ceramic hollow nanofibers by electrospinning, *Nano Lett*. 4 (2004) 933-938.
- [23] A.K. Moghe and B.S. Gupta, Co-axial electrospinning for nanofiber structures: Preparation and applications, *Polym Rev*. 48 (2008) 353-377.
- [24] X.L. Yu, H.F. Xiang, Y.H. Long, N. Zhao, X.L. Zhang, and J.A. Xu, Preparation of porous polyacrylonitrile fibers by electrospinning a ternary system of PAN/DMF/H<sub>2</sub>O, *Materials Letters*. 64 (2010) 2407-2409.
- [25] Z.C. Sun, E. Zussman, A.L. Yarin, J.H. Wendorff, and A. Greiner, Compound core-shell polymer nanofibers by co-electrospinning, *Adv Mater*. 15 (2003) 1929-+.
- [26] H. Kriel, R.D. Sanderson, and E. Smit, Coaxial Electrospinning of Miscible PLLA-Core and PDLLA-Shell Solutions and Indirect Visualisation of the Core-Shell Fibres Obtained, *Fibres Text East Eur*. 20 (2012) 28-33.
- [27] C.L. He, Z.M. Huang, X.J. Han, L. Liu, H.S. Zhang, and L.S. Chen, Coaxial electrospun poly(L-lactic acid) ultrafine fibers for sustained drug delivery, *J Macromol Sci B*. 45 (2006) 515-524.
- [28] N. Bhardwaj and S.C. Kundu, Electrospinning: A fascinating fiber fabrication technique, *Biotechnol Adv*. 28 (2010) 325-347.

- [29] H.F. Moafi, A.F. Shojaie, and M.A. Zanjanchi, Photoactive Polyacrylonitrile Fibers Coated by Nano-Sized Titanium Dioxide: Synthesis, Characterization, Thermal Investigation, *J Chil Chem Soc.* 56 (2011) 610-615.
- [30] A.V. Korobeinyk, R.L.D. Whitby, and S.V. Mikhlovsky, High temperature oxidative resistance of polyacrylonitrile-methylmethacrylate copolymer powder converting to a carbonized monolith, *Eur Polym J.* 48 (2012) 97-104.
- [31] P.K. Miao, D.M. Wu, K. Zeng, G.L. Xu, C.E. Zhao, and G. Yang, Influence of electron beam pre-irradiation on the thermal behaviors of polyacrylonitrile, *Polym Degrad Stabil.* 95 (2010) 1665-1671.
- [32] R.F. De Farias, C.C.G. Silva, and T.A.G. Restivo, Thermal study of the anatase-rutile structural transitions in sol-gel synthesized titanium dioxide powders, *J Serb Chem Soc.* 70 (2005) 675-679.
- [33] S. Yin, H. Hasegawa, and T. Sato, Phase-compositional and morphological control of titania nanoparticles via low temperature dissolution-reprecipitation process in liquid media, *Chem Lett.* (2002) 564-565.
- [34] J.H. Yu, S.V. Fridrikh, and G.C. Rutledge, Production of submicrometer diameter fibers by two-fluid electrospinning, *Adv Mater.* 16 (2004) 1562-+.
- [35] J.E. Diaz, A. Barrero, M. Marquez, and I.G. Loscertales, Controlled encapsulation of hydrophobic liquids in hydrophilic polymer nanofibers by co-electrospinning, *Adv Funct Mater.* 16 (2006) 2110-2116.
- [36] H.J. Lee, H. Suda, K. Haraya, and S.H. Moon, Gas permeation properties of carbon molecular sieving membranes derived from the polymer blend of polyphenylene oxide (PPO)/polyvinylpyrrolidone (PVP), *J Membrane Sci.* 296 (2007) 139-146.
- [37] M.F. Silva, C.A. da Silva, F.C. Fogo, E.A.G. Pineda, and A.A.W. Hechenleitner, Thermal and FTIR study of polyvinylpyrrolidone/lignin blends, *J Therm Anal Calorim.* 79 (2005) 367-370.
- [38] P. Bajaj, D.K. Paliwal, and A.K. Gupta, Acrylonitrile Acrylic Acids Copolymers .1. Synthesis and Characterization, *J Appl Polym Sci.* 49 (1993) 823-833.
- [39] W.X. Zhang, J. Liu, and G. Wu, Evolution of structure and properties of PAN precursors during their conversion to carbon fibers, *Carbon.* 41 (2003) 2805-2812.
- [40] M.X. Ji, C.G. Wang, Y.J. Bai, M.J. Yu, and Y.X. Wang, Structural evolution of polyacrylonitrile precursor fibers during preoxidation and carbonization, *Polym Bull.* 59 (2007) 527-536.

- [41] H. Kakida and K. Tashiro, Mechanism and kinetics of stabilization reaction of polyacrylonitrile and related copolymers .2. Relationships between isothermal DSC thermograms and FT-IR spectral changes of polyacrylonitrile in comparison with the case of acrylonitrile methacrylic acid copolymer, *Polym J.* 29 (1997) 353-357.
- [42] D. Zhu, A. Koganemaru, C.Y. Xu, Q.D. Shen, S.L. Li, and M. Matsuo, Oxidative stabilization of PAN/VGCF composite, *J Appl Polym Sci.* 87 (2003) 2063-2073.
- [43] E.C. Catalkaya and F. Kargi, Dehalogenation, degradation and mineralization of diuron by peroxone (peroxide/ozone) treatment, *J Environ Sci Heal A.* 44 (2009) 630-638.
- [44] B. Liu and H.C. Zeng, Hydrothermal synthesis of ZnO nanorods in the diameter regime of 50 nm, *J Am Chem Soc.* 125 (2003) 4430-4431.
- [45] B.H. Hameed, A.L. Ahmad, and K.N.A. Latiff, Adsorption of basic dye (methylene blue) onto activated carbon prepared from rattan sawdust, *Dyes and Pigments.* 75 (2007) 143-149.
- [46] T. Steiner, Unrolling the hydrogen bond properties of C-H center dot center dot center dot O interactions, *Chem Commun.* (1997) 727-734.
- [47] A. Kornherr, S.A. French, A.A. Sokol, C.R.A. Catlow, S. Hansal, W.E.G. Hansal, J.O. Besenhard, H. Kronberger, G.E. Nauer, and G. Zifferer, Interaction of adsorbed organosilanes with polar zinc oxide surfaces: a molecular dynamics study comparing two models for the metal oxide surface, *Chem Phys Lett.* 393 (2004) 107-111.
- [48] G. Pacchioni, Physisorbed and Chemisorbed CO<sub>2</sub> at Surface and Step Sites of the MgO(100) Surface, *Surf Sci.* 281 (1993) 207-219.
- [49] J. Li, J. Wang, G.K. Zhang, Y. Li, and K. Wang, Enhanced molecular molecular oxygen activation of Ni<sup>2+</sup>-doped BiO<sub>2-x</sub> nanosheets under UV, visible and near-infrared irradiation: Mechanism and DFT study, *Appl Catal B-Environ.* 234 (2018) 167-177.
- [50] J.F. Montoya, M.F. Atitar, D.W. Bahnemann, J. Peral, and P. Salvador, Comprehensive kinetic and mechanistic analysis of TiO<sub>2</sub> photocatalytic reactions according to the direct-indirect model: (II) Experimental validation, *J Phys Chem C.* 118 (2014) 14276-14290.
- [51] S. Malato, J. Caceres, A.R. Fernandez-Alba, L. Piedra, M.D. Hernando, A. Agüera, and J. Vial, Photocatalytic treatment of diuron by solar photocatalysis: Evaluation of main intermediates and toxicity, *Environ Sci Technol.* 37 (2003) 2516-2524.
- [52] M.J. Farre, S. Brosillon, X. Domenech, and J. Peral, Evaluation of the intermediates generated during the degradation of Diuron and Linuron herbicides by the photo-Fenton reaction, *J Photoch Photobio A.* 189 (2007) 364-373.

- [53] J. Fenoll, M. Martinez-Menchon, G. Navarro, N. Vela, and S. Navarro, Photocatalytic degradation of substituted phenylurea herbicides in aqueous semiconductor suspensions exposed to solar energy, *Chemosphere*. 91 (2013) 571-578.
- [54] F. Gozzo, Radical and non-radical chemistry of the Fenton-like systems in the presence of organic substrates, *J Mol Catal a-Chem*. 171 (2001) 1-22.
- [55] J. Li, X.Y. Wu, Z. Wan, H. Chen, and G.K. Zhang, Full spectrum light driven photocatalytic in-situ epitaxy of one-unit-cell  $\text{Bi}_2\text{O}_2\text{CO}_3$  layers on  $\text{Bi}_2\text{O}_3$  nanocrystals for highly efficient photocatalysis and mechanism unveiling, *Appl Catal B-Environ*. 243 (2019) 667-677.

## Output ที่ได้จากโครงการ

Sutaporn Meephon, Thanyada Rungrotmongkol, Somchintana Puttamat, Supareak Praserttham and Varong Pavarajarn, “Heterogeneous photocatalytic degradation of diuron on zinc oxide: Influence of surface-dependent adsorption on kinetics, degradation pathway, and toxicity of intermediates”, Journal of Environmental Sciences (in press), มี impact factor 3.120 <https://doi.org/10.1016/j.jes.2019.04.016>.